Theses and Dissertations

2015

Computational Study of Soft-Sphere and DNA-Mediated Interparticle Interactions

Yajun Ding
Lehigh University

Follow this and additional works at: http://preserve.lehigh.edu/etd

Part of the Chemical Engineering Commons

Computational Study of Soft-Sphere and DNA-Mediated Interparticle Interactions

by

Yajun Ding

Presented to the Graduate and Research Committee

of Lehigh University

in Candidacy for the Degree of

Doctor of Philosophy

in

Chemical Engineering

Lehigh University

August 2015

Approved and recommended for acceptance as a dissertation in partial fulfillment of the requirements for the degree of Doctor of Philosophy.

Committee:

Jeetain Mittal, Committee Chair

James F. Gilchrist

Mark Snyder

Anthony McHugh

James D. Gunton

Acknowledgements

Contents

List of Tables

List of Figures

Abstract

Colloidal particles exhibit versatile dynamic behaviors and structures, dependent on various interactions between these particles. In this dissertation, we studied two representative colloidal systems: one with classic repulsive interparticle interactions and the other with novel DNA-mediated interparticle interactions.

In the first part of this dissertation, we studied the equilibrium and nonequilibrium dynamics and structure of soft particles, which are modeled by the inverse power potential. The freezing-point scaling relation, to a good approximation, collapses diffusivity and viscosity data of different particle softness. Using the freezing-point scaling relation as a starting point, shear rheology and microstructures of particles with different softness are studied. A universal shear-thinning behavior was observed for particles with different softness in absence of hydrodynamics, albeit softer particles exhibit stronger shear-thinning tendency. By investigating the microstructure of these systems, a strong relation between the changes of the structures and the particle softness was found in presence of shear. These different microstructure changes in responses to the shearing might explain the extent of shear-thinning behavior for different particle softness.

In the second part of this dissertation, we studied the self-assembly of DNA-functionalized particles (DFPs). The coarse-grained model was developed for DFPs. The potential of mean forces (PMFs) between two DFPs were computed as a function of temperatures, DNA grafting density and lengths of the hybridizing and non-

hybridizing parts of DNA. The computed PMFs were used to study the self-assembly of ordered 2D binary crystal lattices. Three crystal phases were identified: square lattice, alternating-string (A-S) hexagonal lattice, honeycomb lattice, by controlling the binding energies between different particle species. The square lattices always exhibit perfect compositional ordering while significant defects appear in hexagonal lattices due to the interplay between thermodynamic and kinetic factors.

Chapter 1

Introduction

Colloids are particles with sizes ranged approximately from one nanometer to ten micrometers suspended in a medium. These particles experience Brownian motion because of their interaction with solvent molecules [122]. Colloids can also form crystals that can exhibit precise particle arrangements and periodic structures spanning hundreds of particle diameters in two or three dimensions [36]. All of these properties of colloids make them very useful for various applications including photonic materials and sensors [55, 133]. The equilibrium state in which a colloidal system exists, either gas, liquid or solid, is highly dependent on the various interactions between colloidal particles [20]. The knowledge of particle interactions is not only helpful for the understanding the relations between these interactions and properties of equilibrium states, but also can be used to tune these interactions to favor the assembly of one structure over another [83].

It is very difficult to determine the relation between initial system conditions and final assembled structures from both theoretical and experimental point of view. Simulation offers an effective method to map various system variables to final states. Modeling of colloidal particle system at the microscopic level is based on comprehensive description of the constituent components. In principle, the rigorous description

relies on the theory of quantum mechanics. By representing atoms or molecules as point masses interaction through some forces, molecular dynamics not only does it work, but works surprisingly well [111]. The aim of this work is to apply computational method to study the relation between particle interaction and accessible states for a given colloidal suspension.

1.1 Colloidal interactions

1.1.1 Classic colloidal interactions

In terms of forces between the colloidal particles, the first contribution stems from the van der Waals attraction [48]. This attraction diverges at particle contact and vanishes as r^{-6} for interparticle distances r. In absence of other interparticle interactions, the particles will aggregate and form large clusters. Hence, the stability of a colloidal suspension requires the existence of additional stabilizing forces. There are two common stabilizating forces for colloidal systems, steric force and electrostatic force. For steric force, the colloidal particles are coated with polymers on their surfaces, which prevent two neighboring particles to come in close contact. This steric force generally can be described as the pairwise hard sphere potential or repulsive potential dependent on the particle hardness [18, 121]. In regards to electrostatic force, the charged surface groups of colloidal particles dissociate into the polar solvent and form counterions, which make the colloidal particles become highly charged macroions. These counterions form an atmosphere of ions in rapid thermal motion close to the surface, known as the diffuse electric double layer. Two particles with similarly charged surfaces usually repel each other electrostatically in solution. The van der Waals attraction always excesses the electrostatic repulsion at small distance due to its power-law interaction. The combination action of electrostatic and van der Waals forces can be described quantitatively by the celebrated DLVO theory of

colloidal stability [124].

1.1.2   DNA-mediated interactions

Specific functionalization of colloidal particles can be used to tailor interparticle interactions [113]. Due to their abilities of forming highly complex and precise structures, biomolecules such as DNA are good candidate to glue particles together. The specificity and tunability of DNA-mediated interactions arise from the assignment of the DNA base pair sequence. The DNA sequence is comprised of four different bases: adenine (A), cytosine (C), guanine (G), and thymine (T). Complementary binding of base pairs A:T and G:C makes two single DNA strands forms double helices. Many researchers have studied the sequence-specific binding and programmability of DNA-mediated interactions [19, 102, 108, 146]. These DNA-mediated interactions can drive the crystallization of nano-sized and micro-sized particles with abundant crystal morphology [85].

1.2   Self assembly

Self-assembly is one powerful method that can be used to create long-range ordered crystals from systems with disordered initial states. The crystallization is driven by the interactions between system components without the need for external mechanical forces. In addition, predefined equilibrium structures can also be created through self-assembly. The simplest case is the hard sphere system, which has no interactions between particles. The fluid-solid phase transition as increasing the packing density is driven only by entropy [152]. The complexity of phase diagram increases when introducing attractive and repulsive forces, while the inclusion of different particle shapes and sizes further increases the its complexity [98]. Colloidal suspensions with van der Waals and electrostatic interactions self assemble into limited nanocrystals,

such as fcc, bcc and hcp [71]. The morphological diversity of assembled crystals from these suspensions is greatly improved with the introduction DNA-mediated interactions [85].

1.3 Dissertation Outline

In this dissertation, two distinct systems are studied: first, the soft particle fluids which are modeled by inverse power potential and second, DNA-functionalized colloidal particles. This dissertation is arranged as follows:

Chapter 2: Equilibrium structure and dynamics of soft particles

In this chapter we test freezing-point scaling relation. This freezing-point scaling relation, to a good approximation, collapses diffusivity and viscosity data of different particle softness. Although the freezing-point scaling relation cannot perfectly collapse the transport coefficient, it is a convenient and effective parameter for comparing the structure and dynamics of the system with different softness, especially from the experimental point of view.

Chapter 3: Structure and dynamics of sheared soft particles

Using the freezing-point scaling relation as a starting point, shear rheology and microstructures of particles with different softness are studied using nonequilibrium molecular dynamics simulations. Our results show that a universal shear-thinning behavior for particles with different softness in absence of hydrodynamics, albeit softer particles exhibit stronger shear-thinning tendency. By investigating the microstructure of these systems, we found a strong relation between the changes of the structures and the particle softness in presence of shear. These different microstructure changes in responses to the shearing might explain the extent of shear-thinning behavior for different particle softness.

Chapter 4: Coarse-grained DNA model

DNA has emerged as an exceptional molecular building block for nanoconstruction due to its predictable conformation and programmable intra- and inter-molecular Watson-Crick base-pairing interactions. The emergence of DNA nanotechnology at the same time also inspires the development of the design rules and reliable assembly methods to engineer DNA nanostructures of increasing complexity, which requires the understanding these systems at the molecular level. Simulation provides a very powerful tool due to its convenience, high efficiency as well as the level of details. In this chapter, two coarse-grained DNA model is presented for the application of modeling self-assembly processes. These two models are relatively simple yet accurately portrays the dynamics and denaturing of DNA and allow for the analysis of larger systems of interest for a long time without sacrificing computational efficiency.

Chapter 5: DNA-mediated interparticle interactions

DNA-functionalized particles have great potential for the design of complex self-assembled materials. The major hurdle in realizing crystal structures from DNA-functionalized particles are expected to be kinetic barriers that trap the system in metastable amorphous states. Therefore, it is vital to explore the molecular details of particle assembly processes in order to understand the underlying mechanisms. Molecular simulations based on coarse-grained models can provide a convenient route to explore these details. Most of the currently available coarse-grained models of DNA-functionalized particles ignore key chemical and structural details of DNA behavior. These models therefore are limited in scope for studying experimental phenomena. In this chapter, we present a new coarse-grained model of DNA-functionalized particles, which incorporates some of the desired features of DNA behavior. The coarse-grained DNA model used here provides explicit DNA representation (at the nucleotide level) and complementary interactions between Watson-Crick base pairs, which lead to the formation of single-stranded hairpin and double-stranded DNA. Aggregation between multiple complementary strands is also

7

prevented in our model. We study interactions between two DNA-functionalized particles as a function of DNA grafting density, lengths of the hybridizing and non-hybridizing parts of DNA, and temperature. The calculated free energies as a function of pair distance between particles qualitatively resemble experimental measurements of DNA-mediated pair interactions.

Chapter 6: Self-assembly of DNA-functionalized particles

In this chapter, we report a comprehensive computational analysis of the self assembly of ordered 2D binary crystal lattices, in which the interactions are governed by DNA bridging between particles. Three crystal phases were identified: square lattice, alternating-string (A-S) hexagonal lattice, honeycomb lattice, by controlling the binding energies between different particle species. The attractive interactions between like particles i.e. E_{AA} and E_{BB}, are required to stabilize the hexagonal lattices over square lattices. At the same time, a large difference in the binding energies, i.e. between E_{AB} and E_{BB} or E_{AA}, is required to reduce the equilibrium concentration of defects. As a result, highly constrained conditions were required in order to achieve good ordering in the hexagonal lattices. On the other hand, without the complication of E_{AA} and E_{BB}, it is much easier to grow perfect square lattices.

Chapter 7: Future work and preliminary results

In this chapter, we propose possible extensions with preliminary results to the current computational work.

Chapter 2

Equilibrium structure and dynamics of soft particles

2.1 Introduction

Concentrated suspensions of soft particles, such as microgel suspensions, polymer coated colloids and compressed oil in water emulsions, have attracted a lot of interest both from academic and industrial aspects. These soft particles are deformable and impenetrable and can be packed beyond the random close packing fraction for hard spheres [21]. Purely repulsive systems have been widely used to model soft particles to understand fundamental questions related to the their behavior in a suspension [18, 121]. Among the various soft repulsive potentials, the inverse power (IP) potential, $U(r) = \epsilon(\sigma/r)^n$, has been studied extensively due to its simple form and ability to capture interesting physical phenomenon [17, 40, 41, 42, 43]. The IP potential model has simply two phases: fluid phase and crystal phase, with a well-known universal phase diagram [2, 53, 110]. The states of IP potential fluid is governed by a single dimensionless parameter that coupling the temperature and density, $\Gamma = \rho\sigma^3(\epsilon/k_B T)^{3/n}$, where ρ is the number density, σ is particle diameter, k_B

is Boltzmanns constant, T is the absolute temperature and n mediates the softness of the particle.

The exploration of the relations between particle softness and the static and dynamic properties of fluids has been the major topic for soft particles [4, 8]. Since the transport coefficient (e.g. diffusion coefficient or viscosity) is problematic to measure experimentally, it is desired to establish possible relationships between these coefficients and some quantities which are usually more readily measured. The recent simulations of IP potentials attempted to establish the scaling relations between the transport coefficients and the particle softness. For large values of n ($n \geq 72$), the behavior of IP potential approaches the hard sphere limit [39]. A scaling law derived from the perturbation theory has also claimed to collapse transport coefficients for extremely soft systems ($n \leq 12$), while ineffective for higher n due to ignoring the higher order terms in the expansion of interaction energy [118]. More recently, for intermediate n ($18 \leq n \leq 36$) a scaling relation based on freezing point are able to collapse the transport coefficients [67]. In addition to explore the scaling relations specifically for IP potentials, Rosenfeld proposed a simple universal relationship between reduced transport coefficient and the excess entropy s^{ex} [114]. This relationship is supported by many studies on various model [30, 115] and real fluids [117, 150].This treatment has also been extended to binary fluid mixtures [30, 44, 93, 117], anomalies in waterlike model fluids [31, 32, 62, 129] and particles under molecular-dimensional confinement [91, 92]. However in the very diluted and dense fluid region, a simple exponential dependence between transport coefficients and s^{ex} fails. Therefore, despite various proposed scaling relations, none of the existing empirical scaling relations in the literature correctly describes transport coefficients over the entire fluid range.

In this chapter, we test the freezing-point scaling relation for soft particles for extended parametric space through molecular dynamics simulations. We report that by using reduced formulations, diffusion coefficient and viscosity of inverse power

potentials collapse when plotted against reduced coupling parameter for a broader set of potential softness and wider range of coupling parameters. The width of the collapsed master curve indicates that although this scaling law accurately captures the long-range structure, structural differences at short distances may limit this correlation. We also report data of universal scaling between the reduced transport coefficient and two-body excess entropy for inverse power potentials. We show a strong correlation between two-body excess entropy and reduced coupling parameter, which is denoted by the collapsing for different softness when two-body excess entropy is plotted against reduced coupling parameter.

2.2   Methods

The soft sphere potential has the form:

$$U(r) = \epsilon \left(\frac{\sigma}{r}\right)^n, \tag{2.1}$$

where r is the distance between two particles, σ is particle diameter, ϵ sets energy scale and n determines the potential steepness with $1/n$ representing the softness of potential. Throughout the paper we use the Lenard-Jones reduced system of units, where σ is the unit of distance, ϵ is the unit of energy, and mass is measured in units of particle mass. The potential is cut at the distance $r_c = 2.5$, at which all the potential are very close to zero. The system of 500 particles is simulated in a canonical ensemble (constant N, V and T) using the Nose-Hoover thermostat. Equations of motion are integrated by the velocity Verlet algorithm using a time step of 0.001 in LJ unit. The initial configuration is started from the fcc lattice at temperature $T = 4.0$. The system is first melted at $T = 4.0$ and then quenched to the temperature $T = 1.0$ and the equilibrated. The diffusion coefficient is calculated

from the mean square displacement via the Einstein relation, while the zero-shear viscosity is determined by using the Green-Kubo relation.

2.3 Results and discussion

Following the work by Lange [67], a scaling law based on the coupling parameter at the freezing point, Γ_f, is used to scale the diffusion coefficient and viscosity. Since at the freezing point the structural and dynamical quantities are independent of particle interactions, by scaling Γ with Γ_f, the long-range structure is almost identical for systems with different softness. This reduced coupling parameter Γ/Γ_f basically measures how far the system away from the freezing transition, which can be treated as the key parameter for comparing the structure to that of a system with different softness. In this study, we first test this scaling law for an extended parametric space. Specifically, we investigate $n = 4$, 6, 8, 10, 12, 24, 36 and $0.01 \leq \Gamma/\Gamma_f \leq 1$.

Before showing the data, it is worthy to note that the relevant length scale of each system with different n is the average particle separation $\Gamma^{-1/3}$. This can be clearly demonstrated by checking the pair distribution function $g(r)$ for different n at freezing point [67], which is maximally collapsed when r is scaled by $\Gamma^{-1/3}$. Therefore, reduced transport coefficients according to Rosenfeld [114], $D^* = D\rho^{1/3}(k_B T/m)^{-1/2}$ and $\eta^* = \eta\rho^{-2/3}(mk_B T)^{-1/2}$ are used, instead of original D and η, to account for this average interparticle distance for different potential softness.

The reduced diffusion coefficient D^* for the different particle softness is presented in Figure 2.1 as a function of reduced coupling parameter Γ/Γ_f with the original data D plotted with Γ presented in the inset of Figure 2.1. It can bee seen from the inset of Figure 2.1 the value of the diffusion coefficient at the freezing transition is almost identical for each case of n, which is around 0.01. By plotting the reduced diffusion coefficient against Γ/Γ_f, to a good approximation, a collapse of the data of different
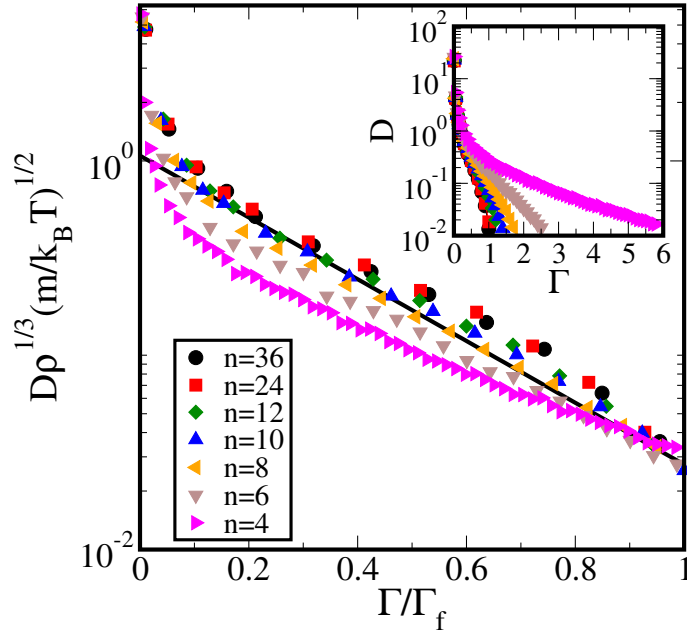
Figure 2.1: Reduced diffusion coefficient, $D\rho^{1/3}(k_B T/m)^{-1/2}$, versus reduced coupling parameter Γ/Γ_f for different softness n described in the legend. The inset shows the original diffusion coefficient D plotted against coupling parameter Γ.

softness is observed. Similarly, we show the viscosity data in Figure 2.2. As might be expected from diffusion data, a convincing collapse of the viscosity data is found. Although the scaling law leads to a better collapse of both diffusion and viscosity data, one can notice that width of master curve is still large. Due to the noise of the viscosity data, the collapsed single curve is much thicker than diffusion data. As predicted previously [115], there is a minimum in viscosity plot, which separates into weak coupling and strong coupling region. As the density increases and approaches freezing, the both curves are collapsing as one might expect. Therefore it is clear that although the scaling law captures the identical long range structure for systems with equal Γ/Γ_f, structure differences at short distances due to the different interaction potentials might be responsible for the quality of collapsing.

Another interesting statistical quantity that can also be measured in a simulation is the two-body excess entropy s_2 [97]. This quantity is essentially the N-body interparticle correlation function expansion of the excess entropy truncated at the
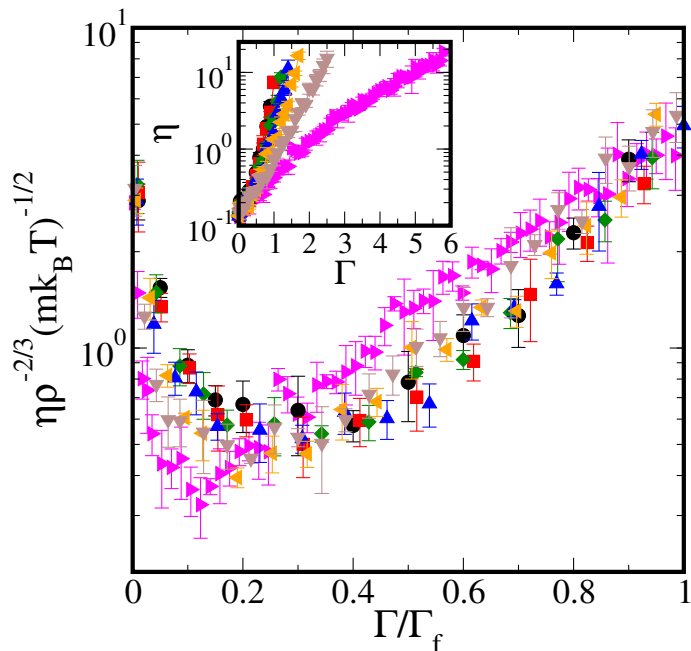
Figure 2.2: Reduced viscosity, $\eta\rho^{-2/3}(mk_BT)^{-1/2}$, versus reduced coupling parameter Γ/Γ_f for different softness n described in the legend of Figure 2.1. The inset shows the original viscosity η plotted against coupling parameter Γ.

two-body level. Although excess entropy can be rigorously calculated in simulations [7, 92, 93], it has been shown in earlier studies that two-body excess entropy is a reasonable approximation for the full excess entropy in many model liquids [30, 115]. This two-body excess entropy is also a measure of the order of the system [140]. s_2 is zero for completely disordered systems like ideal gas, becomes large and negative for ordered structures and goes to negative infinity for perfect crystal. Rosenfeld [114] observed that reduced transport coefficients approximately exponentially depend on the excess entropy of the liquid. In fact, this relation is approximately true for many "strongly correlating" simple liquids [125]. The quantitative link between reduced transport coefficient and $-s_2$ is tested here for soft sphere fluids. Figure 2.3 shows reduced diffusion coefficient D^* (top) and viscosity η^* (bottom) as a functions of $-s_2$ for different softness, respectively. Both D^* and η^* appears to collapse onto single curves when plotted versus $-s_2$, with a much better quality of collapse than Γ/Γ_f

14

scaling.
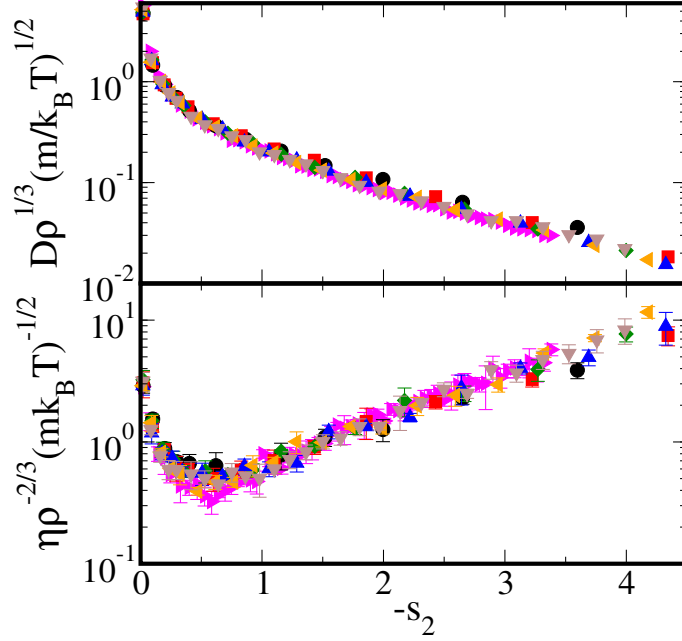
Figure 2.3: (top) Reduced diffusion coefficient, $D\rho^{1/3}(k_BT/m)^{-1/2}$, and (bottom) reduced viscosity $\eta\rho^{-2/3}(mk_BT)^{-1/2}$, versus negative two-body excess entropy, $-s_2$, for different softness n described in the legend of Figure 2.1.

Since both Γ/Γ_f and s_2 are indications of structural order in the system, it is naturally to ask whether there is any relations between these two quantities. Figure 2.4 shows $-s_2$ plotted versus Γ/Γ_f for different particle softness. A well collapse of our curves implies that there is strong correlation between Γ/Γ_f and s_2. This strong correlation is physically intuitive since two-body excess entropy is essentially a measure of the difference from the ideal gas in terms of available states, while Γ/Γ_f is a natural parameter measuring the distance from the freezing transition. Both reference points are independent of specific particle interaction. The discrepancy between those curves can be explained by the way of particle with difference softness approach two reference states.

It was found that the excess entropy s^{ex} for inverse-power potentials follows a quasi-universal scaling law of the form $s^{ex} \simeq f(\kappa/\kappa_f)$, where κ is related to our coupling parameter Γ by the form of $\kappa = ((4\pi/3)\Gamma)^{n/3}$ [116]. By combining this scaling
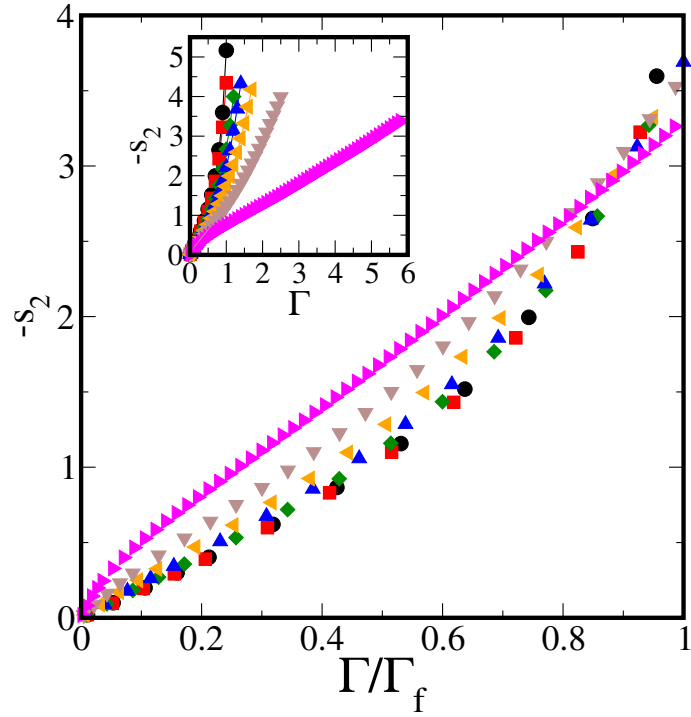
Figure 2.4: Two-body structural order parameter $-s_2$ as a function of reduced coupling parameter Γ/Γ_f for different softness n described in the legend of Figure 2.1. The inset shows the two-body structural order parameter $-s_2$ plotted against coupling parameter Γ.

law with semiempirical universal relation between reduced transport coefficient and excess entropy, Rosenfeld [116] found that reduced transport coefficient is scaled approximately as a function of κ/κ_f for $n \leq 12$. Since this relation is a combination of two approximate scaling relations, the error of the combined relation might be a propagation of two.

2.4 Conclusions

In this chapter we test freezing-point scaling relation. This freezing-point scaling relation, to a good approximation, collapses diffusivity and viscosity data of different particle softness. Although the freezing-point scaling relation cannot perfectly collapse the transport coefficient, it is a convenient and effective parameter for comparing the structure and dynamics of the system with different softness, especially from the experimental point of view. The calculation of the two-body excess entropy is still quite difficult from experiments especially for 3D systems. The validity of this universal scaling law in experiments has not been well tested for colloidal particle suspensions. Recently, Ma et al. [84] tested of this excess-entropy scaling law of diffusion by using colloidal monolayers. By considering above points, in the next chapter we will apply the freezing-point scaling relation as a reasonable starting point to study the shear rheology and microstructure of particles with different softness.

Chapter 3

Structure and dynamics of sheared soft particles

3.1 Introduction

Colloidal suspensions exhibit many nonlinear responses to the applied flow rate, i.e.
shear thinning, thickening or a mixture of the both nonlinear responses. Understand-
ing the shear rheology of dense colloidal suspensions still remains a challenge. Many
experimental studies and computer simulations have attempted to relate changes in
particle configurations to the nonlinearity of these phenomena [22, 23, 35, 51, 78,
79, 147], albeit no conclusive statement has been made. Recently simultaneous ap-
pearance of the layering structural change and the shear thinning was observed by
Cheng et al. [22]. However the results of Xu et al. [148] indicated the simultaneous
appearance of layering and shear thinning is coincidental rather than causal. They
demonstrated that pair structure in the suspension has a stronger correlation with
shear-thinning phenomenon. Layer formation can be enhanced by the presence of
planar boundaries, i.e. walls in experiments or simulations [148]. Several groups
observed hydroclusters in the shear thickening regime [22, 51], which is consistent

with the prediction by Brady and coworkers [13, 15, 34, 109] that shear thickening is caused by the formation of transient hydroclusters induced by shearing.

Shear rheology of hard sphere systems, such as silica, poly(methyl methacrylate) or PMMA and polystyrene (PS), have been extensively studied due to its simplicity and abundances of relevant theoretical work [95, 134]. Soft sphere systems, spanned from ultrasoft polymeric coils and star polymers to quasi-hard sphere such as core-shell microgels and emulsions, show very richer rheological properties than the hard counterparts [21, 143, 145]. The understanding the relation between structure and macroscopic rheological properties of soft sphere systems and prediction their behavior is much more challenging. The versatile rheological properties of soft particle systems are closely linked to the softness of interparticle interactions, which imply the tunability of rheological behaviors by varying the particle softness. Nazock-dast and Morris [99] investigated the effect of steepness of repulsive interactions on the structure and rheology of sheared colloidal systems from both simulations and theory. In this study, soft colloids, modeled by Yukawa interactions, exhibited the shear-thinning behavior and no shear thickening was observed. They proposed the lubrication forces are significantly reduced in soft colloidal system and the interparticle repulsive forces balance the shearing forces to determine the pair microstructure. Recently, Zhou et al. [151] examined the effect of microgel softness on its shear thickening behavior using core-shell microgel particles. The measured interaction potentials between microgel particles were successfully mapped to the inverse power potential. They observed as effective volume fraction increased, temperature increased or shell thickness decreased, the shear thickening behavior became more obvious. The reason of shear thickening for their system is still under investigation. Xu et al. [147] also examined the effect of "softness" of particles on the structure of colloidal suspension by tuning electrostatic interactions. The tuning of electrostatic interactions changes the effective particle diameter preventing the direct contact between particles. They

found electrostatic interactions played a complex role in suspension structure.

In this chapter we investigate the effect of particle softness on microstructure and rheology of sheared soft particle system. Soft particles are modeled by the inverse power (IP) potential, which has been successfully mapped to the interactions of poly(12-hydroxystearic acid) or PHSA particles [18] and several types of core-shell microgel particles [60, 121, 127, 151]. Nonequilibrium molecular dynamics (NEMD) are used for shearing simulation. By decoupling the hydrodynamic interactions, we would expect only shear-thinning behavior are captured in our simulation. Our results show that a universal shear-thinning behavior for particles with different softness, albeit softer particles exhibit stronger shear-thinning tendency. By investigating the microstructure of these systems, we found a strong relation between the changes of the structures and the particle softness in presence of shear. Specifically, the shearing slightly enhanced the overall translational ordering of quasi-hard sphere by strengthening the correlation of nearest-neighbor particles and slightly weakening the long-range ordering, while significantly decreased the ordering of softer particles. The shearing has a much pronounced effect on enhancing the correlation along flow direction for quasi-hard sphere, while at the same time induce a pronounced secondary depletion region for ultrasoft particles. These different responses to the shearing might explain the extent of shear-thinning behavior for different particle softness.

3.2 Methods

The soft sphere potential has the form:

$$U(r) = \epsilon \left(\frac{\sigma}{r} \right)^n, \tag{3.1}$$

where r is the distance between two particles, σ is particle diameter, ϵ sets energy scale and n determines the potential steepness with $1/n$ representing the softness of potential. Throughout the paper we use the Lenard-Jones reduced system of units, where σ is the unit of distance, ϵ is the unit of energy, and mass is measured in units of particle mass. The potential is cut at the distance $r_c = 2.5$, at which all the potential are very close to zero. The system of 500 particles is simulated in a canonical ensemble (constant N, V and T) using the Nose-Hoover thermostat. Equations of motion are integrated by the velocity Verlet algorithm using a time step of 0.001 in LJ unit. The initial configuration is started from the fcc lattice at temperature $T = 4.0$. The system is first melted at $T = 4.0$ and then quenched to the temperature $T = 1.0$ and the equilibrated. The diffusion coefficient is calculated from the mean square displacement via the Einstein relation, while the zero-shear viscosity is determined by using the Green-Kubo relation. For nonequilibrium molecular simulation (NEMD), the thermostatted SLLOD equations of motion with the appropriate periodic boundary conditions are used to study the system under shear. The x-direction is set as the flow direction, while the y-direction is velocity gradient. Shear rate is defined as $\dot{\gamma} = dv_x/dy$. Shear viscosity is calculated by $\eta = -\langle\sigma_{xy}\rangle/\dot{\gamma}$. The two-body structural order parameter $-s_2$ was computed using the expression [140]

$$-s_2 = \frac{\rho}{2} \int \{g(\mathbf{r})\ln g(\mathbf{r}) - [g(\mathbf{r}) - 1]\}d\mathbf{r}, \tag{3.2}$$

where ρ is number density and $g(\mathbf{r})$ is the pair distribution function. The cumulative order integral I_{s_2} was defined as [61]

$$I_{s_2} = \frac{\rho}{2} \int_0^r dr' \int_0^{2\pi} d\theta \int_0^\pi d\phi r'^2 sin(\phi)f(r), \tag{3.3}$$

where $f(r) = g(r',\theta,\phi)\ln g(r',\theta,\phi) - [g(r',\theta,\phi) - 1]$.

3.3 Results and discussion

3.3.1 Rheological properties

As showed in equilibrium simulation, by maintaining the equal Γ/Γ_f, the systems with different particle softness have similar long-range structure and dynamics. We select the state close to freezing transition, $\Gamma/\Gamma_f = 0.85$, for the shear simulations. The shear rate dependence of $\eta(\dot{\gamma})$ as well as zero-shear viscosity by Green-Kubo relation for different particle softness is given in Figure 3.1. The extrapolation of the finite shear rate values to zero shear-rates is consistent with the Green-Kubo values. The rheological behavior becomes Newtonian at low shear rate where η approach its zero-shear viscosity η_0. At high shear rate, the fluids display a shear-thinning behavior. We note that the shear-thinning behavior is dependent on the softness of particle interactions even by maintaining the same Γ/Γ_f. The softer particles exhibit stronger shear-thinning phenomenon.
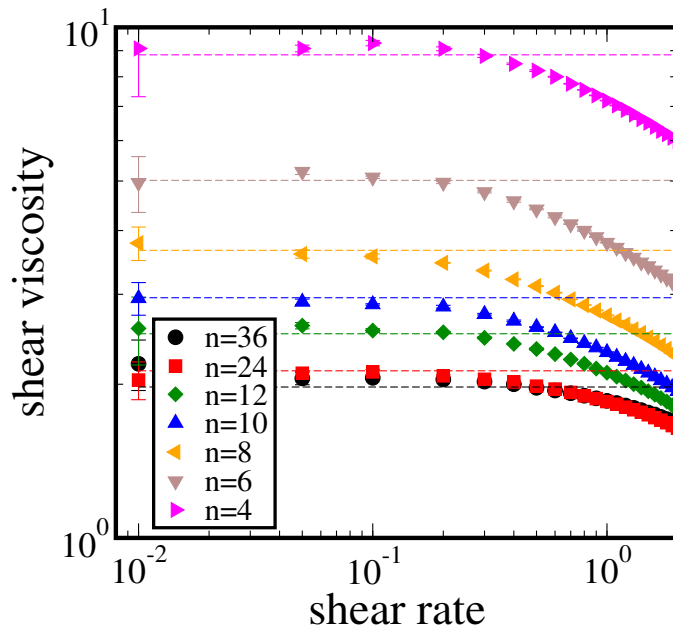
Figure 3.1: Shear viscosity η versus shear rate $\dot{\gamma}$ for the different particle softness n described in the legend at $\Gamma/\Gamma_f = 0.85$. Dashed lines represent zero-shear viscosity η_0.

We have also calculated first and second normal stress difference as a function of shear rate. First and second normal stress difference are defined as $N_1 = \Sigma_{xx} - \Sigma_{yy}$ and $N_2 = \Sigma_{yy} - \Sigma_{zz}$, which are both zero at equilibrium and become nonzero under shear. As can be see in Figure 3.2, the sign of N_2 is negative for both $n = 36$ and 4 under the shear, while N_1 is positive for $n = 4$ and slightly negative for $n = 36$. The positive sign of N_1 and the negative sign of N_2 for ultrasoft particles confirms previous results of charged colloids [112]. The negative sign of N_1 and N_2 of quasi-hard sphere particles resemble the hard sphere behavior [34]. In addition, we observed that the increase of particle softness leads to a more positive first normal stress difference (data are not shown).
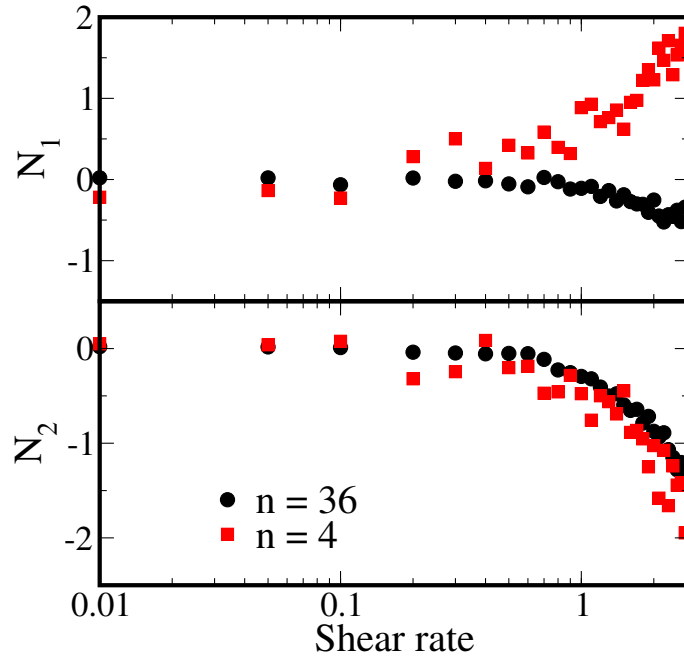
Figure 3.2: First normal stress difference (N_1) and second normal stress difference (N_2) as function of shear rate for $n = 36$ and 4.

3.3.2 Microstructure

In order to investigate how particle softness relates to the deformation of fluid structure under steady shear, pair distribution functions (PDF) at the shear plane (x-y

plane), $g(x, y)$ are constructed for each of the systems at different shear rate. Figure 3.3 shows pair distribution function $g(x, y)$ for $n = 36$ and 4. For better contrast, an upper cut-off value at $g(x, y) = 4$ and $g(x, y) = 6$ are imposed for $n = 4$ and 36 respectively. From Figure 3.3, one can see clearly the anisotropy of structure under steady shear. In general, moving from top to bottom, inner and outer rings of high-probability are being deformed and reduced therefore less identifiable, which imply that structural ordering and symmetry is attenuated with the increasing shear. At low shear rate, the structure is nearly isotropic and no angular variation in the first and second nearest-neighbor rings. As the shear rate increased, there is a buildup of particles in the compressive axis (about 135°) and a depletion of particles in the extensional axis (about 45°) as shown at $\dot{\gamma} = 1.0$ for $n = 36$ and 4. This oval-like structure is initially symmetrical along the compressive axis. As the shear further increased, the symmetry is broken by appearance of vague tails near the opening of the innermost ring that indicate the convection of probability downstream into neighboring extensional region and high-probability dots at 0° and 180° that indicates stronger correlation along flow direction. In addition, by comparing the right and left column, the quasi-hard sphere and ultrasoft cases, the ultrasoft particle shows thicker rings than quasi-hard sphere particle and the deformation of these rings with respect to shear rate is not as significant as quasi-hard sphere particles.

To see how quantitatively the shear-induced anisotropy is related to softness of particle interactions, angularly averaged PDF, $g_s(r)$, is shown as a function of shear rate $\dot{\gamma}$ for two particle softness in Figure 3.4 (upper panel). For $n = 36$, we observed a slightly sharpened nearest-neighbor peak and flatter second and third peaks with the increase of shear rate. For the cases of $n = 4$, the effect of shear on the $g_s(r)$ is to weaken both the short-range and long-range ordering as all the peaks are flattened by increasing the shear rate. To quantify the subtle changes of ordering, we exanimate the cumulative structure order I_{s_2} shown in Figure 3.4 (lower panel). For the ultrasoft
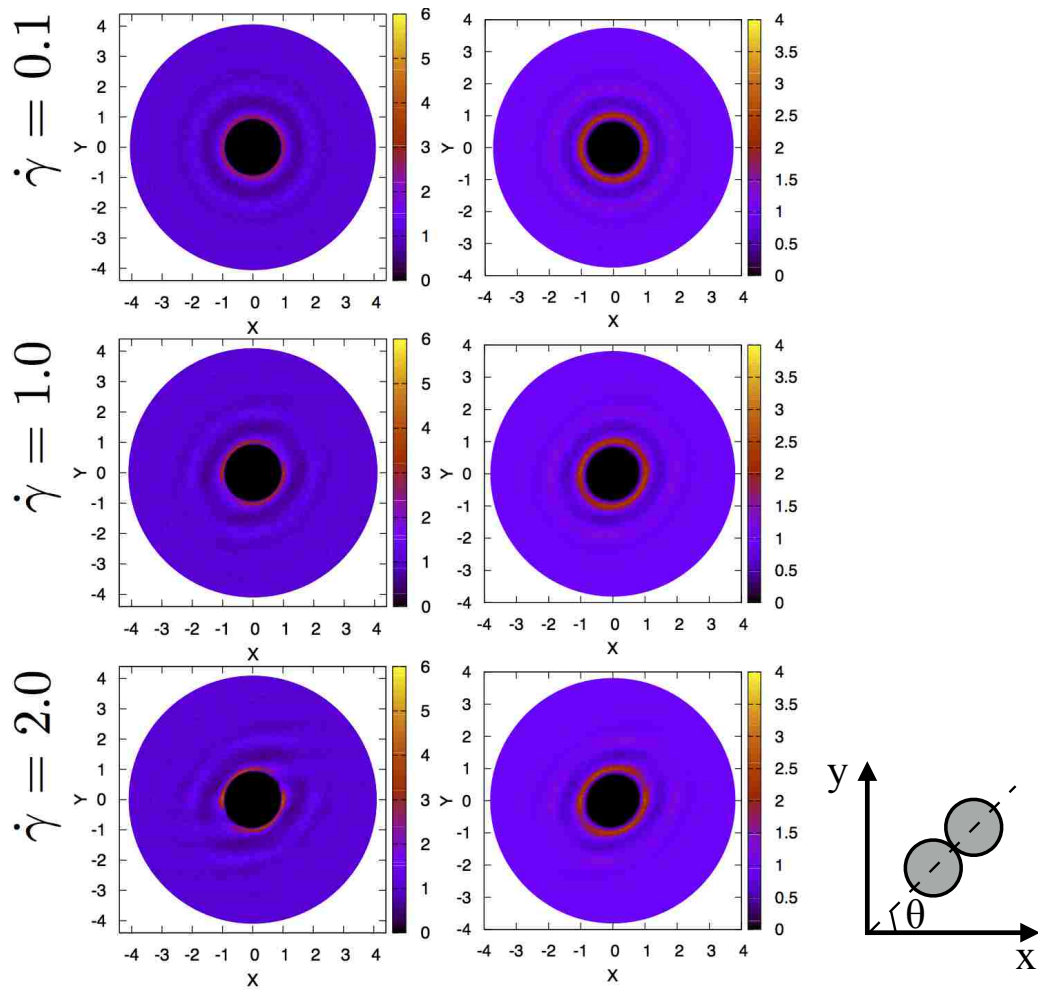
Figure 3.3: Pair distance function $g(x, y)$ for $n = 36$ (left column) and 4 (right column) at shear plane (x-y plane) at different shear rate $\dot{\gamma}$.

particles ($n = 4$), the contributions to the overall structural order by multiple peaks become less pronounced under the increased shear rate, which is denoted by both the downshift and flattening of I_{s_2} curves in Figure 3.4. For quasi-hard sphere particle ($n = 36$), the enhanced first peak make a significant contribution to the overall structural order as increased the shear rate, which make the I_{s_2} curves shift up at the point of nearest-neighbor peak.
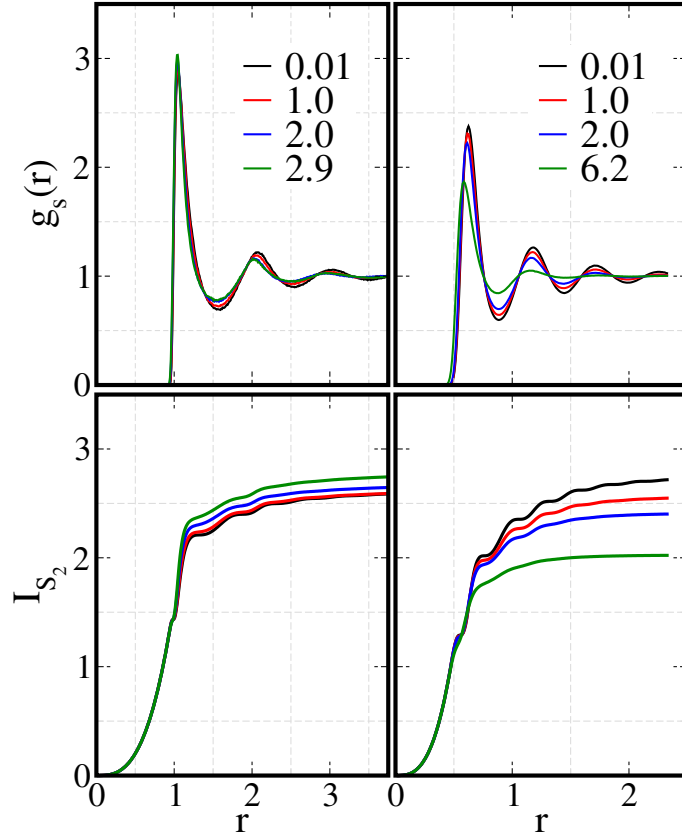
Figure 3.4: (Upper panel) Angularly averaged pair distribution function $g_s(r)$ for $n = 36$ (left column) and $n = 4$ (right column) at several shear rates. (Lower panel) Cumulative order integral $I_{s_2(r)}$ calculated corresponds to upper panel.

Recent simulations have also shown the average structure was flattened by the increase of shear rate for the Debye-Huckel repulsive potential [13], while a enhanced nearest-neighbor peak was found for hard sphere interaction [96]. Although the hydrodynamic interactions were included in their simulations, we observed the quite

similar results by NEMD, which implies that hydrodynamic interactions have no significant effect on the altering of translational order in response to shear forces. In addition, we noted that when hydrodynamic interactions are present, the enhanced nearest-neighbor correlation for quasi-hard sphere particles might facilitate the hydrocluster formation, which has been confirmed from both experiments [22, 51] and simulations [13, 15, 34, 109] as the cause of the shear thickening. For the softer particles, the decayed nearest-neighbor correlation tends to suppress the formation of hydroclusters and therefore the difficulty to observe the shear thickening.

For a better illustration of first peak variation in $g_s(r)$ under shear, the angular variations of PDF at the radius where first peak of $g_s(r)$ locates, $g(r_c, \theta)$, is shown in Figure 3.5. For $n = 36$ case, no obvious deviation from equilibrium value is found for $\dot{\gamma} = 0.01$ and 0.1. At $\dot{\gamma} = 1.0$, $g(r_c, \theta)$ display an approximately sinusoidal variation around isotropic value with the maximum and minimum located at around $\theta = 130°$ and 40°. At $\dot{\gamma} = 2.0$, secondary maximum and minimum are found at $\theta = 115°$ and 150°, with a deeper depleted correlation region at $\theta = 40°$ and enhanced correlation at flow direction. The correlation along the flow direction becomes more pronounced as the shear rate further increased combined with more clear first and secondary depletion regions.

For the ultrasoft case ($n = 4$), although similar elevation and reduction of $g(r_c, \theta)$ relative to the equilibrium value can be observed under shear, the difference from $n = 36$ is clear. At $\dot{\gamma} = 1.0$, there is no symmetrically distributed variation about minimum and maximum values of $g(r_c, \theta)$. Instead a pair of minima are found at $\theta = 40°$ and $\theta = 150°$. The enhanced correlation along the flow direction due to shearing becomes less pronounced as compared to $n = 36$. Two contact values at $\theta = 40°$ and 150° are found to be decreased with the increase of shear rate. To sum up, for $n = 36$, the area under the $g(r_c, \theta)$ curve is slightly increase with the shear rate, while for $n = 4$ the corresponding area is clearly decrease with the shear rate.

27
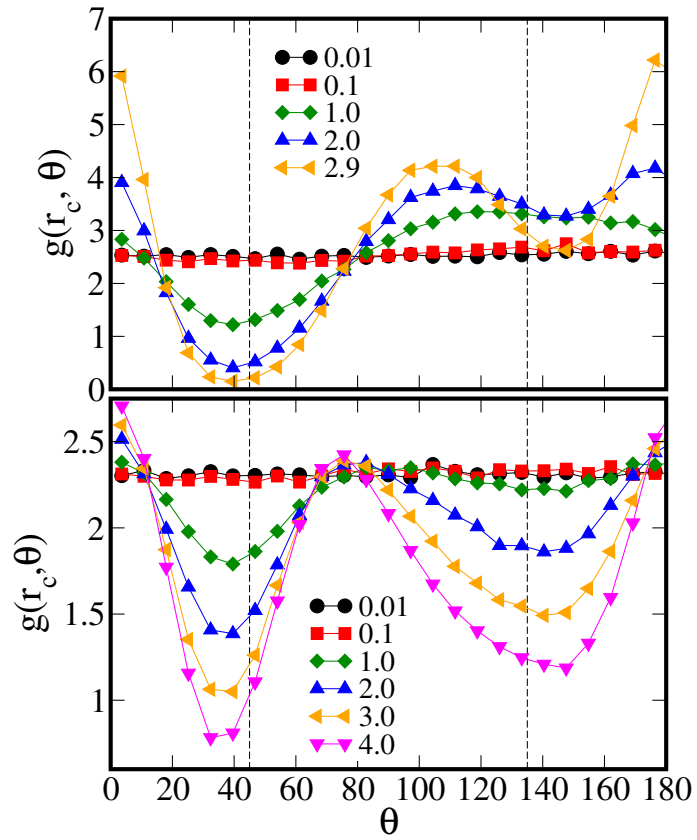
Figure 3.5: Angular variation of PDF $g(r_c, \theta)$ at the radius of first peak of $g_s(r)$ for the particle softness n=36 (upper) and 4 (bottom).

The flattened first peak for $n = 4$ is closely related to the formation of secondary depletion region at $\theta = 150°$ as well as weaker correlation along the flow direction due to the effect of particle softness.

3.4   Conclusions

Shear rheology and microstructures of particles with different softness are studied using NEMD simulations. Our results show that a universal shear-thinning behavior for particles with different softness in absence of hydrodynamics, albeit softer particles exhibit stronger shear-thinning tendency. By investigating the microstructure of these systems, we found a strong relation between the changes of the structures and the particle softness in presence of shear. These different microstructure changes in responses to the shearing might explain the extent of shear-thinning behavior for different particle softness.

Chapter 4

Coarse-grained DNA model

4.1 Introduction

DNA, a very important molecule in biological systems, is composed of sugar-phosphate backbone with four different types of bases: adenine A, thymine T, cytosine C, and guanine G. The specificity of complementary base pairing (A-T and C-G) not only determines the formation of double helical structures, but also makes DNA a useful tool for self-assembly, e.g., DNA-functionalized particles as building blocks for the assembly of nanostructures [85].

In order to understand the role of DNA in the emerging DNA nanotechnology, accurate computational models need to be developed. Quantum chemistry calculation, due to its high computational demand, has very limited applications in modeling dynamical processes involving breaking and forming of base pairs, which are the critical processes in these DNA nanotechnology. All-atom models with empirical force fields, such as the CHARMM and AMBER force fields, have been used to model transitions in small duplexes and hairpins [103]. However the minimal unit in a DNA nanotechnology typically involves tens to hundreds of DNA chains with around 10-100 nucleotides for each chain. The events, which involve chain diffusion

as well as base pair stacking, and hydrogen bonding happen at the ms timescale or even longer. As an alternative, coarse-grained (CG) models of DNA reduce degrees of freedom by replacing a group of atoms by a single site with effective interactions between CG sites. By sacrificing details at some level, these CG models allow one to study much larger systems and also for a longer time (Figure 4.1).
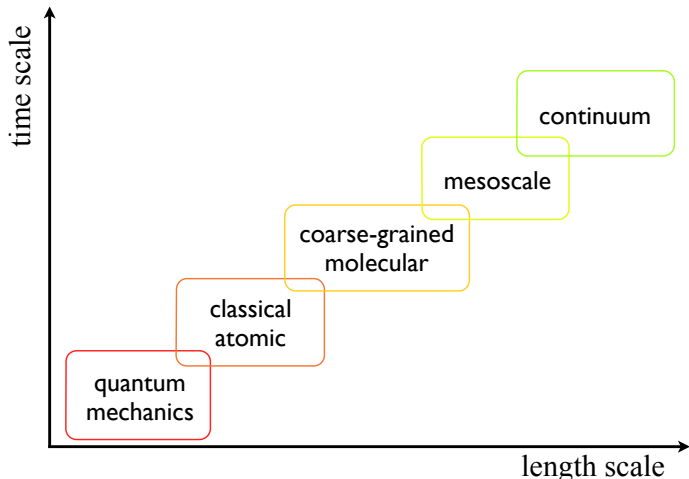
Figure 4.1: Molecular simulation scales

Numerous coarse-grained DNA models have been proposed varying in complexity [45, 52, 59, 82, 136]. These CG models typically simplify the physical structure of the nucleotide into two or three interaction sites (or beads). The base is represented by one site and then the sugar-phosphate backbone is either defined as a single or two interaction sites (i.e. one site for sugar group and the other for phosphate group). Despite the huge reduction of interaction site numbers as compared to the corresponding all-atom models, most of these CG models are still parameterized with very complicated interaction potentials involving multi-body interactions. The examples shown in the literature are limited to simulations of two or three DNA strands. The capability of simulating typical minimal unit involved in the DNA nanotechnology with these available CG models is still questionable.

In this chapter, we focus on developing CG DNA model for studying the self-

assembly of DNA-functionalized particles (DFPs). DNA provides a natural tool for directed particle assembly because of the chemical specificity of double helix formation. Particles with short single-stranded DNA, grafted on their surfaces will be bridged together if and only if those strands have complementary base sequences due to the spontaneous formation of double-stranded DNA [102, 108]. Moreover, the temperature-dependent stability of such DNA bridges allows the resulting attraction to be modulated from negligibly weak to effectively irreversible over a convenient range of temperatures [113]. The key features of the proposed CG DNA model required to successfully simulate the DNA-mediated assembly processes is to capture the dynamic processes of double-stranded DNA melting. Moreover, the coarse-grained model must be properly designed to capture the structural, thermodynamical, and mechanical properties of DNA in both the single- and double-stranded forms. Therefore in this chapter we first present a simpler coarse-grained DNA model, which is based on an earlier ssDNA model proposed by Dofman and Kenward [52], and then we introduce an advance version, which are parameterized according to previous all-atom simulation data. This new version CG model includes the properties of helix of dsDNA, angular-dependent hydrogen bonding interactions and accurate structure (i.e. diameter and length of dsDNA). The helix of backbone is induced by DNA stacking and hydrogen bonding without any extra torsional constraints

4.2 Coarse-grained DNA model in the reduced unit

4.2.1 DNA model

In order to achieve an accurate description of DNA behavior in a CG DFP model, the DNA model itself should be suitable for studying the properties of ssDNA and

dsDNA. The model proposed here is expected to include the following key aspects of DNA behavior that may be important for understanding the assembly of DFPs: (i) attractive interactions between complementary base pairs A:T and G:C, (ii) attractive interactions between adjacent bases to capture base stacking, (iii) the ability to study sequence-dependent behavior, (iv) hairpin formation in a suitable ssDNA sequence with complementary WC pairs at both ends, (v) hybridization between two fully or partially complementary strands, and (vi) no multi-strand association or aggregation in the form of large bundles.

It is also desirable to include base pair dependent non-WC interactions [128], but is something that will require extensive parameterization and testing. We plan to do this in future refinement of the model proposed here. By taking into account the requirements above, we have developed our CG model, which is based on an earlier DNA model proposed by Dorfman and co-workers [52]. Our choice is based on a compromise between computational efficiency and accurate representation of DNA behavior. Other DNA models are available in the literature, which can be computationally more efficient or physically more accurate. In our model (see Figure 4.2), a two bead representation is used for a nucleotide, one bead for the phosphate-sugar backbone and another for the nitrogenous base.

The connectivity between base and backbone beads and between adjacent backbone beads is modeled by the finite extensible nonlinear elastic (FENE) bond potential [63], which is given by

$$U_{\text{bond}}(r_{ij}) = -\frac{k_{\text{bond}}}{2} R_0^2 \ln \left[1 - \left(\frac{r_{ij}}{R_0} \right)^2 \right],$$

(4.1)

where k_{bond} is the effective strength of the potential, and R_0 is the cutoff distance at which this potential diverges. Following Kenward et $al.$, we use $k_{\text{bond}} = 30\epsilon/\sigma^2$ and $R_0 = 1.5\sigma$ here [52]. Here, ϵ is the characteristic energy scale and σ is the
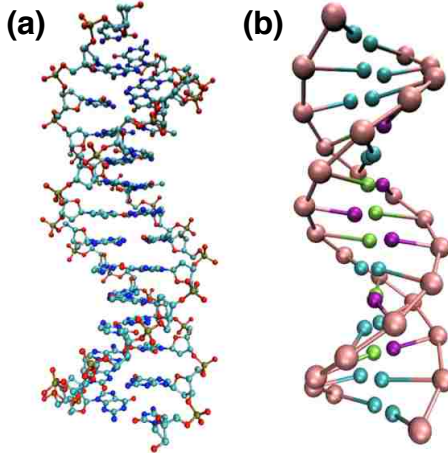
Figure 4.2: (a) All-atom model of dsDNA. (b) Two-bead coarse-grained model of dsDNA

characteristic length scale. The angle potential is used to provide additional bending rigidity to the backbone with the following functional form:

$$U_{\text{angle}}(\theta) = \frac{k_{\text{angle}}}{2}(cos\theta + cos\theta_0)^2, \qquad (4.2)$$

where θ the angle between three adjacent backbone beads, $\theta_0 = 180°$ is the reference bending angle, and $k_{\text{angle}} = 24\epsilon$ is the stiffness parameter. Inter-chain and intra-chain stacking (st) and WC hydrogen bonding (hb) attractions between DNA base beads are modeled as [52]

$$U_k(r_{ij}) = -\epsilon u_k \delta_{ij}^k \left\{ \exp\left(20\left[\frac{r_{ij}}{\sigma} - \Gamma_s\right]\right) + 1 \right\}^{-1}, \qquad (4.3)$$

where $k \in \{\text{hb}, \text{st}\}$ and Γ_s sets the range of interaction; we use $\Gamma_s = 1.5$. The interactions between possible base pairs out of the four base alphabet (A, T, C or

G) can be simply represented in a matrix form $[\delta_{ij}^k]$ as [52]

$$[\delta_{ij}^{st}] = \begin{pmatrix} \delta_{AA}^{st} & \delta_{AT}^{st} & \delta_{AC}^{st} & \delta_{AG}^{st} \\ \delta_{TA}^{st} & \delta_{TT}^{st} & \delta_{TC}^{st} & \delta_{TG}^{st} \\ \delta_{CA}^{st} & \delta_{CT}^{st} & \delta_{CC}^{st} & \delta_{CG}^{st} \\ \delta_{GA}^{st} & \delta_{GT}^{st} & \delta_{GC}^{st} & \delta_{GG}^{st} \end{pmatrix} = \begin{pmatrix} \frac{3}{4} & \frac{1}{2} & \frac{1}{2} & \frac{3}{4} \\ \frac{1}{2} & \frac{1}{4} & \frac{1}{4} & \frac{1}{2} \\ \frac{1}{2} & \frac{1}{4} & \frac{3}{4} & \frac{3}{4} \\ \frac{3}{4} & \frac{1}{2} & \frac{3}{4} & 1 \end{pmatrix}, \tag{4.4}$$

$$[\delta_{ij}^{hb}] = \begin{pmatrix} \delta_{AA}^{hb} & \delta_{AT}^{hb} & \delta_{AC}^{hb} & \delta_{AG}^{hb} \\ \delta_{TA}^{hb} & \delta_{TT}^{hb} & \delta_{TC}^{hb} & \delta_{TG}^{hb} \\ \delta_{CA}^{hb} & \delta_{CT}^{hb} & \delta_{CC}^{hb} & \delta_{CG}^{hb} \\ \delta_{GA}^{hb} & \delta_{GT}^{hb} & \delta_{GC}^{hb} & \delta_{GG}^{hb} \end{pmatrix} = \begin{pmatrix} 0 & \frac{2}{3} & 0 & 0 \\ \frac{2}{3} & 0 & 0 & 0 \\ 0 & 0 & 0 & 1 \\ 0 & 0 & 1 & 0 \end{pmatrix}. \tag{4.5}$$

In Eq. (4.3), u_k sets the relative energy scale between base stacking u_{st} and hydrogen bonding u_{hb}. We use $u_{st} = 2.5$ and $u_{hb} = 1.0$ and keep $u_{st}/u_{hb} = 2.5$ as suggested previously by Linak *et al.* [81]. The stacking potential U_{st} is only applied to adjacent bases in a DNA strand connected to backbone beads i and $i\pm1$, which are less than distance 2σ apart. The hydrogen bonding potential U_{hb} is applied between all possible WC inter-strand base pairs and intra-strand base pairs, which are less than distance 2σ apart, excluding adjacent (i and $i\pm1$) and next-nearest neighbors (i and $i\pm2$). In addition, short-range repulsive interactions between backbone-base and

base-base beads are modeled by the Weeks-Chandler-Andersen (WCA) potential as

$$U_{\text{WCA}}(r_{ij}) = \begin{cases} 4\epsilon \left[\left(\dfrac{\sigma}{r_{ij}} \right)^{12} - \left(\dfrac{\sigma}{r_{ij}} \right)^{6} \right] + \epsilon, & \text{if } r_{ij} \leq 2^{\frac{1}{6}}\sigma, \\ \\ 0, & \text{if } r_{ij} > 2^{\frac{1}{6}}\sigma. \end{cases} \tag{4.6}$$

The repulsive interactions between negatively charged backbone beads are modeled by the Yukawa potential (screened electrostatics) as [50]

$$U_{ele}(r_{ij}) = A\frac{e^{-\kappa r_{ij}}}{r_{ij}}, \tag{4.7}$$

where A is a prefactor with units of energy$\times$distance, $\kappa = 2/\sigma$ is the screening length, and $r_{\text{cut}} = 3.2\sigma$ is the potential cutoff value. In our reduced unit model, the actual strength of electrostatic interactions ($A = 100\ \epsilon\sigma$) is selected so as to prevent triple- or multi-strand aggregation as shown in Figure 4.3. The undesired aggregation of multiple DNA strands results from the absence of electrostatic repulsion between backbone beads, whereas well-separated dsDNA pairs form in the presence of such repulsion modeled as the Yukawa interaction potential, Eq. (4.7). We note that aggregation of multiple DNA strands can also be avoided by accounting for the directional nature of hydrogen bonding interactions between DNA base beads with a multi-body interaction potential instead of the isotropic distance dependent potential given by Eq. (4.3). To account for electrostatic interactions in a more transparent manner, we are currently developing a DNA model in real units with appropriate size scaling for the backbone and base beads as well as disparate bond lengths for backbone-backbone and base-backbone bonds [14]. No attempt is made here to convert the reduced simulation units to SI units as was done previously by Linak et al. [80, 81] for the temperature based on the experimental data. Without significant experimental input, such a mapping will likely yield inconsistent results.
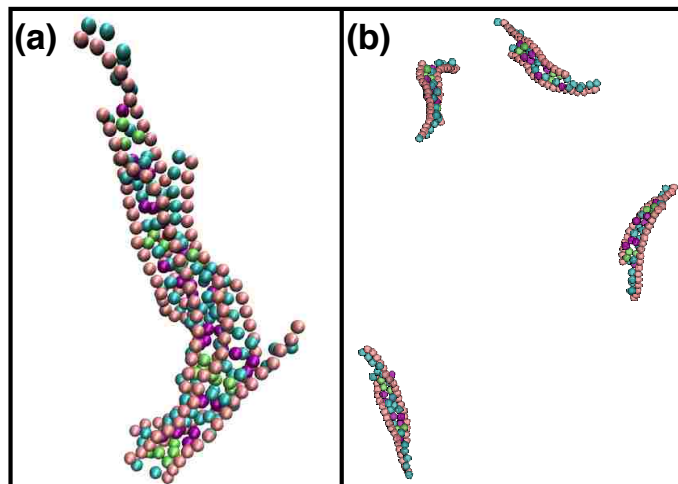
Figure 4.3: Simulation snapshots of four pairs of partially complementary DNA sequence without (a) and with (b) the Yukawa interaction potential temperature below the DNA melting temperature.

4.2.2 Results

In order to validate the CG DNA model, we first present the simulation data to characterize the melting behavior of ssDNA and dsDNA. The melting temperature is identified as the temperature at which the heat capacity (calculated from potential energy fluctuations) shows a maximum, the so-called calorimetric definition [56]. We also use a structure based definition to define melted or unhybridized states. We define ssDNA hairpin or dsDNA duplex configurations to be hybridized (Figure 4.4) if at least a certain number of the possible complementary base pairs are bonded. Up to a certain threshold value of number of bonded pairs, the melting curves are quite similar. The melting temperature, identified from this structure based criteria as the temperature at which 50% of the states are melted, is similar to the calorimetric definition based on the heat capacity.

Figure 4.5 shows the melting curves for a ssDNA hairpin: $A_{10}G_{20}T_{10}$ and a dsDNA S1S2: GCGTCATACAGTGC obtained from REMD simulations. The shape of these melting curves is similar to what is expected based on thermodynamic melting behavior of hairpins and dsDNA formation from experiments [106, 144], although the
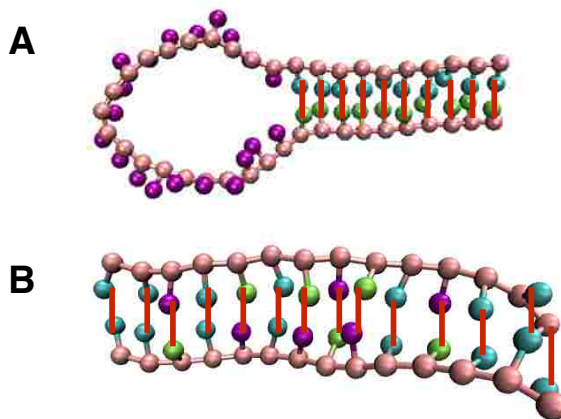
Figure 4.4: Illustration of the hydrogen bonds formed between the stem bases of a hairpin ($A_{10}G_{20}T_{10}$) and dsDNA (S1S2: GCGTCATACAGTGC). The red lines represent hydrogen bonds formed between the bases.

widths of the melting transitions are much broader as found by Linak et al. [80, 81] as well for a similar model as used here. Such broad transitions (unphysical) are also found in more detailed atomistic models of biomolecular systems such as proteins [10]. From Figure 4.5 we observe that at very low temperatures almost all states are found to be hybridized and at high temperatures all states are melted. The transition between these two states is occurring in a cooperative manner, more so in the case of dsDNA. The temperature at which the fraction of melted states equals the fraction of hybridized states can be defined as the melting temperature. We note that the melting curve obtained from simulation of a single pair of duplex in the canonical ensemble is different from the bulk experimental situation involving hybridization between many pairs of complementary strands, due to finite-size effects, as discussed in detail by Ouldridge et al. [104, 105] If a comparison between simulation data from a finite system and experiment is desirable, melting temperature can be estimated as the temperature at which 33% of states are melted, as opposed to 50%. We also note that in the case of dsDNA hybridization, the melting temperature is also a function of the DNA concentration or simulation box volume for a fixed number of DNA strands.

Figure 4.5: Thermodynamic melting behavior. The fraction of melted states as a function of temperature (red symbols) (and typical DNA configurations) and heat capacity (black symbols) are shown for (a) a ssDNA hairpin:$A_{10}G_{20}T_{10}$ and (b) a pair of dsDNA S1S2:GCGTCATACAGTGC.

Based on the results above, the CG DNA model is expected to capture the essential thermodynamics of dsDNA hybridization and ssDNA properties. Specifically, cooperative transitions between hybridized and unhybridized states for dsDNA and ssDNA, as a function of temperature are captured.

4.3 Coarse-grained DNA model in the real unit

4.3.1 DNA model

The advanced version of CG DNA model proposed here is mainly based on previous ladder-like model, which is relatively simple yet accurately portrays the dynamics and denaturation of DNA. We designed our new CG model in the real unit to facilitate the direct comparison with available experiment data. In order to save the computational cost, the model is still a bead-spring type model that divides the nucleotide into two beads. One bead represents the sugar-phosphate backbone and the other represents the base. We parameterized the base interactions according to the previous all-atom model studies by our group, which contains a more accurate quantification of different base interactions. The anisotropic nature of the hydrogen bonds are included in this model, which combined with stacking interactions induces the helix structure of double-stranded DNA. This new model also differentiates the backbone-backbone bond length and the backbone-base bond length, which is also important for double helix formation. We note this model does not differentiate between bases in size, mass, or bond length to backbone. It also does not differentiate between the backbone beads and the base beads in terms of mass or size.

The overall potential energy in the model is defined as the sum of each interaction:

$$U_{\text{total}} = U_{\text{st}} + U_{\text{hb}} + U_{\text{WCA}} + U_{\text{bond}} + U_{\text{angle}} + U_{\text{ele}} \tag{4.8}$$

The stacking interactions of adjacent bases are modeled as 12-10 Lennard-Jones potential:

$$U_{\text{st}}(r_{ij}) = \epsilon_{ij} \left[5 \left(\frac{\sigma_{\text{st}}}{r_{ij}} \right)^{12} - 6 \left(\frac{\sigma_{\text{st}}}{r_{ij}} \right)^{10} \right]. \tag{4.9}$$

The Watson-Crick (WC) hydrogen bonding potentials between complementary base pairs (A:T and C:G) are also represented by 12-10 type Lennard-Jones potentials with the exception of additional modulating function $f(\theta)$ to account for the angular dependence of hydrogen bonding.

$$U_{\text{hb}}(r_{ij}) = \begin{cases} \epsilon_{ij} \left[5 \left(\frac{\sigma_{\text{hb}}}{r_{ij}} \right)^{12} - 6 \left(\frac{\sigma_{\text{hb}}}{r_{ij}} \right)^{10} \right] + \epsilon_{ij}[1 - f(\theta)] & \text{if } r_{ij} \leq \sigma_{\text{hb}}, \\[2em] \epsilon_{ij} f(\theta) \left[5 \left(\frac{\sigma_{\text{hb}}}{r_{ij}} \right)^{12} - 6 \left(\frac{\sigma_{\text{hb}}}{r_{ij}} \right)^{10} \right] & \text{if } r_{ij} > \sigma_{\text{hb}}, \end{cases} \tag{4.10}$$

where

$$f(\theta) = \begin{cases} 0 & \text{if } 0 \leq \theta \leq \pi/3, \\[1em] |cos(3\theta/2)| & \text{if } \pi/3 \leq \theta \leq 2\pi/3, \\[1em] 1 & \text{if } 2\pi/3 \leq \theta \leq \pi. \end{cases} \tag{4.11}$$

The θ is defined as an angle formed by two vectors, each of which is composed of a hydrogen-bonded base and its connected backbone bead. The stacking potential U_{st} is only applied to adjacent bases in a DNA strand connected to backbone beads i and $i\pm1$. The hydrogen bonding potential U_{hb} is applied between all possible WC inter-strand base pairs and intra-strand base pairs excluding adjacent (i and $i\pm1$) and next-nearest neighbors (i and $i\pm2$). The parameters of the hydrogen bonding and stacking interactions between possible base pairs out of the four base alphabet (A, T, C or G) are listed in Table 4.1. The ϵ_{ij} and $\sigma_{\text{st/hb}}$ correspond to the minimum value of the

12-10 Lennard-Jones potential and the distance where the minimum occurs. All the values of ϵ_{ij} and $\sigma_{\text{st/hb}}$ listed in Table 4.1 are derived from all-atom simulations using the CHARMM27 force field by coupling umbrella sampling with Hamiltonian replica exchange from the previous study [128]. In that study, the constructed potential of mean force (PMF) between possible base pairs in the bulk mimic the Lennard-Jones type potential, which lead to the choice of 12-10 Lennard-Jones potential with values of ϵ_{ij} and $\sigma_{\text{st/hb}}$ matching the minimum and corresponding distances of PMFs. We note the ϵ_{ij} in the Table 4.1 represent the values taken from the all-atom data. In order to make them more robust for the propose of simulation, these values are scaled with respect to the maximum counterpart (i.e. for stacking, all the ϵ_{ij} are scaled with respect to the value of G:G pair and for hydrogen bonding, all the ϵ_{ij} are scaled with respect to the value of G:C pair). The anisotropic nature of the hydrogen bonds also greatly diminishes the actual strength of hydrogen bonding interactions. The relative strength between stacking and hydrogen bonding interactions are tuned to provide the greatest representation of the physical nature of the system (i.e. structural stability, melting transition). Finally, the cutoff distances for stacking and hydrogen bonding interactions are chosen to be 6.5 Å and 9.5 Å respectively, where the both interactions diminish almost to zero.

The connectivity between base and backbone beads and between adjacent backbone beads is modeled by the harmonic bond potential:

$$U_{\text{bond}}(r_{ij}) = k_{\text{bond}}(r_{ij} - r_0)^2. \tag{4.12}$$

The three-body angle potential is applied to the backbone beads is defined by the harmonic angle potential:

$$U_{\text{angle}}(\theta) = k_{\text{angle}}(\cos\theta - \cos\theta_0)^2. \tag{4.13}$$

Table 4.1: Parameters for base pair interactions

	Stacking			Hydrogen bonding	
base pair	ϵ_{ij}	σ_{st}	base pair	ϵ_{ij}	σ_{hb}
AT	4.05	3.6	AT	2.82	6.0
CG	4.04	3.8	CG	3.49	5.5
AA	4.60	3.6			
AC	4.02	3.6			
AG	4.80	3.6			
CC	2.97	3.7			
CT	3.37	3.8			
GG	5.25	3.6			
GT	4.26	3.6			
TT	3.65	3.7			

Electrostatic interactions are applied to backbone beads to account for the negative charge on the phosphate group based on the Debye-Huckel approximation, which assumes the high salt concentrations:

$$U_{\text{ele}}(r_{ij}) = \frac{q_i q_j}{4\pi\epsilon_0\epsilon_k r_{ij}}e^{-r_{ij}/\kappa} = \frac{A}{r_{ij}}e^{-r_{ij}/\kappa}, \tag{4.14}$$

where

$$\kappa = \left(\frac{\epsilon_0\epsilon_k RT}{2N_A^2 q_e^2 I}\right)^{0.5}. \tag{4.15}$$

This interaction is only applied to the backbone beads that are not bonded or not part of the same angle. In addition, short-range repulsive interactions between backbone-base and base-base beads are modeled by the Weeks-Chandler-Andersen (WCA)

potential as:

$$U_{\text{WCA}}(r_{ij}) = \begin{cases} 4\epsilon\left[\left(\dfrac{\sigma}{r_{ij}}\right)^{12} - \left(\dfrac{\sigma}{r_{ij}}\right)^{6}\right] + \epsilon & \text{if } r_{ij} \leq 2^{1/6}\sigma, \\\\ 0 & \text{if } r_{ij} > 2^{1/6}\sigma. \end{cases} \tag{4.16}$$

The addtional parameters for potentials used in this study are tabulated in Table 4.2.

Table 4.2: Values of parameters for potential energy functions

Parameter	Value	Unit
σ	5.5	Å
ϵ	4	kcal/mol
k_{bond}	50	kcal/mol/Å^2
$r_{\text{bb-b}}$	5.75	Å
$r_{\text{bb-bb}}$	5.5	Å
k_{angle}	80	kcal/mol
θ_0	180°	
A	4.243	kcal/mol
$\kappa_{120\text{mM}}$	8.8	Å
$\kappa_{50\text{mM}}$	13.6	Å
$\kappa_{20\text{mM}}$	21.5	Å

4.3.2   Results

4.3.2.1   Melting behavior of dsDNA

Here we study the melting transition of our CG DNA model using sequence of $S1S2$, whose melting behavior has been studied experimentally in several salt solutions. Figure 4.6 shows simulated results for the fraction of melted states and corresponding heat capacity as a function of temperature for $S1S2$ at three salt concentrations.

Parameterization are only based on $[Na^+] = 120$mM. The curves at other salt concentrations, as well as all other simulation results presented hereafter, represent predictions of the model. Since the model are parameterized to reproduce melting data at $[Na^+] = 120$mM, the melting temperature obtained from simulation at this salt concentration is, by construction, in agreement with experiment. However, the simulated results are also in close agreement with the melting temperatures for other salt concentrations (Table 4.3). Although the simulated melting transition is slightly broader than its experimental counterpart, this phenomenon is common in coarse grain approaches, and the discrepancy in this case is minor compared to that of our previous ladder-like model. We note our parameterization is based on very limited data set: S1S2. In order to improve the accuracy of prediction by our CG model, a large data set (i.e. hundreds of dsDNA sequences) should be used to select the parameters by minimizing the discrepancy between predicted melting temperatures (from experiment data or thermodynamic calculations) and simulated temperatures.
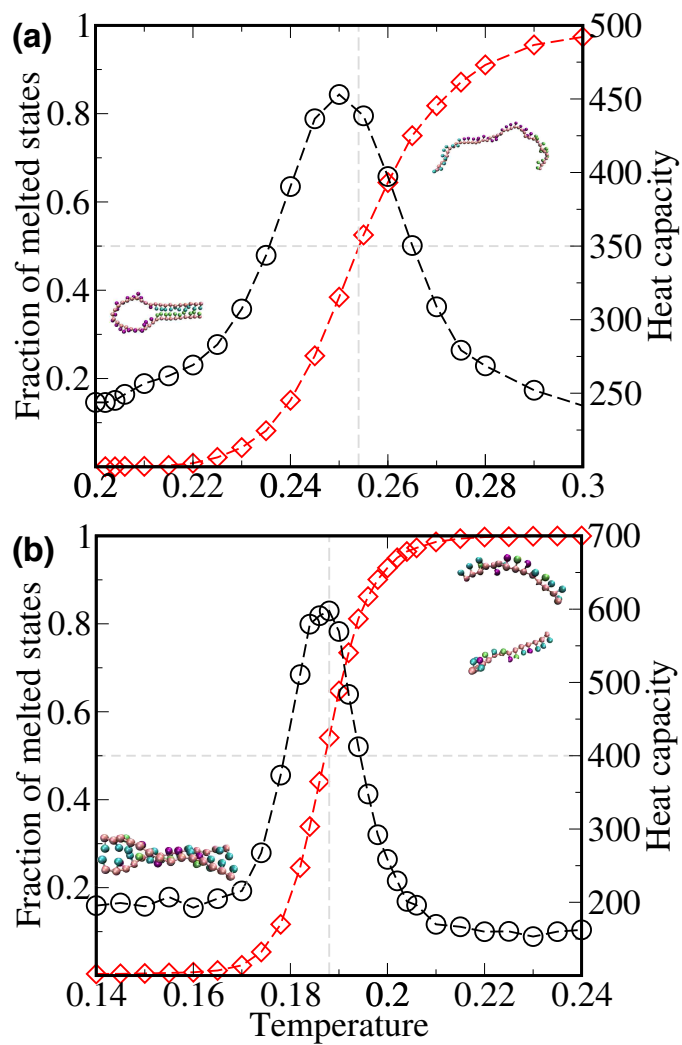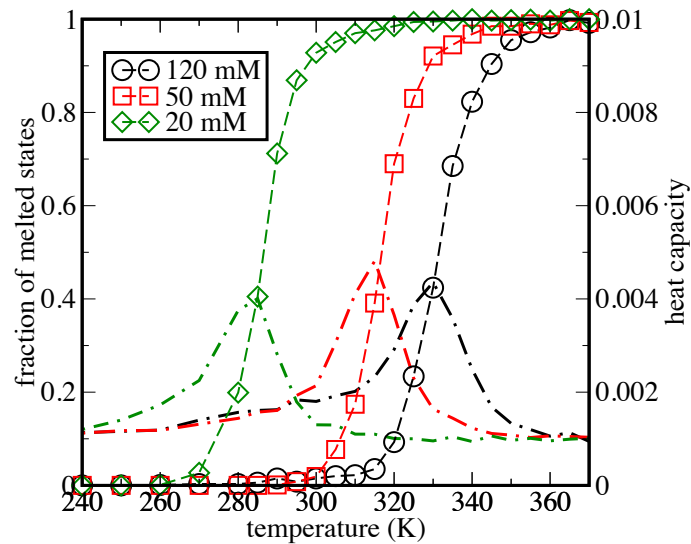

Figure 4.6: Thermodynamic melting behavior. The fraction of melted states as a function of temperature (symbols) and heat capacity (dashed lines) are shown for a pair of dsDNA S1S2:GCGTCATACAGTGC at three salt concentrations.

Table 4.3: Melting temperatures of S1S2 at different salt concentrations from experiments, thermodynamic prediction and simulation

	Melting temperature (K)		
$[Na^+]$ (mM)	Experiment	Prediction	Simulation
120	333.2	323.0	331.4
50	328.5	316.7	316.1
20	321.0	310.1	285.2

4.3.2.2 Structure of dsDNA

Our CG DNA model not only exhibits reasonable hybridization-melting thermodynamics, but also spontaneously forms B-form like dsDNA over a wide range of temperatures. We used dsDNA sequences of $S1S2$, containing 14 base pairs and performed simulations at 16 different temperatures from 180 K to 390 K. We found that within the temperature range that stabilizes dsDNA structure, right-handed helices are formed in 48% of the structures and the remaining are left-handed helices. This result is reasonable since our model has no built-in handedness; the formation of either left-handed for right-handed helices should has equal probability. In Figure 4.7, we provide two snapshots of the dsDNA configuration from our simulations, which shows the left-handed and right-handed helical dsDNA.

B-DNA has about 10 bases per turn. For the 14 base pair helix, it has less than 1.5 turns. From Figure 4.7, our dsDNA has about 12 bases per turn. We attribute this discrepancy to the limitation of one-bead representation of backbone. Since our model has no torsional constraints that favor helical structures and the helix is solely induced by stacking and anisotropic hydrogen bonding, the energy penalty due to bending and torsion of backbone is higher than for example two-bead representation of backbone. The decrease of the rigidity of backbone helps dsDNA structure but disrupts the ssDNA structure and leads to clumped states.
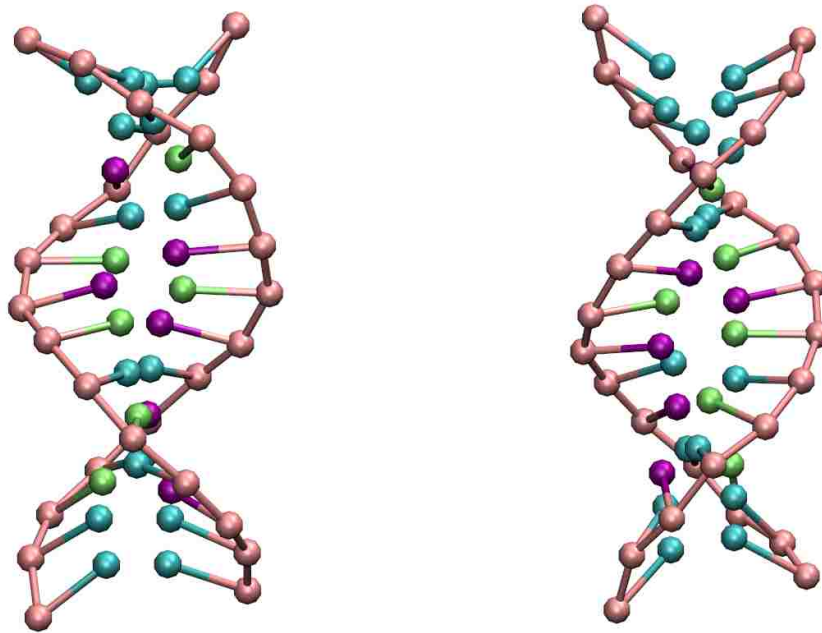
Figure 4.7: Left-handed (left) and right-handed (right) helical dsDNA.
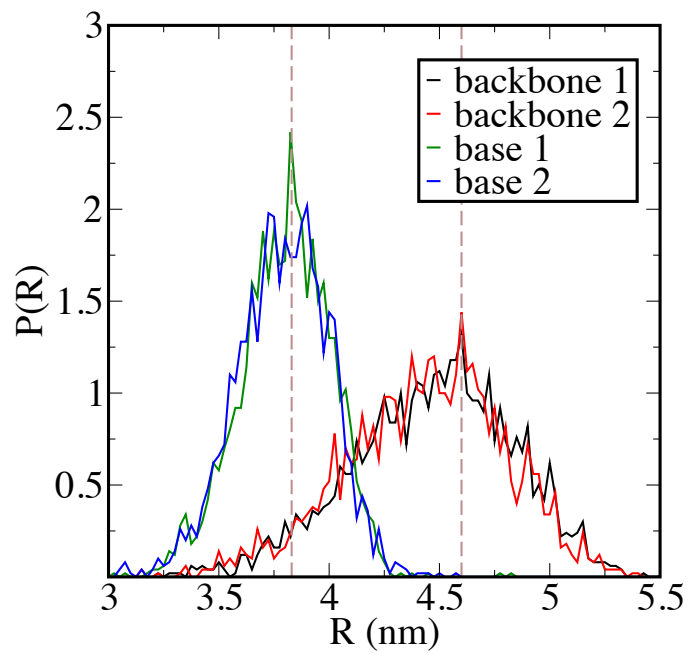
Figure 4.8: The distribution of end-to-end distance (R) of dsDNA.
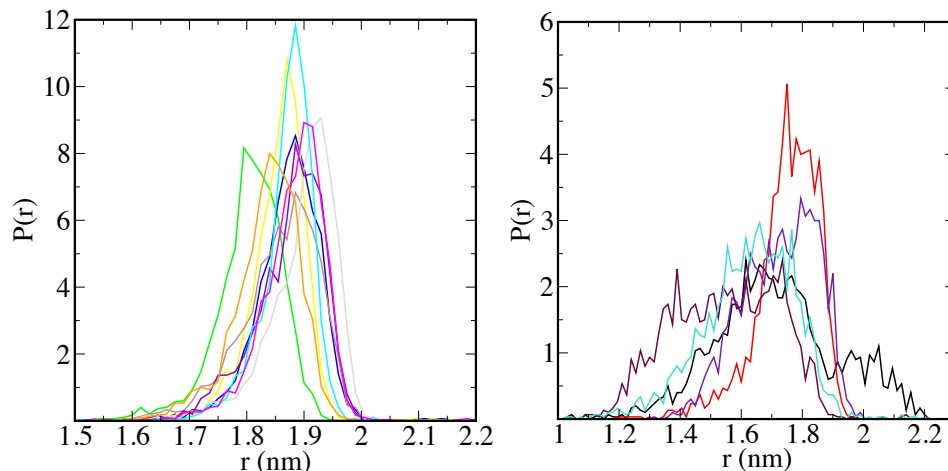
Figure 4.9: The distributions of distances between backbones. (a) backbone pairs at center of the DNA chain. (b) backbone pairs at two ends of the DNA chains

Figure 4.8 shows the distribution of end-to-end distance (R) of dsDNA. The end-to-end distributions are computed based on both base and backbone beads for each of the two ssDNA that hybridized into dsDNA. Depending on the reference bead (base or backbone), we obtained end-to end distance of 3.83 nm (base-to-base), 4.6 nm (backbone-to-backbone). We also estimate the diameter of our dsDNA by computing the distributions of distances between a pair of backbones that connected to the hybridized bases in Figure 4.9. The distributions are relatively narrow for backbone beads located at center of DNA chains comparing to those at two ends of DNA chains. This observation is related to the so-called fraying of the terminal base pairs. Our estimation of diameter of dsDNA is about 1.8-1.9 nm. These structures are essentially unchanged whether they are the left-handed or right-handed helices, because the potentials are symmetric with respect to the handedness. The comparison of structure data between our simulations and experiments are tabulated in Table 4.4. Although these numbers are not exactly same, they are within reason despite not require Gö-type structural terms such as a forced dihedral. The structural representation is also assisted by the anisotropic nature of the hydrogen bonding which more closely represents reality. This along with the short stacking

distance coupled with the longer backbone-backbone bond length gives the B-DNA like structure its helical shape.

Table 4.4: Structure data for dsDNA

Property	Experiment	Simulation
Base pairs per turn	10-10.6	12
diameter (nm)	2.0	1.8-1.9
length (nm)	4.76	4.6

Chapter 5

DNA-mediated interparticle interactions

5.1 Introduction

It is now well recognized that self-assembly of particles functionalized with biomolecules is a promising way to form unique nanostructured materials [37, 88]. The distinct advantage of inter-particle interactions mediated by DNA molecules is the specificity of Watson-Crick (WC) pairing [3, 90]; the functionalized particles can be bridged together either by direct hybridization of complementary single-stranded DNA (ss-DNA) molecules (sticky end) or indirectly via "linker" DNA molecules that can bind simultaneously to the complementary ssDNA sequences on two different particles [37]. While significant progress has been made in recent years, the fundamental details of DNA-mediated particle assembly are not very well understood [37, 88]. Specifically, the assembly of micron-sized particles into crystalline structures is still quite challenging, though nanoparticles have been assembled into a wide variety of periodic arrangements via DNA-mediated interactions [85, 102, 108].

Computer simulations can provide a convenient route to explore the large parame-

ter space of DNA-functionalized particles (DFPs), which can be useful for developing basic understanding and to test existing theoretical design models [75, 85, 94, 132]. Using all-atom models to study the properties of DFPs is still beyond the current state-of-the-art computational capabilities [69, 70, 100]. Simple and accurate coarse-grained (CG) models are, therefore, needed to overcome existing computational challenges and are actively being developed. Starr and co-workers [26, 46, 47, 107, 141] have developed a "two-bead" DFP model in which each nucleotide is represented by two force sites, one for the phosphate-sugar backbone and one for the nitrogenous base. The backbone beads are connected by the standard finite extensible nonlinear elastic (FENE) bond potential. The beads representing the nucleotide bases are also connected to the backbone beads by the FENE potential. To model WC pairing, the 12-6 Lennard-Jones (LJ) nonbonded potential between complementary bases is used. The particle itself is modeled as a single spherical or icosahedral core for simplicity. This model has extensively been applied to understand nanoparticle dimers, the stability of nanoparticle crystals, polymorphism, equilibrium clustering and dynamics [26, 46, 47, 107, 141]. Seifpour *et al.* also proposed a modified model based on this model and applied it to study the effect of DNA strand composition and sequence on the structure and thermodynamics of DFPs [126].

Li *et al.* [76, 77] recently introduced a CG DFP model which is based on an earlier model by Travesset *et al.* [57, 58]. In this model, the DNA molecule is made up of three parts: single-stranded DNA, double-stranded DNA (dsDNA), and a "sticky end". Connected beads of different sizes are used to represent ssDNA and dsDNA. The sticky end is modeled by multiple beads to take into account the selectivity and directionality of hydrogen bonding between complementary DNA bases. With this model, Li *et al.* reproduced all nine crystal structures observed experimentally by Macfarlane et al. [85], and also proposed new linker sequences for future experiments. Frenkel and co-workers [75, 86, 87, 94] have developed a CG "core-blob" DFP model

by further reducing the DNA degrees of freedom. In their model, the sticky end of tethered DNA is modeled as a blob connected to an effective spherical core. This model can capture several important features of DNA-mediated particle assembly, from pair-particle interactions [75] to thermodynamic phase transitions [86, 94].

When moving from the CG model with explicit DNA-like chains to a simplified core-blob model, the structural and chemical details of DNA molecules are gradually lost. Although it is obvious that significant coarse graining is needed to explore DFP system behavior (in particular spontaneous crystallization), certain molecular details, which are often ignored in these previous models, are important to understand DNA-mediated particle assembly. For example, most current models use an average base representation (ignoring the differences between A:T and G:C pair interactions), thereby neglecting the dependence of particle interactions on the DNA sequence. Not only is the difference between strengths of G:C pairing (stronger due to the presence of three interbase hydrogen bonds) compared to A:T pairing (two interbase hydrogen bonds) important, but the actual DNA sequence can also affect properties of hybridized DNA molecules [126, 136]. In addition, it has been reported that in order to capture surface-adsorbed or interfacial DNA structure, one needs to account for non-WC base pairing as well, since dsDNA melting and ssDNA properties will be affected by these additional interactions [82, 119, 120, 128]. Base stacking interactions, which drive the coplanar alignment of neighboring bases, are also important to the overall stability of helical duplexes and are also sequence-dependent [149]. Furthermore, the intra-particle interactions, which are the interactions between DNA strands on the same particle, are often ignored but can be quite important for particle diffusion and kinetics of assembly [24].

In this chapter, we present a new CG DFP model in which we use a two-bead representation for each nucleotide of tethered DNA molecules. The DNA model, as described in section 4.2, displays typical experimentally observed temperature

melting behavior for dsDNA hybridization and ssDNA hairpin formation. The DNA strands are connected to spherical particle cores (made up of smaller point particle beads) by FENE bonds to simulate DFPs. We use this model to study the potential of mean force (PMF) between two DFPs as a function of DNA grafting density, spacer length, sticky end length, and temperature. The results presented in this paper suggest that this new DFP model can be useful for studying the thermodynamics and kinetics of particle assembly mediated by DNA hybridization.

5.2   Model and simulation details

5.2.1   Coarse-grained model for DNA-functionalized particle

The model of DNA is described in details in Chapter 4.2, which is formulated in the reduced unit and exhibits a ladder-like structure for dsDNA. The particles are modeled as rigid body hollow spheres (radius 5σ used throughout this work), and each particle is made up of 100 beads uniformly distributed on the surface of a sphere [1]. The particle beads are uncharged and interact with DNA and other particle beads via the WCA interaction potential. Single strand DNA molecules are covalently linked to the particle surface beads by the FENE bond potential. We select particle surface beads that are farther than a certain distance value, which varies with DNA grafting density, to ensure uniform distribution of DNA strands on the particle surface. Figure 5.1 shows a snapshot of two CG DFPs with several ssDNA molecules attached at random locations to the particle surface. In our model, DNA molecules that are attached to the same particle can interact via the WC base pair interactions, in contrast to previous CG DFP models that neglect intra-particle base pair interactions even between A:T and G:C base pairs. Therefore, appropriate DNA sequences in our model can form hairpin or loop structures, which have been proposed as ideal candidates for novel design schemes [5, 72, 73, 74]. Both inter-
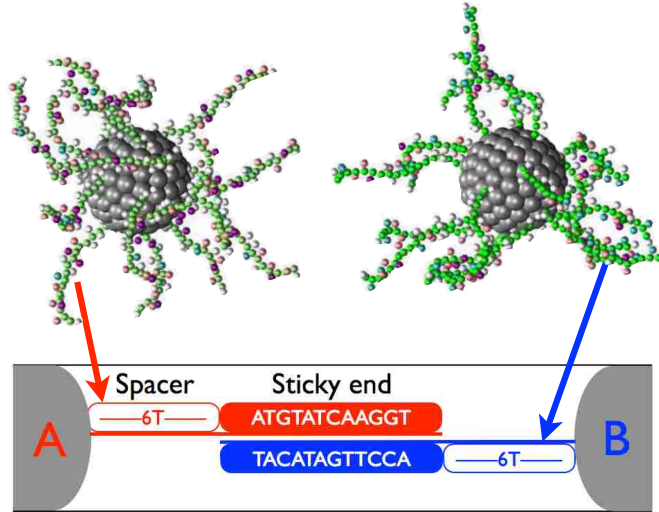
Figure 5.1: Coarse-grained DNA functionalized particle model. Two particles with multiple DNA molecules attached to the particle surface atoms are shown. The DNA sequence is composed of two parts, the spacer (6T: TTTTTT) and the sticky end as shown in the schematic.

particle and intra-particle base pair interactions are naturally incorporated in our CG DFP model.

5.2.2 Simulation details

To enhance equilibrium sampling, the replica exchange molecular dynamics (REMD) method is used for all of our simulations [135]. REMD simulations are carried out under the canonical ensemble using a Langevin thermostat with damping parameter $\tau = 1 \; (\epsilon/m/\sigma^2)^{-1/2}$ in a cubic simulation box with periodic boundary conditions in all directions. The size of the simulation box is chosen to be 100σ so that there are no interactions between molecules and their periodic images. In our REMD simulations, we typically use 16 to 48 temperature replicas to obtain sufficient exchange probability and, therefore, convergence. The replica temperatures were chosen by trial and error such that the potential energy distributions adjacent replicas overlap sufficiently to ensure exchange between any two adjacent replicas with at least 50% probability. The total number of timesteps that we performed for each simulation

is of the order of 10^8 steps with a step size of $\Delta t = 0.01 \ (\epsilon/m/\sigma^2)^{-1/2}$. About 10^8 timesteps per replica are required to obtain a reasonable estimate of the melting profiles of the hairpin and the duplex, which takes approximately 144 hours of processor time (for 32 replicas) on the Lehigh computing server corona (corona.cc.lehigh.edu) equipped with AMD Opteron 8-core 6128, 2GHz processors. For DFPs, we need about 5×10^8 timesteps per replica, requiring approximately 2304 hours of processor time (for 32 replicas) on the Lehigh computing server corona.

DFPs are placed randomly inside the simulation box. The initial part of the simulation is discarded as equilibration, and the equilibration length is decided based on observables such as number of hydrogen bonds and distance between the particles. The equilibration length for DFPs is about 10^8 steps. We use the block averaging scheme to estimate errors by dividing the production data into three sets and calculating the standard deviation from the mean.

When simulating DFPs, we also tested to ensure that results remain unchanged with a box size of 200σ. For the larger box size, we find it useful to employ umbrella sampling simulation [139] to obtain free energies as a function of pair distance between particles in a reasonable time. This also helps validate results obtained from REMD simulation. For umbrella sampling, we use harmonic umbrella potential with spring constant $= 5.0 \ \epsilon/\sigma^2$ along the pair distance between the particles with a sufficient number of copies to obtain overlap between distance distributions.

Finally, we have used two different pairs of complementary DNA sequences in our simulation [11, 113]: a 12-mer, long sticky end (TTTTTTATGTATCAAGGT and TTTTTTACCTTGATACAT) and a 7-mer, short sticky end (TTTTTTTTTTTGTC-TACC and TTTTTTTTTTTGGTAGAC).

5.3 Results

Since attentive control of particle interactions is needed to obtain ordered structures, several previous efforts have been focused on understanding pair interactions between DNA-functionalized particles. On the experimental side, Crocker and co-workers measured DNA-mediated pair interactions between micron-sized particles [12, 113]. The separation distances between particles were obtained by confining two DFPs in harmonic potentials in an optical tweezer setup. The pair interaction potential (or free energy as a function of distance) is then obtained by the Boltzmann relation, accounting for optical forces. These direct measurements have allowed the development of statistical physics-based theoretical models for understanding the underlying physical phenomena [113] of interactions between micron-sized particles. Though experimentally very challenging, it is desirable to obtain such information for interactions between nanoparticles as well.

Estimates of pairwise interactions between nanoparticles have been obtained by simulation with the help of CG DFP models [68, 138]. These previous studies consider pair interactions between DFPs for very low DNA grafting densities of 4 to 6 DNA molecules per particle. Frenkel and co-workers [94, 142] have developed numerical schemes to extract pair interactions using their core-blob DFP model with a combination of statistical mechanics theory and Monte Carlo simulations. Our new DFP model presented here is meant to act as a bridge between the core-blob type simplified description (which is computationally tractable even for phase behavior calculations) and experiment by including a more detailed description of DNA degrees of freedom (see section IIA). Ultimately, it may turn out that some of these details are not necessary to capture essential details of DFP assembly thermodynamics, including phase diagrams. But we anticipate that some of these additional details in our model may be important for understanding issues related to particle

56

dynamics and the kinetics of assembly.

We simulate two DFPs grafted with either the 12-mer long sticky end or the 7-mer short sticky end as described previously. The potential of mean force (PMF) or free energy as a function of pair distance between two DFPs, with respect to unhybridized particles, is calculated as

$$\Delta F_I(r) = -k_B T \ln[g(r)] + c, \tag{5.1}$$

where $g(r)$ is the pair correlation function (normalized with respect to an ideal gas), k_B is the Boltzmann constant, c is an additive constant, and I is used to identify particle types in a pair, i.e., $I = \{\text{A-A}, \text{B-B}, \text{A-B}\}$. In addition to binning data collected at a single temperature in an REMD simulation, we also use the weighted histogram analysis method (WHAM) [65, 131] to combine data from all of the temperatures to obtain PMFs.

5.3.1   Effect of temperature

Figure 5.2 shows a representative set of PMFs for different temperatures (see legend) between three possible pairs of particles (A-A, B-B, and A-B). The symbols represent data from the REMD simulations sampled at a single temperature, and the lines are the WHAM reconstruction based on the data from all temperatures. The agreement between the two estimates clearly indicates that the simulation times are long enough to obtain PMFs. The interactions between like pairs (A-A and B-B) are purely repulsive at all of the temperatures, as shown in Fig. 5.2b, as these ssDNA sequences were designed to have minimal self-interactions. Moreover, the repulsive interactions between like pairs are independent of the temperature, except at very low pair distances.

The PMFs between unlike particle pairs (A-B), which are coated with comple-
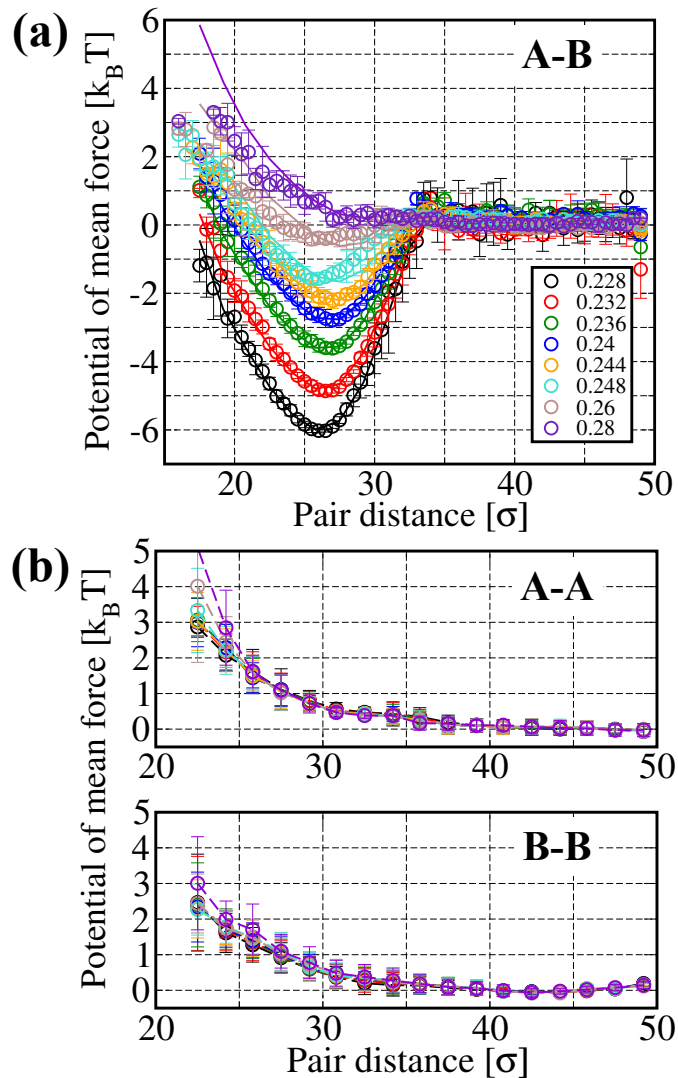
Figure 5.2: Potential of mean force (PMF) calculated for a grafting density of 16 DNA molecules per particle with long sticky end for pairs A-B (a), A-A (b, top panel), and B-B (b, bottom panel). The data from simple binning at a single temperature shown by empty symbols, and solid lines are estimates from the weighted histogram analysis method. Symbol and line colors are used to distinguish between various temperatures as labeled in panel a.

mentary ssDNA with a long sticky end, are shown in Fig. 5.2a. The free energy as a function of pair distance shows a distinct minimum at low temperatures, which corresponds to the bound configuration between particles A and B (stabilized by DNA hybridization). Specifically, the general shape of the pair potential and its dependence on temperature resemble the experimentally measured effective pair potentials [113]. For two particle simulations in a large enough box (approaching zero density limit), the minimum in free energy is an important parameter to characterize interactions between particles as a function of system parameters such as temperature, DNA grafting density, and length of sticky or spacer end [28].

Figure 5.3 shows the minimum interaction free energy as a function of temperature, which we find to vary in a highly non-linear manner. Previously, Dreyfus *et al.* [28] also predicted a similar non-linear dependence of the minimum interaction free energy on temperature with the help of a theoretical model. In their model, the minimum interaction free energy depends on the number of bonds formed between the two particles as well as the entropy associated with the selection of various combinations of strands or bonds on the two particles; the sharp decrease in the minimum interaction free energy as a function of decreasing temperature is most likely due to enhanced hydrogen bonding (due to the increase in the number of hydrogen bonds as the temperature decreases and the increased stability of a hydrogen bond with decreasing temperature), which is further facilitated by shorter distances at which the minimum occurs. However, in their model DNA is simplified as a rigid rod with a sticky point at the end (to represent complementary ssDNA), and the two particles are approximated as flat plates. In our model, ssDNA strands are relatively flexible, and the length of the sticky end is comparable to the length of the spacer. Given these differences between our simulation model and the theoretical model of Dreyfus *et al.*, the non-linear dependence of the minimum interaction free energy on temperature is expected to be a general feature of DNA-mediated particle interactions.

At low temperatures, the minimum interaction free energy can be quite significant compared to the thermal energy, thereby leading to irreversible particle binding. Appearance of such irreversible particle binding at temperatures not too far from the desired temperature range (weak binding regime) due to non-linearity is likely to be an inherent hindrance to particle rearrangement, and, therefore, crystallization in DNA-mediated particle assembly.
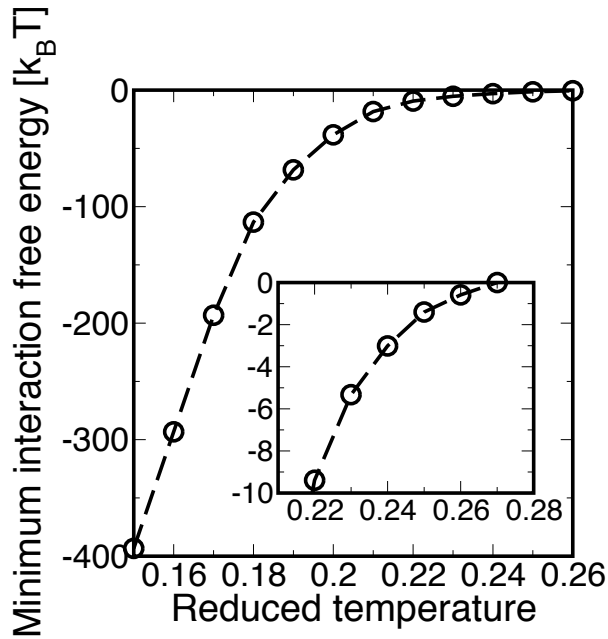
Figure 5.3: The minimum interaction free energy is shown as a function of temperature corresponding to system parameters used in Fig. 5.2a. The inset shows a zoomed-in view of the main plot.

5.3.2 Effect of DNA grafting density

In experiments, DNA grafting density on the particle surface can be controlled by synthesis methods [27, 101] as well as by adding non-hybridizing ssDNA in the solution buffer [29]. By controlling the fraction of sticky ends that can hybridize with complementary ssDNA on other particles, it was shown that the particle dissociation behavior (melting temperature and sharpness) can be controlled quanti-

tatively [19, 29]. It is still less well understood how this particular parameter can affect the pair interaction potential and the associated assembly mechanism. Here, we study the first question by calculating PMFs as a function of DNA grafting density ranging from 1 DNA molecule per particle to 32 DNA molecules per particle.

Figure 5.4 shows the minimum interaction free energy as a function of temperature for varying DNA grafting densities for the case of a short sticky end. For a given temperature, the minimum interaction free energy becomes lower with increasing DNA grafting densities as a greater number of complementary DNA molecules can hybridize between a pair of particles. According to Dreyfus et al. [28], the non-linear dependence of the minimum interaction free energy can be categorized into three different regimes. The weak-binding regime, in which the minimum interaction free energy is comparable to the thermal energy, is most relevant for successful DNA-mediated particle assembly in laboratory experiments. In this regime, the minimum interaction free energy is expected to be proportional to the average number of hydrogen bonds formed [28]. In Figure 5.4, we limit the range of the minimum interaction free energy from $-10k_BT$ to $-k_BT$, which approximately corresponds to the so-called weak-binding regime. We find that even in this regime, the variation in minimum interaction free energy as a function of temperature is quite non-linear. Similar behavior in the weak binding regime was also observed previously by Mirjam et al. [75].

To identify changes in pair PMF as a function of DNA grafting density, we use two special cases – constant temperature and constant minimum interaction free energy. Figure 5.5a shows PMFs between unlike particles (A-B) for different grafting densities, but the minimum interaction free energy is kept constant at $-4k_\mathrm{B}T$ by changing the temperature (see legend). We find that the change in temperature is related logarithmically to the DNA grafting density in order to obtain a constant minimum interaction free energy (data not shown). Though not entirely unexpected,
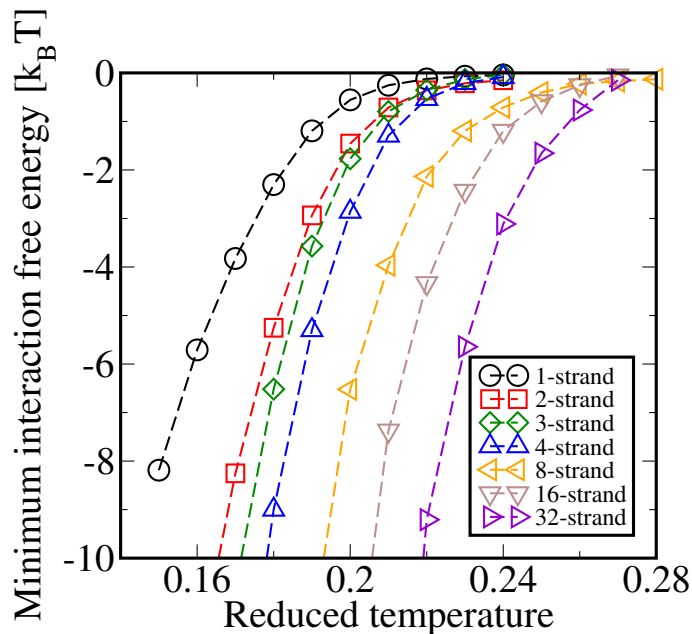
Figure 5.4: The minimum interaction free energy is shown as a function of temperature for different grafting densities (see legend) for the short sticky end.

the DNA grafting density significantly alters the shape of the pair interaction potential or PMF. The minimum in free energy is quite broad for lower grafting densities, but the attractive well becomes narrower with increasing DNA grafting density. This narrowing of the attractive well is most likely due to stronger repulsion caused by overlap between grafted DNA molecules at small pair distances. Although some previous work has been done relating shape of the pair potential with particle dynamics [130], there is no general framework to determine which of these potential shapes will be most desirable for ordered particle assembly. Our hypothesis is that intermediate DNA grafting densities will yield an optimum in the width of the attractive well so that pair distance can change as needed for structural rearrangements, while the resulting ordered structure is still stable without significant fluctuations in lattice parameters.

In Figure 5.5b, we compare PMFs at the same temperature for varying DNA grafting densities. The minimum interaction free energy decreases with increas-

ing DNA grafting density as expected due to the higher number of complementary strands that can hybridize. However, the maximum number of hydrogen bonds, defined as the number of hydrogen bonds formed between the two particles at the lowest temperature of our simulation, does not linearly increase with the number of grafted DNA chains (see Figure 5.6). This is most likely due to the excluded volume (repulsive) interactions between the DNA molecules on the same particle, thereby limiting the number of strands that can hybridize with increasing DNA grafting density. Similar to Figure 5.5a, we also observe narrowing of the attractive well in addition to deepening at higher DNA grafting densities, again due to enhanced repulsion between DNA molecules at small pair distances.

Finally, we note that the current model, due to its approximate nature, can only provide qualitative changes in the potential function, and therefore the observed changes in the potential width should be interpreted accordingly.

5.3.3 Effect of spacer length

Experimentally, Jin *et al.* [49] showed that an increase in the spacer length (the non-hybridizing part of the ssDNA) increases the melting temperature of DNA grafted on nanoparticles. Later, Sun *et al.* [137] also observed a similar increase in DNA melting temperature with increasing spacer length. From molecular simulations of the CG DFP model, Fernando *et al.* [141] found that longer spacer length can actually destabilize a preformed crystal lattice of DFPs at lower temperatures. Although there are several studies on the relationship between spacer length and DNA melting temperature, relatively little information is available on the dependence of the pair interaction potential between DFPs on spacer length.

Figure 5.7 shows PMFs between a pair of unlike DFPs (A-B) when each particle is grafted with 16 complementary ssDNA molecules with the long sticky end at the same temperature. The minimum interaction free energy decreases slightly
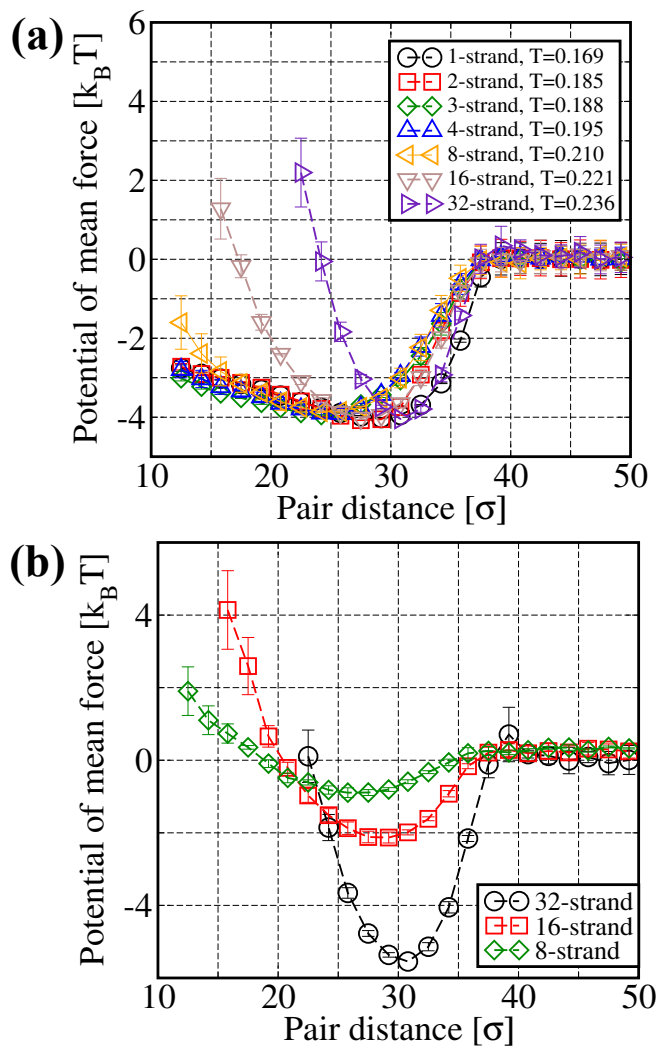
Figure 5.5: (a) Potential of mean force (PMF) for different DNA grafting densities for the short sticky end with the same attraction free energy of $-4k_BT$. (b) PMF for different grafting densities for the short sticky end at the same temperature of 0.23.
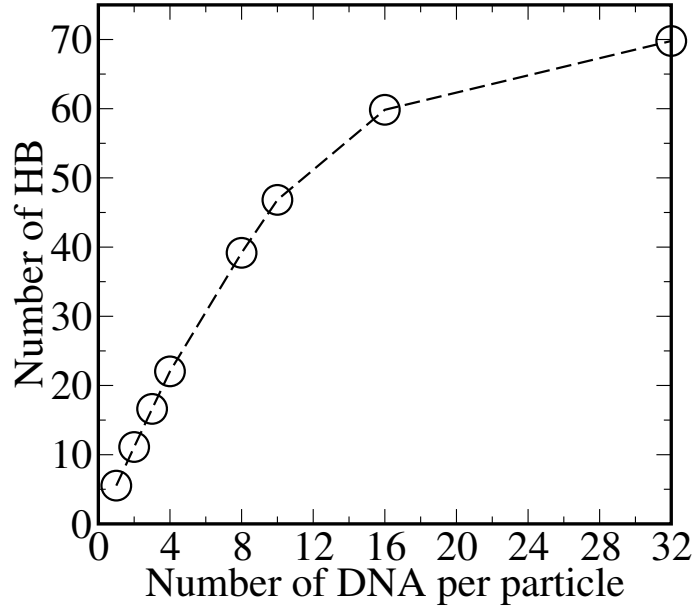
Figure 5.6: The average number of hydrogen bonds (HB) formed are shown as a function of DNA grafting density at the lowest temperature in our REMD simulation for the short sticky end (7 bases).

(by about 1 $k_{\mathrm{B}}T$) with increasing spacer lengths from 0 to 8 bases. This suggests that increasing the spacer length may help in the formation of more hydrogen bonds between DFPs, but other parameters such as DNA grafting density and particle curvature may be more important determinants of enhanced hydrogen bond formation. More importantly, the pair distance at which the minimum in the PMF occurs shifts to a higher value with increasing spacer length. These results are consistent with experimental observations, as the decrease in the minimum interaction free energy will lead to a higher melting temperature and the increase in preferred pair distance will lead to a longer translational lattice parameter [85]. As the width of the PMF also increases with increasing spacer length, one may expect destabilization of certain crystal lattices as observed by Fernando *et al.* [141] in their simulations.
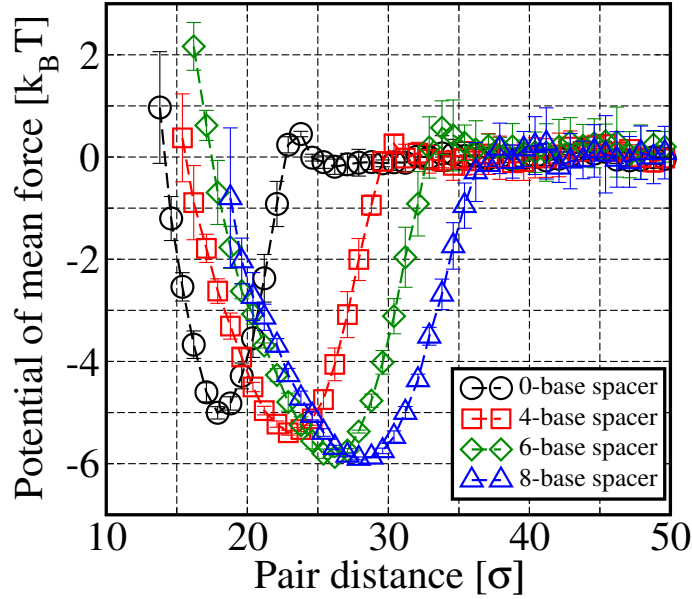
Figure 5.7: Effect of spacer length on the potential of mean force for long sticky end with 16 DNA molecules per particle at temperature 0.224.

5.3.4 Effect of sticky end length

In addition to varying the DNA grafting density, one can also alter the minimum interaction free energy between DFPs by changing the number of complementary base pairs (or type of base pairs formed, A:T versus G:C [126]) of the sticky end. Crocker *et al.* [89] found that reducing the sticky end length leads to a decrease in melting temperature. Similar conclusions were also drawn by others using separate linker-mediated interactions between DFPs [38]. Figure 5.8 compares PMFs obtained for a pair of DFPs with short and long sticky ends for three temperatures. Both of the DNA sequences (long and short sticky ends) have a total of 18 bases, out of which 7 and 12 are part of the sticky end for short and long sticky ends, respectively. Intuitively, varying the length of the sticky end (while keeping the total DNA length constant) can have two effects on the shape of the PMF – change in the depth and change in the width of the attractive potential well. As shown in Fig. 5.8, the minimum interaction free energy for the short sticky end is higher than for the long

sticky end at the same temperature, as expected. The minimum in free energy for the short sticky end is also shifted to longer pair distances due to shorter overlap between shorter sticky ends as compared to long sticky ends. Interestingly, the PMF well in the case of the short sticky end is wider as compared to that of the long sticky end. Current CG DFP models, which assume a point-like sticky end, cannot capture the effect of sticky end length on the shape of the PMF. This is not expected to be limiting for small variations in sticky end length but may be important for large changes in the sticky end length to model associated changes in the particle assembly behavior.
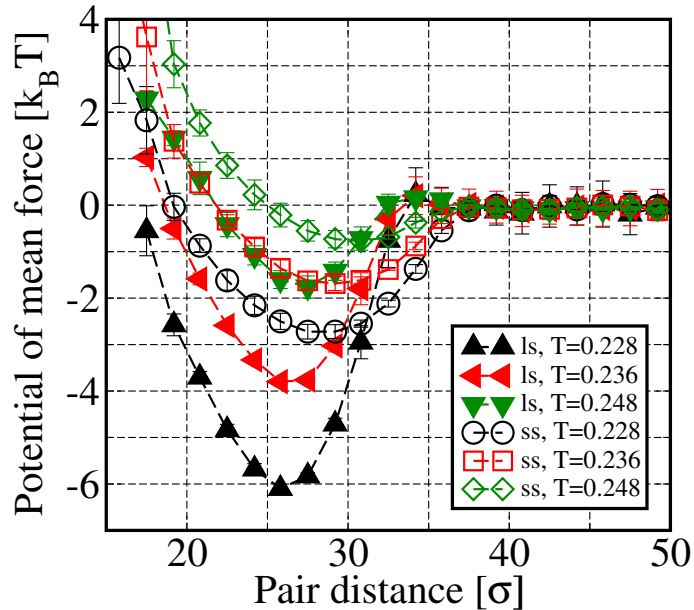
Figure 5.8: Comparison of potential of mean force between short and long sticky ends at three different temperatures. ss: short sticky end; ls: long sticky end.

5.4 Conclusions

In this chapter, we use the coarse-grained DNA model as described in section 4.2 to study the behavior of DNA-functionalized particles. The coarse-grained DNA model used here provides explicit DNA representation (at the nucleotide level) and comple-

mentary interactions between Watson-Crick base pairs, which lead to the formation of ssDNA hairpins and dsDNA. Aggregation between multiple complementary strands is prevented. We use this model to calculate the dependence of the free energy on the distance between a pair of DNA-coated particles as a function of temperature, DNA grafting density, and lengths of sticky end and spacer DNA. The change in the minimum interaction free energy as a function of system temperature is found to be non-linear even in the weak-binding regime. Our results of particle pair potentials as a function of system parameters can also be useful for future design of crystal lattices based on DNA-mediated particle assembly. For example, Macfarlane *et al.* [85], suggests that the lattice spacing can be adjusted by varying the hydrodynamic size ratio between two types of particles grafted with complementary DNA molecules. Based on our effective pair potentials, one should be able to modify the lattice spacing with the same hydrodynamic particle size ratio by varying the sticky end length while keeping the total DNA length the same. Moreover, we find that several system parameters (such as DNA grafting density and sticky end length) can be used to change the width of the attractive well. We hypothesize that shallower and broader attractive potentials may be preferable for particle assembly in ordered structures due to dynamic DNA hybridization [77], but may also lead to lower lattice stability. In the future, we plan to address these questions with multiparticle assembly simulations using the new coarse-grained model.

Chapter 6

Self-assembly of DNA-functionalzied particles

6.1 Introduction

Colloidal crystals have shown promise for their potential applications in photonic band-gap materials, sensors, catalytic supports and scaffold structures [55, 133]. Due to the advantages of direct visualization, they also serve as model systems to study the phase behaviour and crystallization kinetics of atomic and molecular crystals. Depending on the number of particle types, particle size ratio and particle interactions, a variety of colloidal crystal structures can be formed [36]. Due to the entropic driving force, hard spheres are known to be crystallized into limited types of close-packed crystals: the face-centered cubic (fcc) or hexagonal close-packed (hcp) [152]. For binary systems, more types of crystal structures can be obtained. Relying on the size ratio, the binary mixing of hard spheres can lead to three types of crystal structures: AB, AB_2 and AB_{13} [66]. The incorporation of attractive interactions can lead to additional crystal structures such as body-centered cubic (bcc), fcc and other exotic crystals. For example, CsCl, LS_6 and LS_8, and NaCl are reported for

oppositely charged ionic colloidal particles [71].

With the demand of achieving more complex crystals (e.g. diamond crystals) and abilities to program the formation of crystals, the DNA-functionalized particles (DFP) have been proposed [3, 90], in which the attractive interactions between particles are induced by the hybridization of complementary DNA sequences. The use of grafted, single-stranded DNA with engineered sequences can effectively tune the interactions between particles [72, 74, 113]. Albeit the versatility of this technology, the successes in obtaining desired crystals relies greatly on the some external factors such as operating conditions [19, 108, 123]. The interplay between thermodynamic and kinetic factors further complicates polymorph selection in the DNA-mediated interaction systems [123]. Most current studies are focus on 3D systems, while with its simplicity and advantage of visualization, 2D system should be a better system to study the self-assembly via DNA-functionalized particles.

In the previous chapter, we establish a new model system that consists of two nano-sized spheres, A and B, which are grafted with strands of ssDNA molecules, whose sequences are designed to be complementary to each other. Our previous computational study measures the potential of mean force between these two DNA-functionalized spheres and its dependence of various parameters in a systematic manner. We note that the interactions between two like particles, A-A or B-B, are purely repulsive and those between two unlike particles, A-B, are attractive. The repulsive interactions between two like particle have very weak temperature-dependence, while the attractive interactions between two unlike particle exhibit a strong temperature-dependence trend. In this chapter we first fit those potential of mean force via modified continuous Jagla (MCJ) potential function and study the crystallization and polymorphism of crystal phases of DNA-functionalized particles in 2D with MCJ potentials.

6.2   Fitting of pair potential

In the previous chapter, we use a detailed model, which includes the explicit representation of the grafted DNA strands, to find the effective pair potentials between DNA-functionalized particles. Here we extend our study to the crystallization of the binary system in 2D using the computed effective pair potentials. Now each DNA-functionalized particle is coarse-grained into a single spherical bead interacting via an effective pair potential due to the grafted DNA chains. By considering the intrinsic physics of the bridging between two DFPs, we fit the potential of mean force between two DFPs with a modified continuous Jagla (MCJ) potential, which has three terms to represent the contribution from (1) sphere-sphere repulsion due to volume exclusion, (2) repulsion due to compression of the grafted DNA chains and (3) attraction due to DNA hybridization respectively as follows:

$$U(r) = \epsilon \left(\frac{\sigma}{r}\right)^n + \frac{A_0}{1 + \exp(A_1 r - A_2)} + \frac{B_0}{1 + \exp(B_1 r - B_2)} \tag{6.1}$$

Figure 6.1(Left) shows one example of comparison between the original data and the fitted MCJ potential. The original data (black circles) is the potential of mean force between two DFPs with each particle grafted by 16, 12-mer long sticky end, DNA strands at temperature T=0.228. In order to improve the fitting quality, we also apply umbrella sampling to obtain additional data point at short contact distances (red circles). Although not based on formal statistical mechanics argument, the fitted MCJ potential exhibits a very good representation of the original data for a wide range of temperatures (Figure 6.1(Right)) and grafting density (data not shown).

We use the MCJ potential to fit a large amount of PMF data from the previous chapter. We have the following conclusive points for a specific grafting scheme: (1) Sphere-sphere repulsion, which can be modeled as 36th power repulsive potential, is temperature independent as expected; (2) Polymer-type repulsions between over-
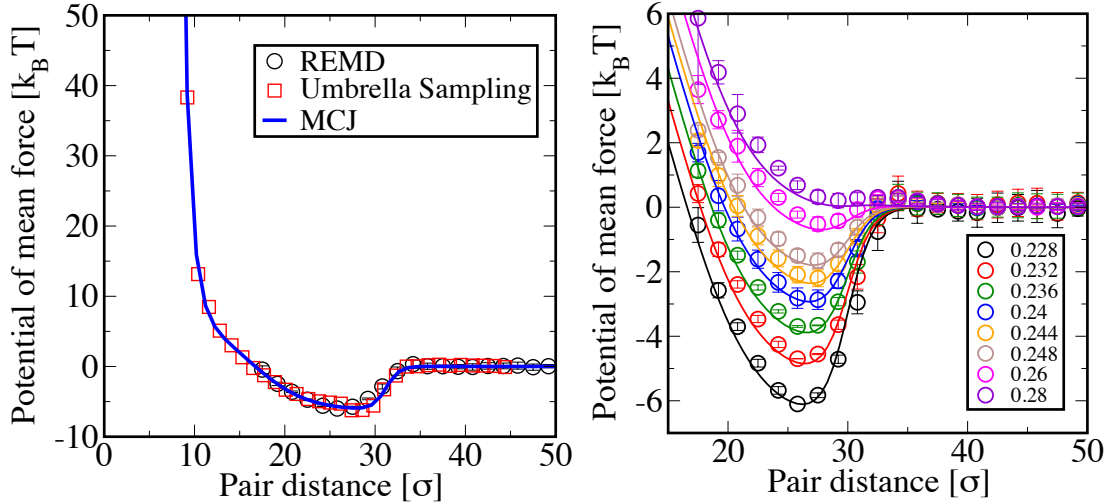
Figure 6.1: (Left) Fitting of potential of mean force (PMF) between two DNA-functionalized particles with each particle grafted by 16, 12-mer long sticky end, DNA strands at T=0.228. (Right) Fitting of PMFs as described in the left panel but for different temperatures.

lapped DNA chains are also temperature independent; (3) Attractive interactions due to DNA hybridization are temperature dependent; (4) Only single parameter B_0 is needed to capture the temperature dependence of attractive interactions. Therefore all the parameters related to the sphere-sphere repulsion are only dependent on particle size; all the parameters relevant to polymer-type repulsion is only dependent on the grafting scheme, i.e. number of grafted DNA chains and length and sequences of DNA strands; all the parameters for the attractive portion of interaction except B_0 are dependence on grafting scheme. Only by varying B_0, we can obtain pair interactions at all the temperatures if the particle size and grafting scheme are fixed.

6.3 Binary lattice analysis

Possible crystal lattices comprised of equal size of A and B particles interacting with self-similar and isotropic potentials in 2D are either square lattice or hexagonal (hex) lattice. Based on the principle of maximizing the number of nearest neighbors to

which it can form DNA connections, four types of lattice are identified as shown in Figure 6.2 varying by the number of nearest neighbors. For the 4-fold coordinated square lattice, each particle is surrounded by 4 unlike nearest neighbors; i.e. each A (green) particle connects to 4 (silver) B particles and vice versa (Figure 6.2(a)). For the 6-fold coordinated hex lattice, each particle is surrounded by 6 nearest neighbors. We can assign each nearest neighbor as either like or unlike particles. Therefore possible combinations of nearest neighbors are: (0A, 6B), (1A, 5B), (2A, 4B) and (3A, 3B), if we assume the center particle is type A. The case of (0A, 6B) leads to honeycomb lattice as shown in Figure 6.2(c); (2A, 4B) forms the type of hex lattice exhibited in Figure 6.2(b), which we call alternating-string (A-S) lattice; (3A, 3B) corresponds to the honeycomb lattice of Figure 6.2(d), which is similar to Figure 6.2(c) by only switching the green and silver color. We also note that for the (1A, 5B) case, no crystal lattice can be formed by replicating the unit cell.

We define $N_{AB} = \sum_i n^i_{AB}/2n$ as an order parameter that describes the average number of A-B bonds formed for each particle in the lattice, where n is total number of particles in the lattice and n^i_{AB} is the total number of A-B bonds between particle i and its nearest neighbors. The summation is over all the particles in the lattice and the factor of 2 is used to account for the double counting of bonds. We find that all the four crystal lattices in Figure 6.2 achieved the same N_{AB} value of 2. Therefore if we only consider attractive interactions between nearest-neighbor unlike particle, i.e. $E_{AB} > 0, E_{AA} = E_{BB} = 0$ where E_{AB}, E_{AA} and E_{BB} are the depth of relevant attractions, all the four crystal lattice are energetically degenerate. Served as an lower bound, we also compute this order parameter for completely random square lattice and hex lattice with A:B stoichiometry of 1:1 by simple probability argument. We find N_{AB} is 1 for square lattice and 1.5 for hex lattice.

Following the definition of N_{AB}, we can also define $N_{AA} = \sum_i n^i_{AA}/2n$ and $N_{BB} = \sum_i n^i_{BB}/2n$ to characterize the average number of A-A and B-B bonds be-

73
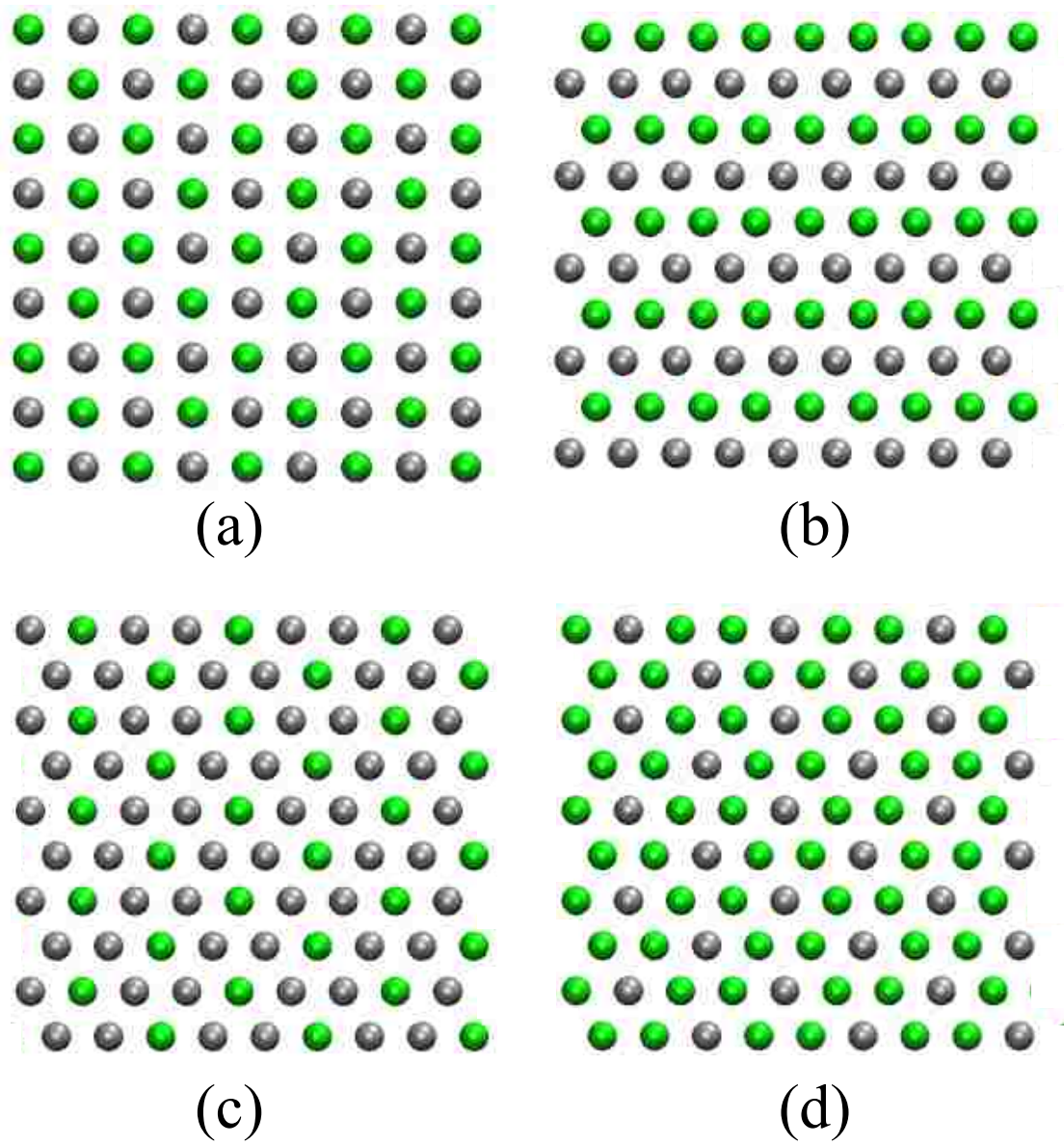
Figure 6.2: Possible crystal lattices comprised of equal size of A and B particles in 2D by considering maximizing nearest-neighbor unlike bonds.

tween each particle and its nearest neighbors in the lattice. We find that for square lattice (Figure 6.2(a)) $N_{AA} = N_{BB} = 0$; $N_{AA} = 2/3$ and $N_{BB} = 1/3$ for A-S hex lattice (Figure 6.2(b)); the value of N_{AA} and N_{BB} equals to 0 and 1 for honeycomb (Figure 6.2(c)); $N_{AA} = 1$ and $N_{BB} = 0$ for honeycomb (Figure 6.2(d)). Although the value of N_{AB} is same for all the four crystal lattices, the values of N_{AA} and N_{BB} are different among these lattices, which change the relative stability of these crystal phases if one can tune the interactions between each particle and its like nearest neighbors.

6.4 Lattice energies calculations

The results presented in the previous section suggest that in 2D both square lattice and hexagonal lattice are theoretically possible due to energetical degeneration with respect to the nearest neighbor binding energy, which is assumed to be dominant because of short-ranged nature of DNA-mediated interactions. Next, we apply the effective pair interactions derived from coarse-grained DFPs model to compute lattice energies which is free energy at ground state for each of the four crystal lattices shown in Figure 6.2. If we just include the attractive interaction between each particle and its unlike-nearest neighbors, the lattice energies curves are same for the four possible lattice phases (Figure 6.3), which is consistent with previous N_{AB}-based predictions. However if we turn on the repulsive interactions between each particle and its like-nearest neighbors, we can see in Figure 6.3, square crystal lattice has lower lattice energies comparing with hex lattice, which indicates the square crystals as the stable crystal phase at the ground state. The relative stability of the square lattice arises from the fact that the extra like bonds (see section previous section), which stem from overlap of the non-hybridizing DNA chains from nearest-neighbor like particles, increase the lattice energy of the hex lattices. We note the lattice energies are same

for the two different hex lattices because the total number of like bonds is same for these two lattices.
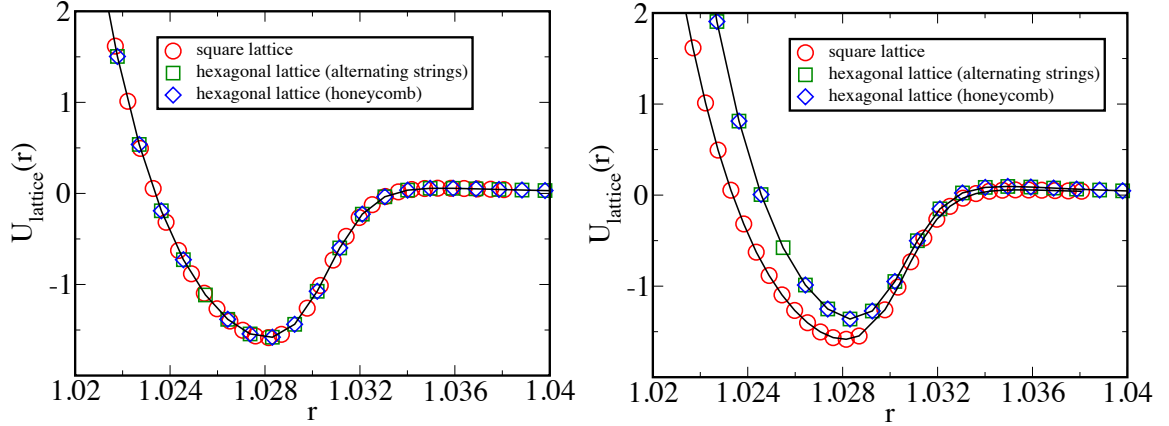
Figure 6.3: (Left) Lattice energies calculations for square and hexagonal lattices by including attraction between unlike particles, E_{AB}. (Right) Lattice energies calculations for square and hexagonal lattices by including attraction between unlike particles, E_{AB}, and repulsion between like particles.

Due to the specificity and versality of DNA-mediated interactions, we can also make the interactions between like particles attractive by mixing different DNA sequences in single particle species. The detail strategies of how to induce attractive interactions between like particles will be discussed in the later of this chapter. Now we assume $E_{AB} > E_{AA} = E_{BB} > 0$. We compute the lattice energies for different values of E_{AA} (or E_{BB}) and data are shown in Figure 6.4. By increasing of E_{AA} (or E_{BB}), the lattice energies of hex lattices decrease and at some point the lattice energies of hex lattice are smaller than those of square lattice, which indicate hex lattice is a stable crystal phase. We note that lattice energies of square crystal lattice are independent on the value of E_{AA} and E_{BB} since all the like particles do not belong to the nearest neighbors in square lattices. We also note that the lattice energies of two hex lattice, honeycomb and alternating strings, are same under the condition $E_{AA} = E_{BB}$ because the total number of like bonds are identical for the two case. On the other side, because honeycomb has 2/3 more A-A bonds and 2/3 less B-B bonds

than alternating-string structure, under the condition $E_{AA} < E_{BB}$ or $E_{AA} > E_{BB}$, honeycomb can be stabilized.
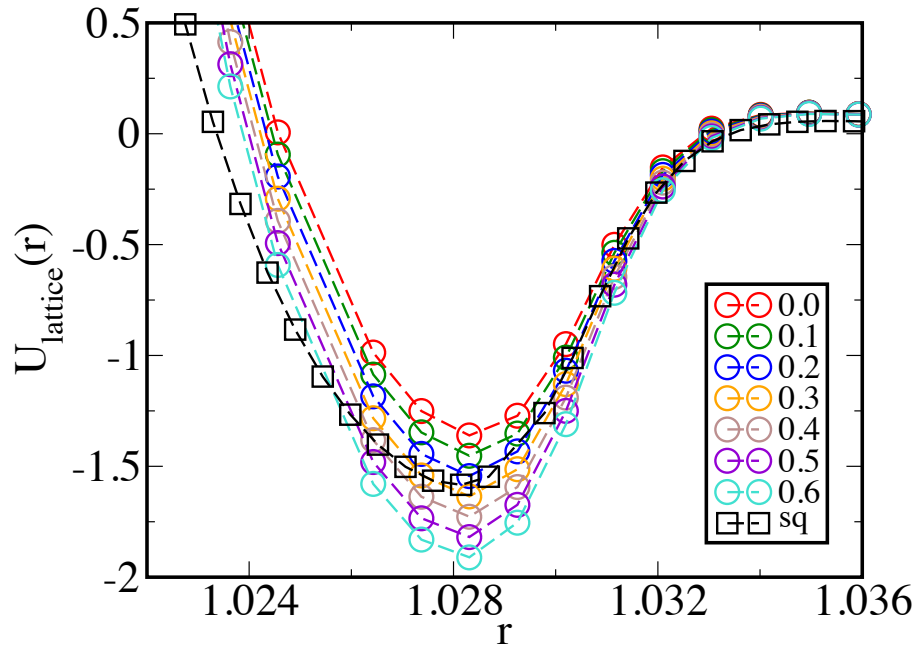
Figure 6.4: Lattice energies calculations for square and hexagonal lattices by increasing the attractions between like particles, $E_{AA} = E_{BB} > 0$

To conclude, from lattice energies calculations, we predict square crystal lattice is the stable phase when the interactions between like particles are repulsive. By adding attractive interactions between like particles, hex crystal lattice becomes more stable. By differentiating the attractions of different types of like particles, honeycomb crystal lattice can be stabilized. The lattice-energy based predictions only consider the ground states. The presence of finite temperature and entropy effect complicates the polymorph selection. In the next section we will apply direct molecular dynamics simulations to determine the physical plausibility of these predictions and related defects due to kinetics.

6.5 Molecular dynamics simulation of crystallization of binary mixtures in 2D

In this section, we apply direct molecular dynamics simulations to study the crystallization of the 2D binary system, in which particles interact through coarse-grained DNA-mediated interactions. These simulations are helpful to establish whether it would be possible to achieve different crystal phases by tuning the relative binding strength between different particle species. We perform MD simulations with various binding energy combinations at the packing fraction of 10%. We initialized simulations with total 400 particles with equal numbers of A and B particles in a random initial state.

We first develop a pseudo-crystal phase diagram for lattice ordering in Figure 6.5 at the condition of $E_{AA} = E_{BB} \leq E_{AB}$. Overall, this pseudo-phase diagram is found to exhibit structures that are in excellent agreement with the lattice energies predictions. For the relatively small value of E_{AA} or E_{BB}, the crystal are all found to be highly ordered square lattices. Further increasing the value of E_{AA} or E_{BB}, we obtain hex lattices. From snapshots of the MD simulations. We find square lattices exhibit almost perfect compositional ordering while hex lattices show a significant disorder in composition. We quantify the lattice ordering by computing $2N_{AB}$ for each point in the phase diagram of Figure 6.5. As mentioned in section 6.3, the order parameter $2N_{AB}$ has maximum value of 4 for both perfect square and hex lattices and minimum value of 2 for completely random square lattices and 3 for completely random hex lattices. From Figure 6.5, we find square lattices always exhibit very high ordering, while the ordering of hex lattices decay by increasing E_{AA} or E_{BB}. The hex lattices become completely random as $E_{AB} = E_{AA,BB}$.

In addition, at the condition $E_{AA,BB} \approx 0.3 - 0.4$, we observe a transformation between the square and alternating-string hex lattices. Our observations indicate
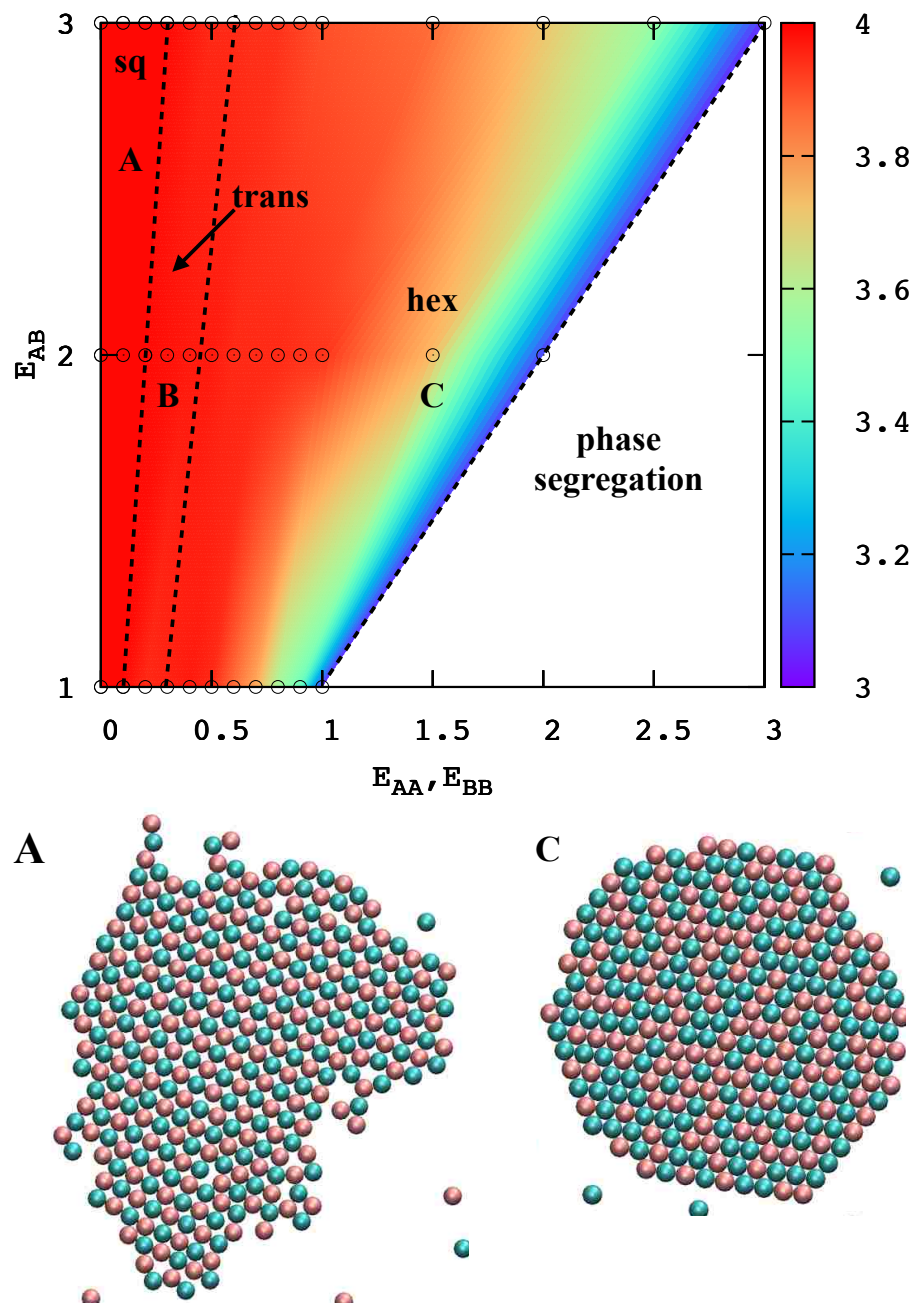
Figure 6.5: Phase diagram for binary crystals under the condition of $E_{AA} = E_{BB} \leq E_{AB}$. Three phases that nucleate and grow from fluid are identified: square lattice (sq), hexagonal lattice (hex) and a transformation region (trans), in which initially nucleated square lattices undergo a rapid transformation into hexagonal lattices before continuing to grow further. The order parameter N_{AB} is computed to quantify the ordering of square and hexagonal lattice. Representative crystal lattice configurations at the three regions of the phase diagram are also shown in this figure (A and C) and Figure 6.6 (B).

B

growth
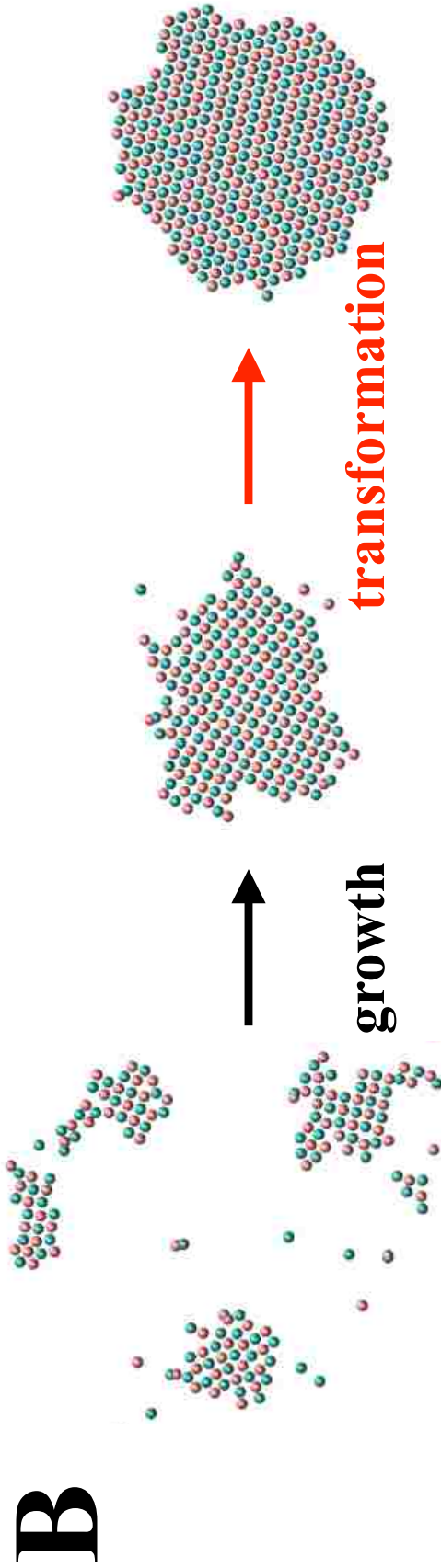
transformation

Figure 6.6: Representative snapshots from MD simulation trajectories at the transformation region (B) of the phase diagram in Figure 6.5

that the small crystal nuclei in the system initially display the morphology of square lattices, but transfer to alternating-string hex lattices once the square lattice grow further as shown in Figure 6.6. The plausible explanation would be due to the kinetic limitations with respect to the compositional ordering during initial nucleation stage as also observed for other systems [19]. Therefore, the system initially choose square lattices because the ground state, ordered hex lattices, is kinetically inaccessible, although ordered hex lattice state has lower free energy.

The fact that hex lattice crystals are subject to a significant compositional disorder under equilibrium conditions is related to both thermodynamic and kinetic issues for hex lattices. Firstly, we discuss the kinetic issues. We consider only the scenario of the antisite, which is defined as a single compositional ordering defect in a binary lattice, as its importance for crystal growth. The energy penalty for a single antisite on the edge of a binary lattice is dependent on the numbers and types of nearest neighbors for that antisite. We tabulate the possible combinations of the numbers and types of nearest neighbors and the corresponding probabilities of occurrence (Appendix A). The expected value of energy penalty is $2E_{AB}$ for a single antisite on the edge of a perfect binary square lattice and Δ_{AB} (or $E_{AB} - E_{AA,BB}$) for a single antisite on the edge of alternating-string hex lattice. Because the expected energy penalty of an antisite on a square lattice is substantially larger than that on a alternating-string hex lattice, square lattices tend to more ordered in terms of compositions. Secondly, from the thermodynamic side, honeycomb and alternating-string lattices are energetically degenerate at the ground state since both have equal average number of like and unlike bonds under the condition of $E_{AA} = E_{BB}$. Therefore the obtained the hex lattice is composed of mixture of these two hex lattice. It is difficult to obtain perfect alternating-string hex lattices from the growth of hex nucleates under $E_{AA} = E_{BB}$, while the most ordered alternating-string hex lattices are obtained from transformations.

We also develop a pseudo-crystal phase diagram in Figure 6.7 at the condition of $E_{AA} \leq E_{BB}$ and $E_{AB} = 1.0$, where we expect to obtain honeycomb lattices (Figure 6.2c) according to the lattice energies predictions. From the snapshot of MD simulations, we find the honeycomb lattices have less defects for the relatively small value of E_{AA}. Therefore, we quantify the ordering of honeycomb lattice by computing $2(N_{BB} - N_{AA})$ and $r_{B/A}$, which is defined as the number ratio of B and A particles in the formed crystal lattices. $r_{B/A} = 2.0$ for perfect honeycomb lattices and $r_{B/A} = 1.0$ for completely random hex lattices at the mixing ratio of 1:1. $2(N_{BB} - N_{AA}) = 2.0$ for perfect honeycomb lattices. For completely random hex lattices, $2(N_{BB} - N_{AA}) = 0$ at the mixing ratio of 1:1. Both $2(N_{BB} - N_{AA})$ and $r_{B/A}$ can deviate from their perfect honeycomb value upward or downward dependent on the type of defects formed in the crystal lattices. As shown in Figure 6.7, the increase of E_{AA} always leads to the lower ordering while the dependence of ordering on E_{BB} is relatively weak. In order to explain this observation, we compute the expected energy penalty for honeycomb lattices (Appendix A), which is equal to $E_{AB} - E_{AA}$ or Δ'_{AB}. This result confirms the strong relation between the defects and magnitude of E_{AA} and the validity of our single-antisite-based crystal growth model.

To conclude, we identify three different crystal lattices by direct MD simulations, which is consistent with lattice energies predictions. When there are only repulsions between like particles, ordered square lattices are obtained. The adding of attractive interactions between like particles stabilizes the hexagonal lattices. The most ordered alternating-string hex lattices always come from square lattice transformations, while the most ordered honeycomb lattices are grown from hexagonal nucleates at the condition of no attractions between particle species that locates at the center of hexagonal cells.
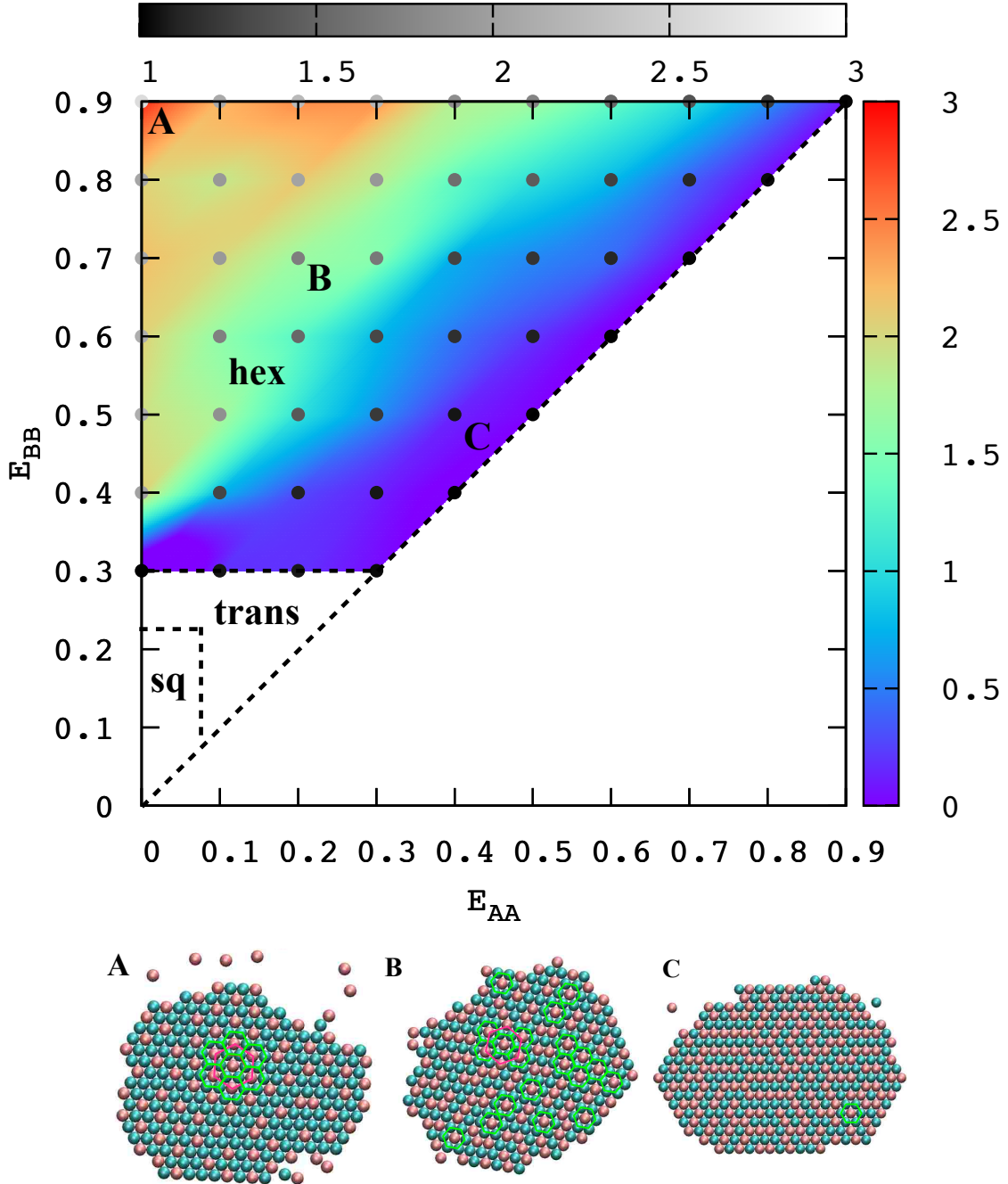
Figure 6.7: Phase diagram for binary crystals under the condition of $E_{AA} \leq E_{BB}$ and $E_{AB} = 1.0$, at which honeycomb crystal lattice is predicted as the stable phase. Three phases that nucleate and grow from fluid are identified: square lattice (sq), hexagonal lattice (hex) and a transformation region (trans), in which initially nucleated square lattices undergo a rapid transformation into hexagonal lattices before continuing to grow further. Two order parameters are computed for hexagonal phase, $N_{BB} - N_{AA}$ (color) and $r_{B/A}$ (gray), to quantify the ordering of honeycomb-type hexagonal structure. Snapshots from MD simulations at three points (A, B, C) of the phase diagram show different compositional ordering.

6.6 Design of DNA-functioinalized particles

In order to induce attraction between a particle and others of its own kind, the particle have to contain DNA strands that can hybridize to other strands on its own surface. The possible approach is to attach mixtures of different DNA sequences to each particle species. For example, particles A species can be functionalized with a mixture of two complementary sequences of α and β. If we assume each particle A is to a good approximation grafted with an equal number of DNA molecules, a mixing ratio $w_{\alpha/\beta} = 0.4$ means 40% of the grafted DNA strands are sequence α and the remaining 60% are sequence β. Such mixing strategy basically introduce the attraction between a particle and others of its own kind due to the hybridization between complementary sequences, i.e. α and β sequences, from two different particles of the same species. By varying the mixing ratio of different particle species, one can simply control the relative strength of attraction of different particles species, i.e. A-A and B-B. We note the above mixing scheme is not limited to the mixture of two different DNA sequences. By following the similar mixing scheme, one in essence can specify a matrix of binding strengths between numbers of different particle species by mixing variety of different DNA sequences in different particle species.

We now consider two different interactions: (1) mixed interactions where each particle contains mutually complementary DNA sequences and (2) unmixed interactions where each particle contains non-complementary DNA sequences but two different particle species contain complementary sequences. We compute the potential of mean forces for the two cases by using our detailed CG model for DNA-functionalized particle. Figure 6.8 shows two representative sets of measured pair-interaction potentials between two mixed and unmixed (i.e. A and B are fully complementary), DFPs as a function of temperature with total 16, 7-mer short sticky end, DNA strands grafted on particle surfaces. As is observed for unmixed case, pair potentials

for mixed case show a temperature-dependent attraction that decreases monotonically with increasing temperature and the same temperature-independent repulsion. Comparing to unmixed case at the same temperature, we notice that the strength of interactions are weakened by $\sim 50\%$ for mixed case.
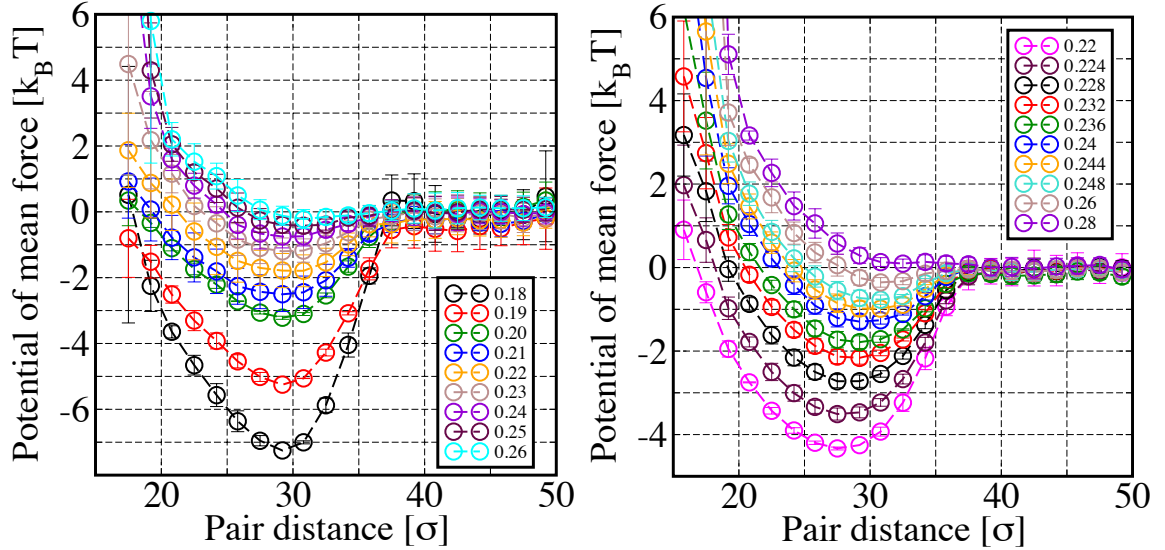
Figure 6.8: Two representative sets of measured pair-interaction potentials between two mixed (left) and unmixed (right), DNA-functionalized particles as a function of temperature. Total 16, 7-mer short sticky end, DNA strands are grafted on the surface of each particle.

A simple thermodynamic argument can be derived as follows to explain the $\sim 50\%$ reduction of attractive interaction strength. Let the hybridzation free energy between two complementary DNA sequences denoted as E_{hyb}. The binding probability of pair of complementary DNA strands (i.e. α and β) from two particles (i.e. A and B) for the unmixed case can be expressed as:

$$P_{\text{bind}} = \exp(-E_{\text{hyb}})P_\alpha^A P_\beta^B, \tag{6.2}$$

where P_α^A is the probability that the binding strand from particle A is α-DNA, which is equivalent to the concentration of α-DNA on particle A. The similar definition can be applied to P_β^B. For the unmixed case, $P_\alpha^A = P_\beta^B = 1$. For the mixed case,

addtional term is needed to account for the binary mixing:

$$P_{\text{bind}} = \exp(-E_{\text{hyb}})(P_\alpha^A P_\beta^B + P_\beta^A P_\alpha^B). \tag{6.3}$$

Therefore for the mixing ratio $w_{\alpha/\beta} = 0.5$, $P_\alpha^A = P_\beta^A = P_\alpha^B = P_\beta^B = 0.5$. The attractive interaction strength is propotional to average number of hybridized DNA strands:

$$E_{\text{att}} \sim \min(N_{\text{DNA}}^A, N_{\text{DNA}}^B)P_{\text{bind}}, \tag{6.4}$$

where N_{DNA}^i is the number of accessible DNA strands on particle species i. By simple calculations, we know that $E_{\text{att}}^{\text{mixed}}/E_{\text{att}}^{\text{unmixed}} = 0.5$, if we assume $N_{\text{DNA}}^A = N_{\text{DNA}}^B$, which confirms our CG simulation data. We note the 50% reduction can only be served as a lower bound. In reality due to intraparticle self binding which competes with interparticle bridging, the reduction would be much higher.

Now we consider mixing strategies to achieve ordered honeycomb lattices. The problem can be described as follows: we have two different particle species (i.e. A and B) and two DNA sequences who have complementary sticky ends (i.e. α and β). Particle species A has a strands of α-DNA and b strands of β-DNA. Particle species B has c strands of α-DNA and d strands of β-DNA. We can assume A is the α-DNA rich species and B is the β-DNA rich species without loss of generality. We require $E_{AB} > E_{BB} > E_{AA}$, which means the attractive interactions between A species and B species are greater than that between B species and itself and the attractive interactions between B species and itself are greater than that between A species and itself. We need to achieve the above goal by proper mixing two different sequences in each particle species.

This problem can be reformulated as nonlinear optimization problem. If we denote the hybridization free energy of α and β sequences as E_{hyb}, we can express the E_{AB}, E_{BB} and E_{AA} as:

$$E_{AB} = \min(N_{\text{DNA}}^A, N_{\text{DNA}}^B) \exp(-E_{\text{hyb}}) \left[\left(\frac{a}{a+b} \right) \left(\frac{d}{c+d} \right) + \left(\frac{b}{a+b} \right) \left(\frac{c}{c+d} \right) \right].$$

$$E_{AA} = 2\min(N_{\text{DNA}}^A, N_{\text{DNA}}^B) \exp(-E_{\text{hyb}}) \left[\left(\frac{a}{a+b} \right) \left(\frac{b}{a+b} \right) \right].$$

$$E_{BB} = 2\min(N_{\text{DNA}}^A, N_{\text{DNA}}^B) \exp(-E_{\text{hyb}}) \left[\left(\frac{c}{c+d} \right) \left(\frac{d}{c+d} \right) \right].$$

For convenient, we assume $a + b = c + d$: the total number of DNA strands in each particle, no matter A species or B species, are roughly same. Therefore N_{DNA}^A and N_{DNA}^B are also same. The scale of a, b, c, d with respect to $a+b$ (or $c+d$) now can be replaced by a, b, c, d, which represent the percentage of α- and β-DNA on Particle A and B respectively. The mathematical formulation of this problem is shown as:

$$
\begin{aligned}
& \underset{a,b,c,d}{\text{minimize}} && ab - cd \\
& \text{subject to} && ad + bc \geq 2cd + \gamma, \\
& && cd \geq ab, \\
& && a \geq b, \\
& && d \geq c, \\
& && a, b, c, d \leq 1, \\
& && a, b, c, d \geq 0, \\
& && a + b = 1, \\
& && c + d = 1,
\end{aligned}
$$

where, γ is an input variable that controls differences between E_{AB} and E_{BB}. According to constraints, $0 \leq \gamma \leq 1$ should be satisfied. The above constraint nonlinear optimization problem has optimal solution and can be solved by routine method such as interior point method. If we assume total number of DNA strands on particle A and B species are same and $\gamma = 0.22$, the optimal solution are $[a, b, c, d] = [1, 0, 1/3, 2/3]$,

which means we only functionalize particle A species with α-DNA and we functionalize particle B species with 1/3 α-DNA and 2/3 β-DNA. The attraction strength between A-B, B-B and A-A are $E_{AB}/E_{BB} = 3/2$ and $E_{AA} = 0$. Finally we note the assumption of equal number of grafting density is just for illustration and is not necessary. The above optimization formulation can be extended to the nonequal grafting density cases.

6.7 Conclusions

In this chapter, we report a comprehensive computational analysis of the self assembly of ordered 2D binary crystal lattices, in which the interactions are governed by DNA bridging between particles. The attractive interactions between like particles i.e. E_{AA} and E_{BB}, are required to stabilize the hexagonal lattices over square lattices. At the same time, a large difference in the binding energies, i.e. between E_{AB} and E_{BB} or E_{AA}, is required to reduce the equilibrium concentration of defects. As a result, highly constrained conditions were required in order to achieve good ordering in the hexagonal lattices. In addition, the binding and rolling kinetics of DFPs, which are still poorly understood, are likely to be much more slower than our CG pair-interaction type simulations. Therefore in reality it may be more challenging to obtain well-ordered hexagonal lattices. On the other hand, without the complication of E_{AA} and E_{BB}, it is more easily to grow perfect square lattices. We also observe the mixing ratio has no strong influences on the ordering of crystal lattices. However due to the slow kinetics, the mixing ratio can play an important role in determining the final structures as observed from our experimental studies (not published). The interplay between kinetic and thermodynamic factors that observed in this study is also present in more complex systems, i.e. ones with more components and different particle sizes. The methods we apply in this study can be extended to explore more

complex phase diagrams.

Chapter 7

Future work and preliminary results

7.1 Simulation of colloidal suspension with hydrodynamic interactions

7.1.1 Hydrodynamics

The dynamic behavior of colloidal particles in a viscous fluid is strongly influenced by hydrodynamic forces arising from the relative motion of colloidal particles and the fluid. Hydrodynamic interactions are extremely important in accurately simulating such kind of systems due to their long-range and multi-body nature, which can only be neglected at very dilute concentration. The Reynolds number indicates the importance of inertia relative to viscous forces. For colloidal suspension, the Reynolds number depends on the particle size and the relative velocity between the particle and the fluid, which are generally very small. Therefore viscous forces dominate the effects of inertia and inertia is negligible for the flows on the scale of colloidal particles. When the Reynolds number is small, the flow is governed by the Stokes

equations. Because of the linearity of Stokes equations, the hydrodynamic forces on the particle are proportional to the relative velocity between the particle and the fluid. If the velocity for the particles are specified and the force is unknown, this is the *resistance* problem [54]. If the force is specified, one needs to seek the velocity of the particle. This is known as the *mobility* problem [54]. There are many approaches to solve the Stokes equations for spheres moving in the Newtonian fluid. One approach is to use the so-called *fundamental* solutions or *Stokeslet* which is the solutions of Stokes equations under a point force. The velocity field in creeping flow then can be expressed in terms of a surface distribution of point forces:

$$\mathbf{u}(\mathbf{x}) - \mathbf{u}^\infty(\mathbf{x}) = -\frac{1}{8\pi\mu} \int_{S_y} \mathbf{G}(\mathbf{x} - \mathbf{y}) \cdot \mathbf{S}(\mathbf{y}) dS_y \tag{7.1}$$

where $\mathbf{u}^\infty(\mathbf{x})$ is the velocity field in the absence of the particles, S_y is the surface of the particle, $\mathbf{S}(\mathbf{y})$ is the surface stresses and $\mathbf{G}$ is the Oseen tensor of the form:

$$\mathbf{G}(\mathbf{x}) = \frac{\mathbf{I}}{x} + \frac{\mathbf{xx}}{x^3} \tag{7.2}$$

Rather than solving the integral equation, we can use multipole expansion to obtain the velocity field:

$$G_{ij}(x - y) = \sum_{n=0}^{\infty} \frac{(-1)^n}{n!} (y_{k_1} - \alpha_{k_1})(y_{k_2} - \alpha_{k_2}) \cdots (y_{k_n} - \alpha_{k_n}) \left(\frac{\partial^n G_{ij}(x - y)}{\partial y_{k_1} \partial y_{k_2} \cdots \partial y_{k_n}} \right)_{y=\alpha} \tag{7.3}$$

, where i, j and ks are coordinate indices. The integer n is the order of the multipole expansion. If we truncate the multipole expansion, then the integral representation can be written as:

$$u_i(\mathbf{x}) - u_i^\infty(\mathbf{x}) = -\frac{1}{8\pi\mu} G_{ij} F_j + \frac{1}{8\pi\mu} G_{ij,k} D_{jk} \tag{7.4}$$

, where the first term is the monopole contribution and the second term is the dipole contribution. The monopole contribution is due to a point force,

$$F_j = - \int_{S_y} f_j dS_y. \tag{7.5}$$

The dipole is due to the force dipole,

$$D_{jk} = \int_{S_y} f_j(y_k - \alpha_k) dS_y. \tag{7.6}$$

The force dipole can be represented as the sum of symmetric and antisymmetric parts,

$$D_{jk} - \frac{1}{3} D_{ii} \delta jk = S_{jk} + T_{jk} \tag{7.7}$$

The symmetric part S_{jk} is also called as *stresslet* which result in the straining motion at a point, and the antisymmetric part T_{jk} is also named as *rolet* which result in a point torque.

$$S_{jk} = \frac{1}{2} \int_{S_y} (f_j(y_k - \alpha_k) + f_k(y_j - \alpha_j)) dS_y - \frac{1}{3} \int_{S_y} f_i(y_i - \alpha_i) \delta_{jk} dS_y \tag{7.8}$$

and

$$T_{jk} = \frac{1}{2} \int_{S_y} (f_j(y_k - \alpha_k) - f_k(y_j - \alpha_j)) dS_y \tag{7.9}$$

The exact solutions of force, torque and stresslet on a single sphere can be derived by the Faxén Laws [54]. In low Reynolds number regime, hydrodynamics interactions among dense particle suspensions are completely characterized by either the resistance or the mobility matrix. The resistance matrix gives the forces in terms of the velocities and the mobility matrix gives the velocities in terms of forces.

7.1.2 Stokesian dynamics

Stokesian dynamics is a molecular-dynamics type approach for simulating the dynamic behavior of many particles suspended in a fluid [16]. Being different from the Brownian dynamics, which oversimplifies the hydrodynamic interactions by using Oseen tensor and therefore is generally valid only in dilute suspensions, Stokesian dynamics incorporate many-body hydrodynamic interactions, which is valid even for dense suspensions. The dynamics of particles in a suspension is governed by N-body Langevin equation:

$$\mathbf{m} \cdot \frac{\partial \mathbf{U}}{\partial t} = \mathbf{F}^H + \mathbf{F}^B + \mathbf{F}^P \tag{7.10}$$

This equation states that total forces equals mass times acceleration. The total forces can be separated into the hydrodynamic force $\mathbf{F}^H$, interparticle force $\mathbf{F}^P$ and Brownian forces $\mathbf{F}^B$. The linearity of Stokes equation requires the force/torque and stresslet exerted by the fluid on the particles, and the particles velocities and the rate of strain are related in the form of:

$$\begin{pmatrix} \mathbf{F} \\ \mathbf{S} \end{pmatrix} = -R \cdot \begin{pmatrix} \mathbf{U} - \mathbf{U}^\infty \\ -\mathbf{E}^\infty \end{pmatrix}, \tag{7.11}$$

and

$$R = \begin{pmatrix} R_{FU} & R_{FE} \\ R_{SU} & R_{SE} \end{pmatrix} \tag{7.12}$$

where R_{FU}, R_{FE}, R_{SU} and R_{SE} are the resistance matrices and R is called grand resistance matrix. The evolution equation is obtained by integrating the N-body

Langevin equation two times over a time step Δt:

$$\Delta \mathbf{x} = Pe\{\mathbf{U}^\infty + R_{FU}^{-1} \cdot [R_{FE} : \mathbf{E}^\infty + \dot{\gamma}^{-1}\mathbf{F}^P]\Delta t + \nabla \cdot R_{FU}^{-1}\Delta t + \mathbf{X}(\Delta t) \qquad (7.13)$$

where $\Delta\mathbf{x}$ is the change of particle position during the time step Δt, $\mathbf{X}(\Delta t)$ is a random displacement due to Brownian motion. In order to make use of the evolution equation, we must determine the grand resistance matrix R. A method that incorporates the near-field lubrication effects and the dominant many-body interactions has been developed [16]. The mobility matrix M, which is the inverse of the grand resistance matrix, can be approximated by combining Faxén's law for particle velocities with a truncated multipole moments representation of the particles. The approximated grand mobility matrix M^∞ can be inverted to yield a far-field approximation to the grand resistance matrix. This many-body approximation to the resistance matrix does not account to the lubrication effects, which can only be reproduced by inverting of the grand mobility matrix if all multipole moments are included. In order to incorporate the lubrication effects, a pairwise-additive two-body resistance matrix is added:

$$R = (M^\infty)^{-1} + R_{lub} \qquad (7.14)$$

7.1.3   Fast lubrication dynamics

According to Kumar et al. [64], the grand resistance matrix R can be expressed as a sum of a diagonal isotropic resistance tensor R_0 and a pairwise interaction tensor R_δ coming from the asymptotic approximation for the lubrication contribution R_{lub} as

$$R = R_0 + R_\delta \qquad (7.15)$$

. The pairwise interaction tensor R_δ, can be obtained based on the pair-drag model by Ball and Melrose [6], which throws out all long-range and multibody hydrodynamic interactions and simplifies the hydrodynamics to pairwise interactions with suitable cutoffs. The isotropic resistance tensor R_0 consists of three different scalars: R_{FU}^0, $R_{T\Omega}^0$, and R_{SE}^0, respectively denoting force-velocity, torque-angular velocity, and stresslet-rate of strain coupling as follows:

$$
R_0 = \begin{pmatrix} R_{FU}^0 I & 0 & 0 \\ 0 & R_{T\Omega}^0 I & 0 \\ 0 & 0 & R_{SE}^0 I \end{pmatrix}.
\tag{7.16}
$$

The value of R_{FU}^0, $R_{T\Omega}^0$, and R_{SE}^0 were chosen to match the short-time translational and rotational self-diffusivity obtained from Stokesian dynamics simulation.

7.1.4 Equilibrium transport coefficients of quasi-hard sphere particle suspension by fast lubrication dynamics

We first presents the data of the effects of volume fraction on the long-time self diffusivity. Figure 7.1 shows the long-time diffusivity at equilibrium as a function of ϕ with hydrodynamic interaction by fast lubrication dynamics. Particles are modeled by inverse power potential, $U(r) = \epsilon(\sigma/r)^{36}$, which approximates the hard sphere particles. Also shown in the figure are previous simulation results of hard spheres by Stokesian dynamics [33].

The zero-shear viscosity from the Green-Kubo formula by Foss and Brady [34], is compared with data from steady-shear simulation by fast lubrication dynamics as a function of volume fraction, in Figure 7.2. The values calculated by fast lubrication dynamics from steady-state averages at the lowest shear rate ($Pe = 0.01$ and 0.005)
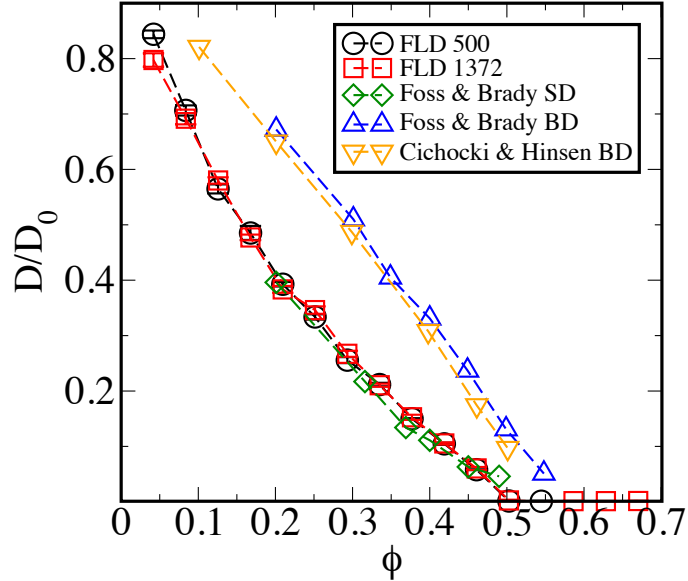
Figure 7.1: Equilibrium values of the long-time self-diffusivity as a function of ϕ. Data include those from both the Brownian Dynamics [25, 33] and Stokesian Dynamics [33] simulation results. $D_0 = k_B T / 6\pi\eta a$

are virtually indistinguishable from the previously reported viscosities determined from Green-Kubo analysis.

7.1.5 Rheological properties of quasi-hard sphere particle suspension by fast lubrication dynamics

In Figure 7.3, we compare the viscosities simulated from fast lubrication dynamics and Stokesian dynamics. In fast lubrication dynamics, particles are modeled by inverse power potential, $U(r) = \epsilon(\sigma/r)^{36}$, which approximates the hard sphere particles. The viscosities from fast lubrication dynamics and Stokesian dynamics are in good quantitative agreement and both exhibit shear-thinning behavior at low shear rate and shear-thickening behavior at high shear rate for dense suspensions.
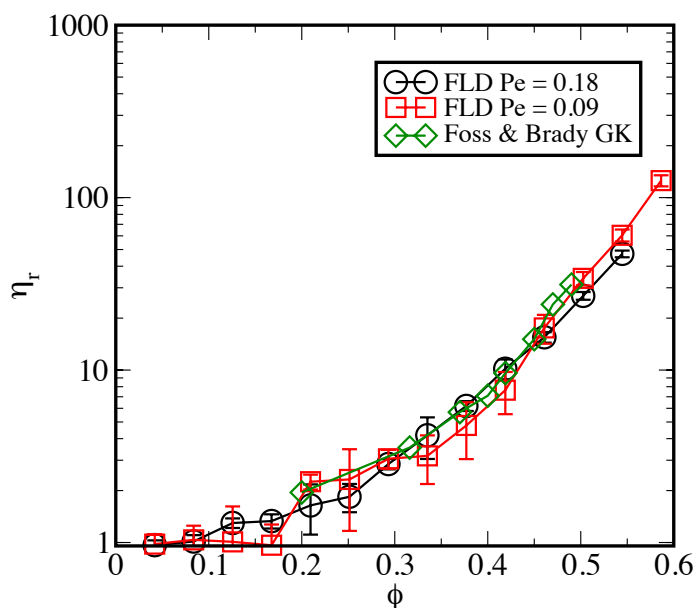
Figure 7.2: Zero-shear limiting relative viscosity, η_r, as a function of volume fraction from fast lubrication dynamics. Simulation results include both previously measured values determined from an equilibrium Green-Kubo analysis by Boss and Brady [34].
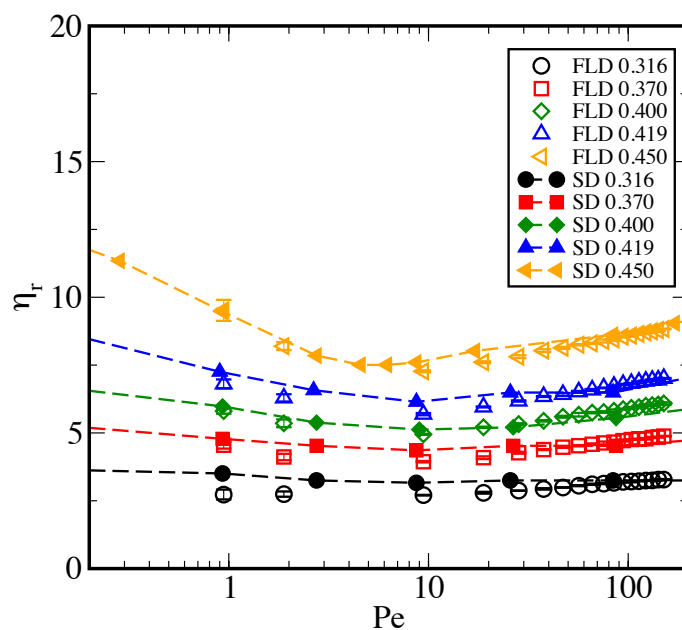
Figure 7.3: Comparison of the relative viscosity of quasi-hard sphere suspensions determined by fast lubrication dynamics as a function of Péclet number Pe with hard-sphere suspensions determined by Stokesian dynamics [34].

7.2 Effect of shear force on self-assembly of DNA-functionalized particles

It is well known that shear has a large effect on colloidal self-assembly. Shear-induced crystallization is the result of flow-induced rearrangements in the microstructure of the fluid, caused by an interplay between hydrodynamics interactions, Brownian motion and interparticle forces. Besseling et al. [9] characterized the real-space structure of four oscillatory shear-induced phases in hard-sphere fluids: the twinned fcc phase, the sliding layer phase, the string phase and the tilted layer phase, via Brownian Dynamics simulations and experiments on PMMA colloids (Figure 7.4). The structures obtained from simulations (with imposed linear velocity profile and no hydrodynamic interactions) are in strong agreement with the experiments. Their results suggested that deviations from a linear profile can be neglected for small Pe number and except for large Pe numbers, hydrodynamic interactions do not strongly affect the shear-induced structures

The crystallization of DNA-functionalized particles is still quite challenging due to the interplay of thermodynamic and kinetic factors. In the future, we plan to use nonequilibrium molecular dynamics (NEMD) to study the shear-induced crystallization for binary particle suspensions with coarse-grained pair interactions in both 2D and 3D. We want to answer the questions such as how the shear forces alter the equilibrium crystal phase diagrams and whether shear forces can facilitate the annealing of crystal structures.
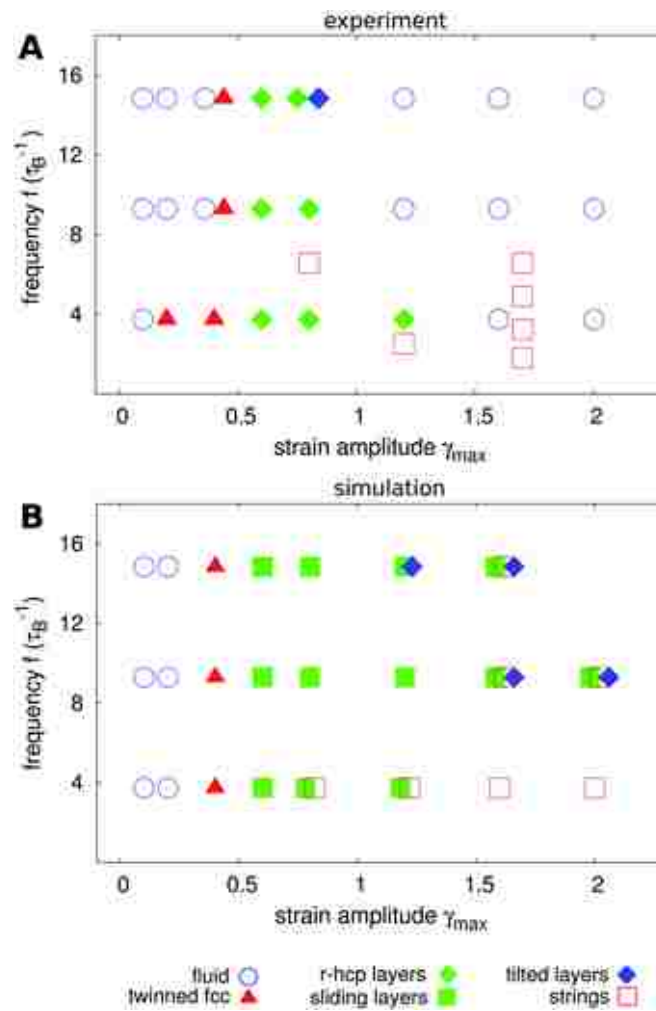
Figure 7.4: The out-of-equilibrium phase diagrams of hard-sphere like particles [9]. (A) Experimental results. (B) Simulation results by Brownian Dynamics.

Bibliography

[1] Constructing polyhedra from repelling points on a sphere. http://www.chiark.greenend.org.uk/ sgtatham/polyhedra/. Accessed: 2014-04-09.

[2] R. Agrawal and D. A. Kofke. Thermodynamic and structural properties of model systems at solid-fluid coexistence. *Mol. Phys.*, 85(1):23–42, 1995.

[3] A. P. Alivisatos, K. P. Johnsson, X. peng, T. E. Wilson, C. J. Loweth, M. P. Bruchez JR, and P. G. Schultz. Organization of 'nanocrystal molecules' using dna. *Nature*, 382(6592):609–611, 1996.

[4] H. C. Andersen, J. D. Weeks, and D. Chandler. Relationship between the hard-sphere fluid and fluids with realistic repulsive forces. *Phys. Rev. A*, 4:1597–1607, 1971.

[5] S. Angioletti-Uberti, B. M. Mognetti, and D. Frenkel. Re-entrant melting as a design principle for dna-coated colloids. *Nat Mater*, 11(6):518–522, 06 2012.

[6] R. Ball and J. Melrose. A simulation technique for many spheres in quasi-static motion under frame-invariant pair drag and brownian forces. *Physica A: Statistical Mechanics and its Applications*, 247:444 – 472, 1997.

[7] A. Baranyai and D. Evans. Direct entropy calculation from computer simulation of liquids. *Phys. Rev. A*, 40:3817–3822, 1989.

[8] D. Ben-Amotz and G. Stell. Hard sphere perturbation theory for fluids with soft-repulsive-core potentials. *J. Chem. Phys.*, 120(10):4844–4851, 2004.

[9] T. H. Besseling, M. Hermes, A. Fortini, M. Dijkstra, A. Imhof, and A. van Blaaderen. Oscillatory shear-induced 3d crystalline order in colloidal hard-sphere fluids. *Soft Matter*, 8:6931–6939, 2012.

[10] R. B. Best and J. Mittal. Protein simulations with an optimized water model: Cooperative helix formation and temperature-induced unfolded state collapse. *J. Phys. Chem. B*, 114(46):14916–14923, 2010.

[11] P. L. Biancaniello, J. C. Crocker, D. A. Hammer, and V. T. Milam. Dna-mediated phase behavior of microsphere suspensions. *Langmuir*, 23(5):2688–2693, 2007.

[12] P. L. Biancaniello, A. J. Kim, and J. C. Crocker. Colloidal interactions and self-assembly using DNA hybridization. *Phys. Rev. Lett.*, 94:058302, 2005.

[13] G. Bossis, J. F. Brady, and C. Mathis. Shear-induced structure in colloidal suspensions: I. numerical simulation. *J. Colloid Interface Sci.*, 126(1):1–15, 1988.

[14] M. J. Boyer, Y. Ding, and J. Mittal. in preparation.

[15] J. F. Brady and G. Bossis. The rheology of concentrated suspensions of spheres in simple shear flow by numerical simulation. *J. Fluid Mech.*, 155:105–129, 1985.

[16] J. F. Brady and G. Bossis. Stokesian dynamics. *Annual Review of Fluid Mechanics*, 20(1):111–157, 1988.

[17] A. C. Branka and D. M. Heyes. Thermodynamic properties of inverse power fluids. *Phys. Rev. E*, 74(3):031202, 2006.

[18] G. Bryant, S. Williams, L. Qian, I. Snook, E. Perez, and F. Pincet. How hard is a colloidal "hard-sphere" interaction? *Phys. Rev. E*, 66:060501, 2002.

[19] M. T. Casey, R. T. Scarlett, W. B. Rogers, I. Jenkins, T. Sinno, and J. C. Crocker. Driving diffusionless transformations in colloidal crystals using DNA handshaking. *Nat. Commun.*, 3:1209, 2012.

[20] D. Chandler, J. D. Weeks, and H. C. Andersen. Van der waals picture of liquids, solids, and phase transformations. *Science*, 220(4599):787–794, 1983.

[21] D. T. N. Chen, Q. Wen, P. A. Janmey, J. C. Crocker, and A. G. Yodh. Rheology of soft materials. *Annu. Rev. Condens. Matter Phys.*, 1(1):301–322, 2010.

[22] X. Cheng, J. H. McCoy, J. N. Israelachvili, and I. Cohen. Imaging the microscopic structure of shear thinning and thickening colloidal suspensions. *Science*, 333(6047):1276–1279, 2011.

[23] X. Cheng, X. Xu, S. A. Rice, A. R. Dinner, and I. Cohen. Assembly of vorticity-aligned hard-sphere colloidal strings in a simple shear flow. *Proc. Natl. Acad. Sci.*, 109(1):63–67, 2012.

[24] A. Chremos and A. Z. Panagiotopoulos. Structural transitions of solvent-free oligomer-grafted nanoparticles. *Phys. Rev. Lett.*, 107:105503, 2011.

[25] B. Cichocki and K. Hinsen. Dynamic computer simulation of concentrated hard sphere suspensions: I. simulation technique and mean square displacement data. *Physica A: Statistical Mechanics and its Applications*, 166(3):473 – 491, 1990.

[26] W. Dai, C. W. Hsu, F. Sciortino, and F. W. Starr. Valency dependence of polymorphism and polyamorphism in DNA-functionalized nanoparticles. *Langmuir*, 26(5):3601–3608, 2010.

[27] L. M. Demers, C. A. Mirkin, R. C. Mucic, R. A. Reynolds, R. L. Letsinger, R. Elghanian, and G. Viswanadham. A fluorescence-based method for determining the surface coverage and hybridization efficiency of thiol-capped oligonucleotides bound to gold thin films and nanoparticles. *Analytical Chemistry*, 72(22):5535–5541, 2000.

[28] R. Dreyfus, M. E. Leunissen, R. Sha, A. Tkachenko, N. C. Seeman, D. J. Pine, and P. M. Chaikin. Aggregation-disaggregation transition of dna-coated colloids: Experiments and theory. *Phys. Rev. E*, 81:041404, 2010.

[29] R. Dreyfus, M. E. Leunissen, R. Sha, A. V. Tkachenko, N. C. Seeman, D. J. Pine, and P. M. Chaikin. Simple quantitative model for the reversible association of DNA coated colloids. *Phys. Rev. Lett.*, 102:048301, 2009.

[30] M. Dzugutov. A universal scaling law for atomic diffusion in condensed matter. *Nature*, 381(6578):137–139, 1996.

[31] J. R. Errington and P. G. Debenedetti. Relationship between structural order and the anomalies of liquid water. *Nature*, 409(6818):318–321, 2001.

[32] J. R. Errington, T. M. Truskett, and J. Mittal. Excess-entropy-based anomalies for a waterlike fluid. *J. Chem. Phys.*, 125(24):244502, 2006.

[33] D. R. Foss and J. F. Brady. Self-diffusion in sheared suspensions by dynamic simulation. *J. Fluid Mech.*, 401:243–274, 1999.

[34] D. R. Foss and J. F. Brady. Structure, diffusion and rheology of brownian suspensions by stokesian dynamics simulation. *J. Fluid Mech.*, 407:167–200, 2000.

[35] C. Gao, S. Kulkarni, J. Morris, and J. Gilchrist. Direct investigation

of anisotropic suspension structure in pressure-driven flow. *Phys. Rev. E*, 81:041403, 2010.

[36] U. Gasser. Crystallization in three- and two-dimensional colloidal suspensions. *J. Phys.: Condes. Matter*, 21:203101, 2009.

[37] N. Geerts and E. Eiser. Dna-functionalized colloids: Physical properties and applications. *Soft Matter*, 6:4647–4660, 2010.

[38] N. C. Harris and C.-H. Kiang. Disorder in dna-linked gold nanoparticle assemblies. *Phys. Rev. Lett.*, 95:046101, Jul 2005.

[39] D. Heyes and A. Branka. The influence of potential softness on the transport coefficients of simple fluids. *J. Chem. Phys.*, 122(23):234504, 2005.

[40] D. M. Heyes and A. C. Branka. Physical properties of soft repulsive particle fluids. *Phys. Chem. Chem. Phys.*, 9(41):5570–5575, 2007.

[41] D. M. Heyes and A. C. Branka. Self-diffusion coefficients and shear viscosity of inverse power fluids: from hard- to soft-spheres. *Phys. Chem. Chem. Phys.*, 10(27):4036–4044, 2008.

[42] D. M. Heyes and A. C. Branka. Transport coefficients of soft repulsive particle fluids. *J. Phys.-Condes. Matter*, 20(11), 2008.

[43] D. M. Heyes and A. C. Branka. Density and pressure dependence of the equation of state and transport coefficients of soft-sphere fluids. *Mol. Phys.*, 107:309–319, 2009.

[44] J. Hoyt, M. Asta, and B. Sadigh. Test of the universal scaling law for the diffusion coefficient in liquid metals. *Phys. Rev. Lett.*, 85:594–597, 2000.

[45] C. W. Hsu, M. Fyta, G. Lakatos, S. Melchionna, and E. Kaxiras. Ab initio determination of coarse-grained interactions in double-stranded dna. *J. Chem. Phys.*, 137(10):105102–105102–12, 2012.

[46] C. W. Hsu, J. Largo, F. Sciortino, and F. W. Starr. Hierarchies of networked phases induced by multiple liquid–liquid critical points. *Proc. Natl. Acad. Sci. U.S.A.*, 105(37):13711–13715, 2008.

[47] C. W. Hsu, F. Sciortino, and F. W. Starr. Theoretical description of a dna-linked nanoparticle self-assembly. *Phys. Rev. Lett.*, 105:055502, 2010.

[48] J. N. Israelachvili. *Intermolecular and Surface Forces (Third Edition)*. Academic Press, 2011.

[49] R. Jin, G. Wu, Z. Li, C. A. Mirkin, and G. C. Schatz. What controls the melting properties of dna-linked gold nanoparticle assemblies? *J. Am. Chem. Soc.*, 125(6):1643–1654, 2003.

[50] G. S. G. K. Kremer and M. O. Robbins. Dynamics of supercooled liquids interacting with a repulsive yukawa potential. *J. Phys. A: Math.Gen.*, 20(3):181–187, 1987.

[51] D. Kalman and N. Wagner. Microstructure of shear-thickening concentrated suspensions determined by flow-usans. *Rheol. Acta*, 48(8):897–908, 2009.

[52] M. Kenward and K. D. Dorfman. Brownian dynamics simulations of single-stranded dna hairpins. *J. Chem. Phys.*, 130(9):095101–095101–10, 2009.

[53] S. Khrapak and G. Morfill. Predicting freezing for some repulsive potentials. *Phys. Rev. Lett.*, 103:255003, 2009.

[54] S. Kim and S. J. Karrila. *Microhydrodynamics: Principles and Selected Applications*. Dover Publications, 2005.

[55] S.-H. Kim, S. Y. Lee, S.-M. Yang, and G.-R. Yi. Self-assembled colloidal structures for photonics. *NPG Asia Mater*, 3:25–33, 2011.

[56] Y. C. Kim and G. Hummer. Coarse-grained models for simulations of multiprotein complexes: Application to ubiquitin binding. *Journal of Molecular Biology*, 375(5):1416 – 1433, 2008.

[57] C. Knorowski, S. Burleigh, and A. Travesset. Dynamics and statics of dna-programmable nanoparticle self-assembly and crystallization. *Phys. Rev. Lett.*, 106:215501, 2011.

[58] C. Knorowski and A. Travesset. Dynamics of dna-programmable nanoparticle crystallization: gelation, nucleation and topological defects. *Soft Matter*, 8:12053–12059, 2012.

[59] T. A. Knotts IV, N. Rathore, D. C. Schwartz, and J. J. de Pablo. A coarse grain model for dna. *J. Chem. Phys.*, 126(8):084901–084901–12, 2007.

[60] N. Koumakis, A. Pamvouxoglou, A. S. Poulos, and G. Petekidis. Direct comparison of the rheology of model hard and soft particle glasses. *Soft Matter*, 8:4271–4284, 2012.

[61] W. P. Krekelberg, V. Ganesan, and T. M. Truskett. Shear-rate-dependent structural order and viscosity of a fluid with short-range attractions. *Phys. Rev. E*, 78:010201, 2008.

[62] W. P. Krekelberg, J. Mittal, V. Ganesan, and T. M. Truskett. Structural anomalies of fluids: Origins in second and higher coordination shells. *Phys. Rev. E*, 77:041201, 2008.

[63] K. Kremer and G. S. Grest. Dynamics of entangled linear polymer melts: a moleculardynamics simulation. *J. Chem. Phys.*, 92(8):5057–5086, 1990.

[64] A. Kumar and J. Higdon. Origins of the anomalous stress behavior in charged colloidal suspensions under shear. *Phys. Rev. E*, 82:051401, Nov 2010.

[65] S. Kumar, J. M. Rosenberg, D. Bouzida, R. H. Swendsen, and P. A. Kollman. The weighted histogram analysis method for free-energy calculations on biomolecules. i. the method. *Journal of Computational Chemistry*, 13(8):1011–1021, 1992.

[66] S.-C. Kung, C.-C. Chang, W. Fan, and M. A. Snyder. Template-free ordered mesoporous silicas by binary nanoparticle assembly. *Langmuir*, 30(39):11802–11811, 2014.

[67] E. Lange, J. B. Caballero, A. M. Puertas, and M. Fuchs. Comparison of structure and transport properties of concentrated hard and soft sphere fluids. *J. Chem. Phys.*, 130(17), 2009.

[68] J. Largo, P. Tartaglia, and F. Sciortino. Effective nonadditive pair potential for lock-and-key interacting particles: The role of the limited valence. *Phys. Rev. E*, 76:011402, 2007.

[69] O.-S. Lee and G. C. Schatz. Interaction between dnas on a gold surface. *J. Phys. Chem. C*, 113(36):15941–15947, 2009.

[70] O.-S. Lee and G. C. Schatz. Molecular dynamics simulation of dna-functionalized gold nanoparticles. *J. Phys. Chem. C*, 113(6):2316–2321, 2009.

[71] M. E. Leunissen, C. G. Christova, A.-P. Hynninen, C. P. Royall, A. I. Campbell, A. Imhof, M. Dijkstra, R. van Roij, and A. van Blaaderen. Ionic colloidal crystals of oppositely charged particles. *Nature*, 437(7056):235–240, 2005.

[72] M. E. Leunissen, R. Dreyfus, F. C. Cheong, D. G. Grier, R. Sha, N. C. Seeman,

and P. M. Chaikin. Switchable self-protected attractions in dna-functionalized colloids. *Nat. Mater.*, 8(7):590–595, 2009.

[73] M. E. Leunissen, R. Dreyfus, R. Sha, N. C. Seeman, and P. M. Chaikin. Quantitative study of the association thermodynamics and kinetics of dna-coated particles for different functionalization schemes. *J. Am. Chem. Soc.*, 132(6):1903–1913, 2010.

[74] M. E. Leunissen, R. Dreyfus, R. Sha, T. Wang, N. C. Seeman, D. J. Pine, and P. M. Chaikin. Towards self-replicating materials of dna-functionalized colloids. *Soft Matter*, 5:2422–2430, 2009.

[75] M. E. Leunissen and D. Frenkel. Numerical study of dna-functionalized microparticles and nanoparticles: Explicit pair potentials and their implications for phase behavior. *J. Chem. Phys.*, 134(8):084702–084702–18, 2011.

[76] T. I. N. G. Li, R. Sknepnek, R. J. Macfarlane, C. A. Mirkin, and M. Olvera de la Cruz. Modeling the crystallization of spherical nucleic acid nanoparticle conjugates with molecular dynamics simulations. *Nano Lett.*, 12(5):2509–2514, 2012.

[77] T. I. N. G. Li, R. Sknepnek, and M. Olvera de la Cruz. Thermally active hybridization drives the crystallization of dna-functionalized nanoparticles. *J. Am. Chem. Soc.*, 135(23):8535–8541, 2013.

[78] N. Y. C. Lin, X. Cheng, and I. Cohen. Biaxial shear of confined colloidal hard spheres: the structure and rheology of the vorticity-aligned string phase. *Soft Matter*, 10:1969–1976, 2014.

[79] N. Y. C. Lin, S. Goyal, X. Cheng, R. N. Zia, F. A. Escobedo, and I. Cohen. Far-

from-equilibrium sheared colloidal liquids: Disentangling relaxation, advection, and shear-induced diffusion. *Phys. Rev. E*, 88:062309, 2013.

[80] M. C. Linak and K. D. Dorfman. Analysis of a dna simulation model through hairpin melting experiments. *J. Chem. Phys.*, 133(12):–, 2010.

[81] M. C. Linak, R. Tourdot, and K. D. Dorfman. Moving beyond watson–crick models of coarse grained dna dynamics. *J. Chem. Phys.*, 135(20):–, 2011.

[82] M. C. Linak, R. Tourdot, and K. D. Dorfman. Moving beyond watson-crick models of coarse grained dna dynamics. *J. Chem. Phys.*, 135(20):205102–205102–12, 2011.

[83] P. J. Lu and D. A. Weitz. Colloidal particles: Crystals, glasses, and gels. *Annual Review of Condensed Matter Physics*, 4(1):217–233, 2013.

[84] X. Ma, W. Chen, Z. Wang, Y. Peng, Y. Han, and P. Tong. Test of the universal scaling law of diffusion in colloidal monolayers. *Phys. Rev. Lett.*, 110:078302, 2013.

[85] R. J. Macfarlane, B. Lee, M. R. Jones, N. Harris, G. C. Schatz, and C. A. Mirkin. Nanoparticle superlattice engineering with dna. *Science*, 334(6053):204–208, 2011.

[86] F. J. Martinez-Veracoechea, B. Bozorgui, and D. Frenkel. Anomalous phase behavior of liquid-vapor phase transition in binary mixtures of dna-coated particles. *Soft Matter*, 6:6136–6145, 2010.

[87] F. J. Martinez-Veracoechea, B. M. Mladek, A. V. Tkachenko, and D. Frenkel. Design rule for colloidal crystals of dna-functionalized particles. *Phys. Rev. Lett.*, 107(4), 2011.

[88] L. D. Michele and E. Eiser. Developments in understanding and controlling self assembly of dna-functionalized colloids. *Phys. Chem. Chem. Phys.*, 15:3115–3129, 2013.

[89] V. T. Milam, A. L. Hiddessen, J. C. Crocker, D. J. Graves, and D. A. Hammer. Dna-driven assembly of bidisperse, micron-sized colloids. *Langmuir*, 19(24):10317–10323, 2003.

[90] C. A. Mirkin, R. L. Letsinger, R. C. Mucic, and J. J. Storhoff. A dna-based method for rationally assembling nanoparticles into macroscopic materials. *Nature*, 382(6592):607–609, 1996.

[91] J. Mittal, J. R. Errington, and T. M. Truskett. Thermodynamics predicts how confinement modifies the dynamics of the equilibrium hard-sphere fluid. *Phys. Rev. Lett.*, 96:177804, 2006.

[92] J. Mittal, J. R. Errington, and T. M. Truskett. Relationships between self-diffusivity, packing fraction, and excess entropy in simple bulk and confined fluids. *J. Phys. Chem. B*, 111(34):10054–10063, 2007.

[93] J. Mittal, V. K. Shen, J. R. Errington, and T. M. Truskett. Confinement, entropy, and single-particle dynamics of equilibrium hard-sphere mixtures. *J. Chem. Phys.*, 127(15):154513, 2007.

[94] B. M. Mladek, J. Fornleitner, F. J. Martinez-Veracoechea, A. Dawid, and D. Frenkel. Quantitative prediction of the phase diagram of dna-functionalized nanosized colloids. *Phys. Rev. Lett.*, 108:268301, 2012.

[95] J. F. Morris. A review of microstructure in concentrated suspensions and its implications for rheology and bulk flow. *Rheol. Acta*, 48(8):909–923, 2009.

[96] J. F. Morris and B. Katyal. Microstructure from simulated Brownian suspension flows at large shear rate. *Phys. Fluids*, 14(6):1920–1937, 2002.

[97] R. D. Mountain and H. J. Raveché. Entropy and molecular correlation functions in open systems. ii two and threebody correlations. *J. Chem. Phys.*, 55(5):2250–2255, 1971.

[98] Z. K. Nagy and R. D. Braatz. Advances and new directions in crystallization control. *Annual Review of Chemical and Biomolecular Engineering*, 3(1):55–75, 2012. PMID: 22468599.

[99] E. Nazockdast and J. F. Morris. Effect of repulsive interactions on structure and rheology of sheared colloidal dispersions. *Soft Matter*, 8(15):4223–4234, 2012.

[100] V. A. Ngo, R. K. Kalia, A. Nakano, and P. Vashishta. Supercrystals of dna-functionalized gold nanoparticles: A million-atom molecular dynamics simulation study. *J. Phys. Chem. C*, 116(36):19579–19585, 2012.

[101] D. Nykypanchuk, M. M. Maye, D. van der Lelie, and O. Gang. Dna-based approach for interparticle interaction control. *Langmuir*, 23(11):6305–6314, 2007.

[102] D. Nykypanchuk, M. M. Maye, D. van der Lelie, and O. Gang. Dna-guided crystallization of colloidal nanoparticles. *Nature*, 451:549–552, 2008.

[103] M. Orozco, A. Perez, A. Noy, and F. J. Luque. Theoretical methods for the simulation of nucleic acids. *Chem. Soc. Rev.*, 32:350–364, 2003.

[104] T. E. Ouldridge. Inferring bulk self-assembly properties from simulations of small systems with multiple constituent species and small systems in the grand canonical ensemble. *J. Chem. Phys.*, 137(14):–, 2012.

[105] T. E. Ouldridge, A. A. Louis, and J. P. K. Doye. Extracting bulk properties of self-assembling systems from small simulations extracting bulk properties of self-assembling systems from small simulations extracting bulk properties of self-assembling systems from small simulations. *J. Phys.: Condens. Matter*, 22(10), 2010.

[106] R. Owczarzy, Y. You, B. G. Moreira, J. A. Manthey, L. Huang, M. A. Behlke, and J. A. Walder. Effects of sodium ions on dna duplex oligomers: improved predictions of melting temperatures. *Biochemistry*, 43(12):3537–3554, 2004.

[107] O. Padovan-Merhar, F. V. Lara, and F. W. Starr. Stability of dna-linked nanoparticle crystals: Effect of number of strands, core size, and rigidity of strand attachment. *J. Chem. Phys.*, 134(24):244701–244701–7, 2011.

[108] S. Y. Park, A. K. R. Lytton-Jean, B. Lee, S. Weigand, G. C. Schatz, and C. A. Mirkin. Dna-programmable nanoparticle crystallization. *Nature*, 451:553–556, 2008.

[109] T. N. Phung, J. F. Brady, and G. Bossis. Stokesian dynamics simulation of brownian suspensions. *J. Fluid Mech.*, 313:181–207, 1996.

[110] S. Prestipino, F. Saija, and P. V. Giaquinta. Phase diagram of softly repulsive systems: The gaussian and inverse-power-law potentials. *J. Chem. Phys.*, 123(14):144110, 2005.

[111] D. C. Rapaport. *The Art of Molecular Dynamics*. Cambridge University Press, 2004.

[112] S. R. Rastogi, N. J. Wagner, and S. R. Lustig. Rheology, self-diffusion, and microstructure of charged colloids under simple shear by massively parallel nonequilibrium Brownian dynamics. *J. Chem. Phys.*, 104(22):9234–9248, 1996.

[113] W. B. Rogers and J. C. Crocker. Direct measurements of dna-mediated colloidal interactions and their quantitative modeling. *Proc. Natl. Acad. Sci. U.S.A.*, 108:15687, 2011.

[114] Y. Rosenfeld. Relation between the transport coefficients and the internal entropy of simple systems. *Phys. Rev. A*, 15:2545–2549, 1977.

[115] Y. Rosenfeld. A quasi-universal scaling law for atomic transport in simple fluids. *J. Phys.: Condens. Matter*, 10:129–134, 2000.

[116] Y. Rosenfeld. Excess-entropy and freezing-temperature scalings for transport coefficients: Self-diffusion in yukawa systems. *Phys. Rev. E*, 62:7524–7527, Nov 2000.

[117] Y. Rosenfeld, E. Nardi, and Z. Zinamon. Corresponding states hard-sphere model for the diffusion coefficients of binary dense-plasma mixtures. *Phys. Rev. Lett.*, 75:2490–2493, 1995.

[118] Y. Rosenfeld and P. Tarazona. Density functional theory and the asymptotic high density expansion of the free energy of classical solids and fluids. *Mol. Phys.*, 95(2):141–150, 1998.

[119] D. Roxbury, A. Jagota, and J. Mittal. Structural characteristics of oligomeric dna strands adsorbed onto single-walled carbon nanotubes. *J. Phys. Chem. B*, 117(1):132–140, 2013.

[120] D. Roxbury, J. Mittal, and A. Jagota. Molecular-basis of single-walled carbon nanotube recognition by single-stranded dna. *Nano Letters*, 12(3):1464–1469, 2012.

[121] C. P. Royall, W. C. K. Poon, and E. R. Weeks. In search of colloidal hard spheres. *Soft Matter*, 9:17–27, 2013.

[122] W. B. Russel and D. A. Saville. *Colloidal Dispersions*. Cambridge University Press, 1999.

[123] R. T. Scarlett, M. T. Ung, J. C. Crocker, and T. Sinno. A mechanistic view of binary colloidal superlattice formation using dna-directed interactions. *Soft Matter*, 7:1912–1925, 2011.

[124] J. H. Schenkel and J. A. Kitchener. A test of the derjaguin-verwey-overbeek theory with a colloidal suspension. *Trans. Faraday Soc.*, 56:161–173, 1960.

[125] T. B. Schroder, N. Gnan, U. R. Pedersen, N. P. Bailey, and J. C. Dyre. Pressure-energy correlations in liquids. V. Isomorphs in generalized Lennard-Jones systems. *J. Chem. Phys.*, 135(13), 2011.

[126] A. Seifpour, S. R. Dahl, B. Lin, and A. Jayaraman. Molecular simulation study of the assembly of dna-functionalised nanoparticles: Effect of dna strand sequence and composition. *Mol. Simulat.*, 39(9):741–753, 2013.

[127] H. Senff, W. Richtering, C. Norhausen, A. Weiss, and M. Ballauff. Rheology of a temperature sensitive coreshell latex. *Langmuir*, 15(1):102–106, 1999.

[128] A. Shankar, A. Jagota, and J. Mittal. Dna base dimers are stabilized by hydrogen-bonding interactions including non-watson–crick pairing near graphite surfaces. *J. Phys. Chem. B*, 116(40):12088–12094, 2012.

[129] M. Shell, P. Debenedetti, and A. Panagiotopoulos. Molecular structural order and anomalies in liquid silica. *Phys. Rev. E*, 66:011202, 2002.

[130] Z. Shi, P. G. Debenedetti, F. H. Stillinger, and P. Ginart. Structure, dynamics, and thermodynamics of a family of potentials with tunable softness. *J. Chem. Phys.*, 135(8):–, 2011.

[131] M. R. Shirts and J. D. Chodera. Statistically optimal analysis of samples from multiple equilibrium states. *J. Chem. Phys.*, 129(12):–, 2008.

[132] B. Srinivasan, T. Vo, Y. Zhang, O. Gang, S. Kumar, and V. Venkatasubramanian. Designing dna-grafted particles that self-assemble into desired crystalline structures using the genetic algorithm. *Proceedings of the National Academy of Sciences*, 110(46):18431–18435, 2013.

[133] A. Stein, B. E. Wilson, and S. G. Rudisill. Design and functionality of colloidal-crystal-templated materials-chemical applications of inverse opals. *Chem. Soc. Rev.*, 42:2763–2803, 2013.

[134] J. J. Stickel and R. L. Powell. Fluid mechanics and rheology of dense suspensions. *Annu. Rev. Fluid Mech.*, 37(1):129–149, 2005.

[135] Y. Sugita and Y. Okamoto. Replica-exchange molecular dynamics method for protein folding. *Chemical Physics Letters*, 314(1-2):141–151, 1999.

[136] P. Sulc, F. Romano, T. E. Ouldridge, L. Rovigatti, J. P. K. Doye, and A. A. Louis. Sequence-dependent thermodynamics of a coarse-grained dna model. *J. Chem. Phys.*, 137(13):135101–135101–14, 2012.

[137] Y. Sun, N. Harris, and C.-H. Kiang. Melting transition of directly linked gold nanoparticle {DNA} assembly. *Physica A: Statistical Mechanics and its Applications*, 350(1):89 – 94, 2005.

[138] P. E. Theodorakis, C. Dellago, and G. Kahl. A coarse-grained model for dna-functionalized spherical colloids, revisited: Effective pair potential from parallel replica simulations. *J. Chem. Phys.*, 138(2):025101–025101–12, 2013.

[139] G. M. Torrie and J. P. Valleau. Nonphysical sampling distributions in monte

carlo free-energy estimation: Umbrella sampling. *Journal of Computational Physics*, 23(2):187–199, 1977.

[140] T. Truskett, S. Torquato, and P. Debenedetti. Towards a quantification of disorder in materials: Distinguishing equilibrium and glassy sphere packings. *Phys. Rev. E*, 62(1):993–1001, 2000.

[141] F. Vargas Lara and F. W. Starr. Stability of dna-linked nanoparticle crystals i: Effect of linker sequence and length. *Soft Matter*, 7:2085–2093, 2011.

[142] P. Varilly, S. Angioletti-Uberti, B. M. Mognetti, and D. Frenkel. A general theory of dna-mediated and other valence-limited colloidal interactions. *J. Chem. Phys.*, 137(9):094108–094108–15, 2012.

[143] D. Vlassopoulos and M. Cloitre. Tunable rheology of dense soft deformable colloids. *Curr. Opin. Colloid Interface Sci.*, 19(6):561–574, 2014.

[144] M. I. Wallace, L. Ying, S. Balasubramanian, and D. Klenerman. Non-arrhenius kinetics for the loop closure of a dna hairpin. *Proc. Natl. Acad. Sci. U.S.A.*, 98(10):5584–5589, 2001.

[145] R. G. Winkler, D. A. Fedosov, and G. Gompper. Dynamical and rheological properties of soft colloid suspensions. *Curr. Opin. Colloid Interface Sci.*, 19(6):594–610, 2014.

[146] K.-T. Wu, L. Feng, R. Sha, R. Dreyfus, A. Y. Grosberg, N. C. Seeman, and P. M. Chaikin. Polygamous particles. *Proceedings of the National Academy of Sciences*, 109(46):18731–18736, 2012.

[147] B. Xu and J. F. Gilchrist. Microstructure of sheared monosized colloidal suspensions resulting from hydrodynamic and electrostatic interactions. *J. Chem. Phys.*, 140(20):204903, 2014.

[148] X. l. Xu, S. A. Rice, and A. R. Dinner. Relation between ordering and shear thinning in colloidal suspensions. *Proc. Natl. Acad. Sci.*, 110(10):3771–3776, 2013.

[149] P. Yakovchuk, E. Protozanova, and M. D. Frank-Kamenetskii. Base-stacking and base-pairing contributions into thermal stability of the dna double helix. *Nucleic Acids Res.*, 34(2):564–574, 2006.

[150] I. Yokoyama. A relationship between excess entropy and diffusion coefficient for liquid metals near the melting point. *Physica B: Condens. Matter*, 254:172–177, 1998.

[151] Z. Zhou, J. V. Hollingsworth, S. Hong, G. Wei, Y. Shi, X. Lu, H. Cheng, and C. C. Han. Effects of particle softness on shear thickening of microgel suspensions. *Soft Matter*, 10:6286–6293, 2014.

[152] J. Zhu, M. Li, R. Rogers, W. Meyer, R. H. Ottewill, W. B. Russel, and P. M. Chaikin. Crystallization of hard-sphere colloids in microgravity. *Nature*, 387(6636):883–885, 06 1997.

Appendix A

Estimation of energy penalty of single antisite

Here we compute the expected value of energy penalty of single antisite on the edge of perfect lattices. In order to grow the desired crystal lattices, we make the following assumptions: for square lattices, we assume $E_{AA} = E_{BB} = 0$; for alternating-string hex lattices, we assume $E_{AA} = E_{BB}$; for honeycomb lattices, we assume $E_{AA} \leq E_{BB}$. Δ is defined as $E_{BB} - E_{AA}$. Δ_{AB} is defined as $E_{AB} - E_{AA,BB}$. Δ'_{AB} is defined as $E_{AB} - E_{AA}$. The maximum number of nearest neighbors (NNs) on the edge of formed crystal lattice is assumed to be four. This is true for square lattices. While hex lattices can have up to 6 NNs, those additional NNs are assumed to be less stable and therefore rare in reality.

A.1 Square lattice

Table A.1: Estimated energy penalty of single antisite for square lattice ($=2E_{AB}$)

Number of NNs	Energy penalty	Probability
1 NN		
A	E_{AB}	$\frac{1}{8}$
B	E_{AB}	$\frac{1}{8}$
2 NN		
AA	$2E_{AB}$	$\frac{1}{4}$
BB	$2E_{AB}$	$\frac{1}{4}$
3 NN		
AAA	$3E_{AB}$	$\frac{1}{8}$
BBB	$3E_{AB}$	$\frac{1}{8}$

A.2 Alternating-string (A-S) lattice (side 1)

Table A.2: Estimated energy penalty of single antisite for A-S lattice ($=\Delta_{AB}$)

Number of NNs	Energy penalty	Probability
2 NN		
AB	0	$\frac{1}{8}$
BA	0	$\frac{1}{8}$
3 NN		
BBA	Δ_{AB}	$\frac{1}{8}$
ABA	Δ_{AB}	$\frac{1}{8}$
AAB	Δ_{AB}	$\frac{1}{8}$
BAB	Δ_{AB}	$\frac{1}{8}$
4 NN		
BBAB	$2\Delta_{AB}$	$\frac{1}{8}$
AABA	$2\Delta_{AB}$	$\frac{1}{8}$

A.3 Alternating-string (A-S) lattice (side 2)

Table A.3: Estimated energy penalty of single antisite for A-S lattice ($=\Delta_{AB}$)

Number of NNs	Energy penalty	Probability
2 NN		
AA	$2\Delta_{AB}$	$\frac{1}{8}$
BA	$2\Delta_{AB}$	$\frac{1}{8}$
3 NN		
BBA	Δ_{AB}	$\frac{1}{8}$
ABB	Δ_{AB}	$\frac{1}{8}$
AAB	Δ_{AB}	$\frac{1}{8}$
BAA	Δ_{AB}	$\frac{1}{8}$
4 NN		
BAAB	0	$\frac{1}{8}$
ABBA	0	$\frac{1}{8}$

A.4 Honeycomb lattice

Table A.4: Estimated energy penalty of single antisite for honeycomb lattice $(=\Delta'_{AB})$

Number of NNs	Energy penalty	Probability
2 NN		
AB	Δ	$\frac{1}{12}$
BA	Δ	$\frac{1}{12}$
BB	$2\Delta_{AB}$	$\frac{1}{12}$
3 NN		
BAB	$\Delta - \Delta_{AB}$	$\frac{1}{6}$
ABA	$\Delta + \Delta'_{AB}$	$\frac{1}{6}$
BBB	$3\Delta_{AB}$	$\frac{1}{6}$
4 NN		
ABAB	2Δ	$\frac{1}{12}$
BABA	2Δ	$\frac{1}{12}$
BBBB	$4\Delta_{AB}$	$\frac{1}{12}$

Appendix B

Vita

Yajun Ding was born in Changzhou, Jiangsu (China) on 03 December 1983, the son of Mr. Jianping Ding and Heying Hao. He received the Bachelor of Science degree in Chemical and Biological Engineering from China Agricultural University, Beijing (China) and Master of Science in Chemical and Biomolecular Engineering from University of Pennsylvania. He started his graduate studies in Chemical Engineering at the Lehigh Univeristy in August 2010.